Pristine $Ti_3C_2T_x$ MXene electrode for the electrochemical detection of biomarker H_2O_2 in the tear fluid

Maria Natalia Noriega Pedraza

A Thesis submitted in partial fulfilment of the requirements of the University of Brighton for the degree of Doctor of Philosophy

Abstract

Non-invasive diagnostics are gaining prominence due to their ability to seamlessly monitor physiological changes over a person's lifetime and positively impact decision-making, lifestyle choices, and habits. Contact lenses, being one of the most common wearable devices, offer a unique platform for the non-invasive monitoring of analytes in the tear fluid. Ophthalmic biomarkers have been identified as a promising route for disease detection. However, challenges in developing these complex technologies lie in having to match the strict requirements of contact lenses with that of the diagnostic device. Moreover, achieving high sensitivity in order to sense analytes in the range of ophthalmic analyte concentrations is of upmost importance.

$Ti_3C_2T_x$ MXene is a two-dimensional material that has been incorporated in several diagnostic technologies with reported enhanced sensitivities and limits of detection. Electrochemical sensors typically take advantage of their high conductivity, redox-active surfaces, and easy processability. However, only complex composites or electrode coatings have investigated the performance of $Ti_3C_2T_x$. Therefore, the optimisation of $Ti_3C_2T_x$ towards electrochemical sensing is limited. Moreover, pristine $Ti_3C_2T_x$ possesses several properties that may result in the development of unique sensors which have yet to be explored.

The objective of this thesis was to showcase the potential of $Ti_3C_2T_x$ MXene as a pristine electrode for the detection of ophthalmic biomarkers. Initially, a fabrication protocol was developed for creating pristine $Ti_3C_2T_x$ electrodes, eliminating the need for current collectors or other electroactive materials. The MXene electrode was characterised using ruthenium hexamine as the outer sphere standard probe. Electrode optimisation for electron transfer was achieved by employing large MXene flakes and thin electrode thickness, resulting in an increase in the ratio between faradaic and capacitive currents in cyclic voltammograms. Additionally, the successful demonstration of flexible and transparent electrodes without compromising the electrochemical signal was achieved for the first time.

Subsequently, electrode optimisation for hydrogen peroxide, as a relevant reactive oxygen species in the tear fluid, detection was performed. It was observed that smaller flake sizes exhibited the highest sensitivity to hydrogen peroxide. The sensitivity to hydrogen peroxide was found to be independent of electrode thickness, highlighting the potential of thin MXene films for transparent sensors. Furthermore, an investigation into optimising the electrochemical parameters revealed that the highest sensitivity for hydrogen peroxide detection was achieved at -1050 mV vs Ag|AgCl. Importantly, no interference was observed from other potential interferent agents present in tear fluid, underscoring the selectivity of $Ti_3C_2T_x$ for hydrogen peroxide detection at this potential. Finally, the pristine $Ti_3C_2T_x$ electrode was successfully incorporated into a commercially available contact lens as a proof of concept. Contact angle measurements confirmed the hydrophilicity of $Ti_3C_2T_x$, resulting in increased wettability of the lens. The stability of the coating in storage contact lens solution and simulated tear fluid was demonstrated. The cytocompatibility of $Ti_3C_2T_x$-coated contact lenses was evaluated using a human corneal epithelial cell line, showing no significant differences between large and small flakes. Ultimately, the successful detection of hydrogen peroxide using a transparent and flexible pristine $Ti_3C_2T_x$ sensor incorporated into the lens was demonstrated.

Overall, this thesis establishes the potential of $Ti_3C_2T_x$ MXene as a promising material for ophthalmic biomarker detection, showcasing its excellent electrochemical performance, selectivity, stability, and compatibility as an electrode incorporated into commercially available contact lenses.

Content

Acknowledgements

I'm deeply grateful to my supervisory team: Dr. Susan Sandeman, Prof. Bhavik A. Patel, Prof. Yury Gogotsi, Dr. Marcus Dymond, and Dr. Joseph Lacey, for their invaluable support and guidance throughout my PhD journey. Your diverse expertise has greatly enriched my knowledge, and I have learned immeasurably from each of you. Special thanks to Emma, Grace and Fernando, for your generosity in sharing your knowledge and for your friendship along the way. To the Patel Lab, thank you for welcoming me halfway through and providing invaluable mentorship. Thank you to everyone in the PhD office and UoB staff. I am also grateful to Yury and the DNI team for their collaboration and friendship, especially to Geetha, Alex, Lingyi, and others who supported my work, including Babak, Mike, Chris, Armin, John, Kathleen and Jamie. To Prof. Flavia Vitale at the University of Pennsylvania, thank you for your mentorship and welcoming me into your lab during my time in Philadelphia. Thank you to Brendan Murphy for your guidance in navigating my early understanding of analytical electrochemistry.

Throughout my PhD journey, I've encountered a wealth of experiences that extend far beyond academic growth. To my friends who have become like family, thank you. Your friendship has brought light to the tough and stressful times of research, creating cherished memories, and making both, Brighton and Philadelphia, feel like home. Your hospitality, every tennis match, the numerous game nights, long phone calls and trips together have made this journey not just academically fulfilling, but also deeply meaningful. Your presence has truly made a profound impact, and for that, I am sincerely grateful.

Finally, I extend my heartfelt gratitude for the support of my parents Pedro and Luz Marina, and to the rest of my family and friends in Mexico, Colombia, around the world and those who are watching over us. Ma y pa, your unconditional love, guidance, encouragement, and patience have propelled me forward, but it is the thought of coming back home every time that makes every effort worthwhile. This thesis is dedicated to both of you.

List of Figures

Declaration

I declare that the research contained within this thesis, unless otherwise stated within text, is the original work of the author. The thesis has not been previously submitted in any form to any other university in fulfilment of any degree or qualification. All sources are acknowledged as references. An exception to this statement is sections in Chapter 2 and 3 published as a lead authorship journal article and reprinted with permission from Natalia Noriega, Mikhail Shekhirev, Christopher E Shuck, Jonathan Salvage, Armin VahidMohammadi, Marcus K Dymond, Joseph Lacey, Susan Sandeman, Yury Gogotsi, Bhavik Anil Patel. “Pristine $Ti_3C_2T_x$ MXene Enables Flexible and Transparent Electrochemical Sensors” ACS Appl Mater Interfaces, 2024,16(5):6569-6578. Copyright 2024, American Chemical Society.

Natalia Noriega

Abbreviations

2D	Two-dimensional
3D	Three-dimensional
BPE	Basal plane electrode
BSA	Bovine serum albumin
CE	Counter electrode
DI	Deionised
DLS	Dynamic light scattering
EDE	Edge plane electrode
EDS	Energy-dispersive X-ray spectroscopy
EMI	Electromagnetic interference
FAD	Flavin adenine dinucleotide
FET	Field effect transistor
GC	Glassy carbon
GO	Graphene oxide
GOx	Glucose oxidase
H_2O_2	Hydrogen peroxide
HF	Hydrofluoric acid
HCE	Human Corneal Epithelial
HCl	Hydrochloric acid
IL-1β	Interleuking-1β
IL-6	Interleukin-6
IL-8	Interleukin-8
IoT	Internet of things
ITO	Indium tin oxide

LiCl	Lithium chloride
LOD	Limit of detection
MMP-9	Matrix metalloproteinase-9
NF	Nanofiber
NP	Nanoparticle
NW	Nanowire
PBS	Phosphate buffer saline
PET	Polyethylene terephthalate
PI	Polyamide
PDI	Polydispersity index
PMMA	Polymethyl methacrylate
POC	Point-of-care
PVA	Polyvinyl alcohol
PVDF	Polyvinylidene difluoride
RE	Reference electrode
Rpm	Rounds per minute
RuHex	Hexaammineruthenium (III) chloride
rGO	Reduced graphene oxide
SE	Shield effectiveness
SEM	Scanning electron microscopy
TCE	Transparent conductive electrode
UV	Ultraviolet
VD3	1α,25-Dihydroxyvitamin D3
Vis	Visible
WE	Working electrode
XRD	X-ray diffraction

1 Introduction

1.1 Overview

In this study, the novel application of $Ti_3C_2T_x$ MXene as a pristine electrode for developing tear-fluid diagnostics integrated into contact lenses was explored. Electrochemical sensing was chosen as the detection mechanism due to its established sensitivity and fast response; surpassing alternative methods such as optical or mechanical sensing(1). The properties of $Ti_3C_2T_x$ MXene establish it as a promising candidate for electrochemical sensing, owing to its high conductivity and redox-active surface. Additionally, the optical and mechanical characteristics of $Ti_3C_2T_x$ MXene make it an ideal candidate for applications where transparent and flexible electrodes are needed, such as in the field of smart contact lenses (2). Previous research has demonstrated $Ti_3C_2T_x$ biocompatibility and positive wound-healing response in several biological systems, including the anterior eye(3,4). Given the unique and promising properties of $Ti_3C_2T_x$ MXene, this investigation extends from its foundational use as an electrode to its incorporation and comprehensive characterisation within a commercial contact lens as a functional sensor. This research aims to unlock the potential of $Ti_3C_2T_x$ MXene in revolutionising the field of tear-fluid diagnostics, offering innovative solutions for disease monitoring and early detection in ophthalmology.

This chapter begins with an exploration of the role of tear fluid, its composition and the presence of biomarkers for potential use in sensor diagnostics. A review of the current state of electrochemical sensors incorporated into contact lenses is then conducted, emphasising the role of nanomaterials in shaping these technologies. The family of two-dimensional materials MXenes is then introduced outlining their relevant properties and applications, leading to an investigation of $Ti_3C_2T_x$ specifically, as a potential candidate for use in an electrochemical sensor for monitoring tear fluid biomarkers.

1.2 The tear fluid

1.2.1 Biological role

The tear fluid is a biological lubricant sitting on the ocular surface corneal epithelial layer. It plays various biological roles including lubrication of the eyelids, conjunctiva, and cornea, providing nourishment of the cornea, and protection from external irritants, such as dust and foreign particles(5). By maintaining a smooth surface on the avascular cornea, the tears also provide a light refraction for the visual system. The secretion of tears is complex and involves several glands, including the lacrimal glands, accessory lacrimal glands, goblet cells of the conjunctiva, and Meibomian glands at the lid margin (Figure 1.1a) (6).

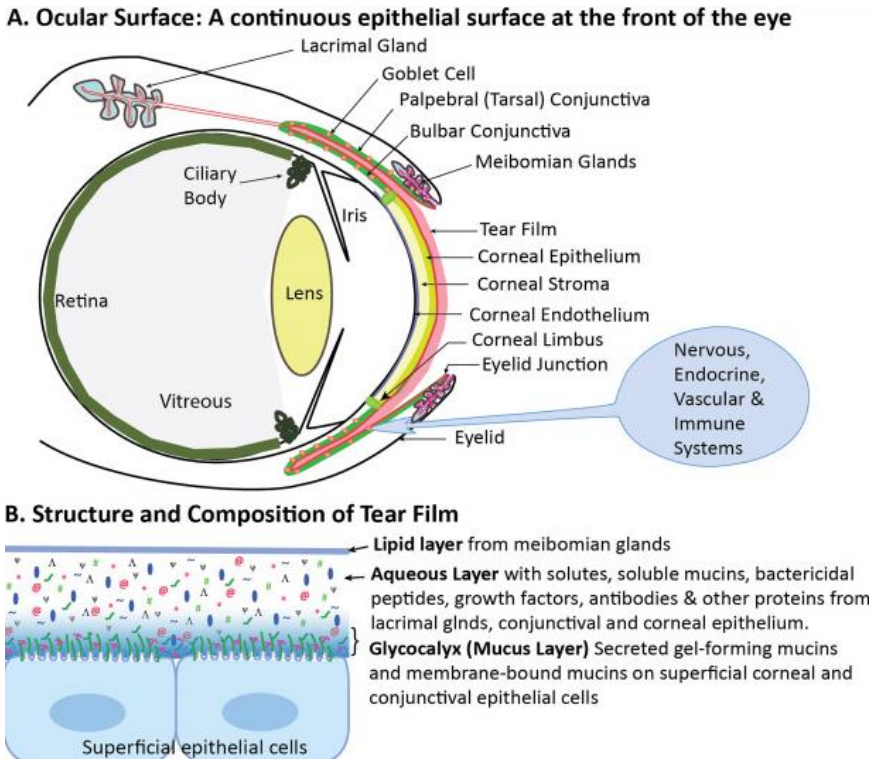

Figure 1.1 Schematic of the eye and the tear film**.** a) Anatomical structure of the eye showing the ocular surface and the tear secretory glands. b) The structure and composition of the tear film made up of the outer lipid layer, the aqueous layer and the inner mucus layer. (6).

As shown in Figure 1.1b, the tear film consists of three distinct layers: a lipid layer, an aqueous layer, and an inner layer (6). The inner glycocalyx layer, produced mostly by the conjunctiva goblet cells and closest to the eye's epithelia, removes contaminants through the nasolacrimal duct, aided by eyelid movement during blinks (7). Moreover, its hydrophilic nature enables the aqueous layer, primarily produced by the lacrimal glands and accessory lacrimal glands, to be evenly distributed across the eye. In addition to soluble mucins, the aqueous layer is composed of numerous constituents including proteins, electrolytes, and water that nourish the avascular corneal tissue (8). Finally, the outer tear layer is prominently produced by the Meibomian glands and is made up of lipids that support the stability of the tear by avoiding its evaporation when the eyelids are open (8). The tear film has been calculated to be approximately 5-10 μm in thickness through multiple measurement methods including the glass filament and fluorometric methods (9). Its overall rate of production is approximately 1-2 μL per minute under normal conditions, but this rate can increase to more than 100 μL per minute when stimulated (10). Emotional and reflective tears, which are produced in response to emotions or presence of foreign objects in the eye, respectively, are mostly secreted by lacrimal glands compared to basal tears whose production has already been discussed (11). Therefore, the mechanism of production will vary the composition of the tears. Emotional tears are generally produced upon signalling from the brain to the lacrimal glands. Instead, reflective tears are generated as a response to changes in the ocular environment through stimulation of corneal sensory nerves.

1.2.2 Ophthalmic biomarkers

According to the National Institute of Health Biomarkers Definitions Working Group, a biomarker (or biological marker) is defined as an objectively measured characteristic used to indicate normal biological processes, pathological processes, or responses to therapeutic interventions (12). The rich composition of the tear fluid has gained increasing interest as an accessible body fluid in predictive, preventive, and personalised medicine. Table 1.1 presents

the primary constituents of the tear fluid, which are proteins, mucins, lipids, and salts [13]. Researchers have extensively explored tear fluid and identified biomarkers for ophthalmic and systemic diseases including neurological and genetic disorders (13).

Table 1.1. Typical concentrations of predominant components in the tear fluid (13). Reprinted under the free to use Creative Commons license (http://creativecommons.org/licenses/by/3.0/).

Component	Concentration
Na^+	120–165 mM
K^+	15–42 mM
Cl^-	118–135 mM
Mg^{2+}	0.5–1.1 mM
Ca^{2+}	0.4–1.1 mM
HCO_3^-	20–42 mM
Urea	6 mM
Ascorbate	11–23 μM
Lactate	1–5 mM
Glucose *,**	0.1–0.6 mM
Total Protein	5–11 mg/mL

1.2.2.1 Proteins

More than 1500 proteins have been identified in tear fluid with an average concentration of 5-11 mg mL^{-1} (14). This is a higher protein concentration than in serum and plasma, making tear fluid attractive for its rich proteome(15). Additionally, it has fewer potential interferents than other accessible body fluids such as urine. The tear fluid contains a diverse array of proteins, including enzymes, antibodies, and signalling molecules. However, lactotransferring, lipocalin-1, serum albumin, lysozyme C and several immunoglobulins are among some of the most prominent proteins presents. Various groups have published comprehensive studies summarizing protein biomarkers in the tear fluid for both ocular and systemic diseases. Among these, conditions like keratoconus(16), diabetic retinopathy (DR), multiple sclerosis (MS), Parkinson's disease (PD), and breast cancer have emerged as prominent areas of investigation(15).

Protein biomarkers can also serve to monitor the response to therapeutic treatments or medical devices. For instance, a study on the impact of contact lenses on corneal epithelial health

highlighted the risk of corneal inflammation and infection with a decrease in antimicrobial enzyme regulation in contact lens wearers (17). The detection of cytokine release including IL-1β, IL-6, and IL-8, has also been performed to study immune response and inflammation mechanisms of human corneal epithelial (HCE) cells following exposure to damaging treatments. For example, the monitoring of these cytokines over time was used to investigate the regulatory role of IL-1β during Pseudomonas aeruginosa colonisation. The study utilised three different bacterial strains; non-infectious strain Paer1 isolated from contact lens-induced acute red eye, and infectious strain 6206 and 6294 isolated from microbial keratitis on HCE cells (18). Results suggest IL-1β having a regulatory role in the expression of IL-8 and IL-6 during Pseudomonas aeruginosa colonisation. The same group a year later demonstrated inhibition of cytokine expression after Pseudomonas aeruginosa colonisation upon treatment with 1α,25-dihydroxyvitamin D_3 (VD_3). Their work suggested the use of VD_3 as an anti-inflammatory agent for HCE cells in ocular diseases (19). A similar study on HCE cells was performed to determine the anti-inflammatory and anti-oxidation effect of green tea polyphenol epigallocatechin gallate(20). The inhibition of the activation of p38 and JNK as well as transcription factors demonstrated the anti-inflammatory and anti-oxidation effect of green tea after the challenge of HCE cells with IL-1β or hyperosmolarity. Moreover, studies on the tear fluid of contact lens wearers, ocular diseases, and microbial infections detected significant changes in these cytokines compared to controls (21–23).

1.2.2.2 Lipids

Over 150 lipids have been identified in the tear fluid, which primarily comprises phosphatidylcholines and phosphatidylethanolamine lipids with a smaller contribution from non-polar triglycerides, polar sphingomyelins, and ceramides (24). Sampling of lipids in the tear fluid demonstrates the potential to understand how disease and extracellular stress affect the composition of tear fluid. For example, a dysregulation of tear lipids in graft-versus-host disease upon allogeneic hematopoietic stem cell transplantation was highlighted by Ma et

al.(25). Their work suggests several lipids and lipid mediators including phosphatidylcholine, sphingomyelin, lactosylceramide and docosahexaenoic acid as potential tear biomarkers for identifying ocular graft-versus-host disease. The role of sphingolipid metabolism has also been studied against exogenous ocular stress in which ultraviolet (UV)-B radiation and hyperosmolarity increased the secretion of sphingomyelinase from HCE cells (26). Additionally, the downregulation of sphingomyelins in the tears of patients with multiple sclerosis was correlated with that in cerebrospinal fluid suggesting a potentially easier sampling route for detection of changes in lipid metabolism in these patients. Lipid biomarkers have also been linked to numerous different disorders including dry eye syndrome (keratoconjunctivitis sicca) and Meibomian gland dysfunction (24,27,28).

1.2.2.3 Salts

Tears contain a variety of electrolytes crucial for maintaining optimal corneal epithelial health and function and buffering the pH of tears. Osmolality, which measures the concentration of dissolved solute particles per kilogram of solvent in a solution, plays a vital role. Electrolytes are primary contributors to osmolality, in which sodium (Na^+), potassium (K^+), chloride (Cl^-), and bicarbonate (HCO_3^-) exhibit the highest concentration in tears, whereas proteins and sugars have minimal impact due to their high molecular weight and low concentration (29). As a result, the dynamic production of electrolytes by the lacrimal gland, the accessory glands of Krause and Wolfring, the cornea, and the conjunctiva significantly influences the osmotic balance of tear fluid.

Abnormal tear osmolality, whether it's too high or too low, can indicate conditions like dry eye disease or other ocular surface disorders. The presence and balance of these electrolytes in tear fluid are vital for preventing osmotic stress, protecting against microbial infections, and facilitating the transport of nutrients and waste products across the ocular surface.

1.2.2.4 Metabolites

Metabolites are intermediate molecules or final products of metabolic processes. Detecting the abnormal concentrations in the tear fluid can be useful for monitoring disease

(30). For example, lower levels of amino acids including alanine, arginine, glutamine/lysine, and methionine, and higher homocysteine concentrations were found in tears compared to controls (31,32). This work suggests a metabolomic approach to detect early glaucoma before the intraocular pressure results in a significant loss of retinal ganglion cells and visual field impairment. Catecholamines including norepinephrine and dopamine have been identified as biomarkers in the tear fluid for early diagnosis of Parkinson's disease (33). A unique signature of metabolites was also identified in patients with Sjogren's syndrome (34), and keratoconus patients (35). Glucose is among the most prevalent metabolites used for disease monitoring. Correlations between tear glucose concentrations and blood glucose levels have proven effective in identifying hyperglycaemic patients (36).

1.2.3 Tear fluid analysis

1.2.3.1 Extraction techniques

Analysis of ophthalmic biomarkers in the tear fluid typically necessitates the extraction of tear fluid from the eye. The different approaches to accomplish this can be categorised as direct and indirect sampling methods (37). Typically, direct tear fluid sampling from the eye has been conducted using microcapillary tubes or micropipettes. The disadvantage of this approach is the small amount of tear fluid available in the eye, and the potential contact of the pipette with the ocular tissue surface. Especially in patients with dry eye syndrome, where tear fluid is naturally diminished due to either reduced production or increased evaporation, this presents a significant challenge (38,39). Work to overcome these issues, is either the stimulation of reflective tear production (40), or the addition of saline solution to the eye before extraction (flushed tears). These approaches have been documented in several prior studies, wherein saline solution additions of up to a volume of 60 µL were administered before tear sampling (39,41,42). However, studies must consider the fact that reflective tears differ in composition from that of basal tears. The different production mechanisms of these tears likely contribute to their composition and therefore the location of extraction or its mixture during flushing may also disturb the samples. This was highlighted by A. Rohit et al. (42) in which a

significant difference in lipid profile between basal, reflective, and flushed tears was observed. Meanwhile, studies led by R. J. Fullard demonstrated that the concentration of only certain proteins (lactoferrin, albumin, peroxidase, and lysozyme) and cytokines remained the same throughout flushed and basal tear samples (39,43). Their work suggests that while the collection of basal tears is more reliable, flushed tears may be a good representation of the tear fluid composition for the investigation of specific analytes.

Indirect tear fluid samples include the use of Schirmer test strips, filter paper disks, cellulose sponges, and polyester rods (44). Generally, these tools work by absorbing tear fluid samples after placement in the ocular tissue for a determined amount of time, followed by submerging in buffers to dilute the collected samples. Key to the indirect sampling approaches is the complete elution of the tear fluid sample (and all its components) from the sampling tool. Schirmer strips are one of the most common tools to extract tear fluid in human patients (45). Contact lenses have also been used to collect tear fluid samples, followed by submersion onto buffers for subsequent colourimetric, fluorometric, electrical, and electrochemical analysis (46,47).

Despite the challenges posed by extraction techniques in obtaining reliable, unaltered, and reproducible tear fluid samples, they have significantly contributed to the current understanding of tear compositions. These techniques, coupled with multiple analysis methods including proteomics, lipidomics, metabolomics, and others, have unveiled various biomarkers present in tears, as previously discussed. However, limitations persist in studying tear composition at singular time points rather than exploring the dynamic changes of biomarkers over time. Furthermore, the cumbersome nature of the extraction mechanisms and analysis necessitates specialised personnel, rendering tear analysis impractical for routine, day-to-day use of basal tears. Current efforts are focused on developing technologies capable of continuous monitoring of biomarkers in tear fluid to deepen the understanding of disease, enable early disease detection, facilitate non-invasive disease monitoring and analysis of treatment efficacy.

1.2.3.2 Overview of contact lenses as platforms for non-invasive monitoring of ophthalmic biomarkers

Contact lenses, introduced in the 1930s, have revolutionised vision correction, with their development driven by advances in lens material science(48). The initial scleral lens made of glass has evolved into soft polymeric materials, ensuring comfort (49). Current commercially available contact lenses provide comfortable vision correction for daily, bi-weekly, and monthly wear, accommodating diverse prescriptions while addressing concerns like dryness and UV protection. Multiple reviews have comprehensively examined the characteristics of contact lens materials (49–51).

Beyond vision correction, contact lenses are increasingly employed for diagnostic purposes, facilitating non-invasive and continuous monitoring of ophthalmic biomarker biomarkers (50). Common components integrated into these devices are microfluidic channels (52–55). These microfluidic channels are strategically designed to efficiently guide the minute volumes of basal tear fluid collected from the eye into a reservoir within the contact lens. Capillary pressure enables the tear fluid to enter the system through the inlet opening located on the concave side of the lens (Figure 1.2) (53). Another important component, following the microfluidic design for tear fluid collection within the lens, is the sensing mechanism which is crucial for biomarker detection. The two main transduction mechanisms that have been previously incorporated into contact lenses are optical and electrochemical sensors. A change in optical properties as a result of the interaction between the analyte and the bioreceptor has been used to measure biomarker concentrations in tear fluid including ions, ascorbic acid, and glucose (46,53,56). An advantage of optical sensors is that they do not require any power input or complex electronic system to output the signal. However, only a few studies have measured *in vivo* with successful correlations between blood and tear glucose concentrations in clinical trials (57,58). Innovative studies have utilised smartphones as a cost-effective means to analyse these optical changes, enabling convenient and accessible health monitoring for the wearer (59) . Contrastingly, electrochemical sensors which rely on an applied voltage for the detection of biomarkers,

require power input. Despite this challenge, numerous reports demonstrate working wireless electrochemical sensors on contact lenses for the continuous monitoring of biomarkers including glucose and cortisol (54,60). Electrochemical sensors stand out as using the most promising mechanism for real-time and sensitive detection of ophthalmic biomarkers. Their potential lies in their ability to accurately measure and record subtle changes in biomarker concentrations, paving the way for precise health monitoring and early disease detection (61–64).

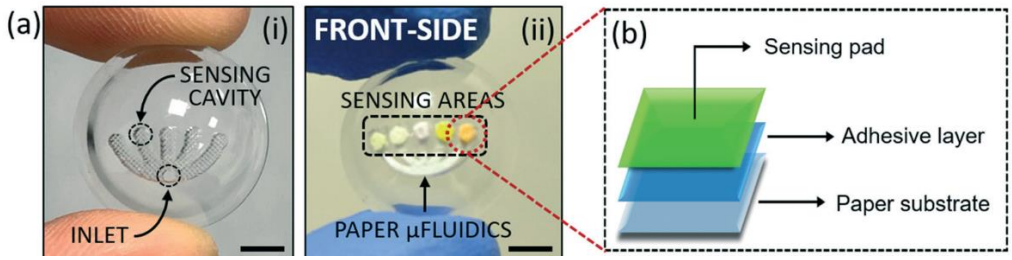

Figure 1.2 Microfluidic contact lens sensor. a) Contact lens design (i) laser-inscribed microfluidic system. (ii) Integrated system with embedded paper microfluidic chip. b) Layers of sensor system. Reprinted with permission from Royal Society of Chemistry (53)

1.3 Electrochemical sensors

1.3.1 Basics of electrochemistry

Analytical electrochemistry studies the relationship between current, charge, and potential to analyse species in a system (65). Electron transfer between the analyte of interest and the electrode (or conductor) occurs when the applied potential is sufficient for a redox reaction to take place. When the applied potential is sufficiently positive to oxidise a molecule, the molecule loses electrons which are transferred to the electrode. Conversely, when the applied potential is sufficiently negative to reduce a molecule, it is the electrode that loses electrons that are transferred to the molecule. The rate of the redox reaction as well as its resulting current are governed by electron transfer and mass transfer (66). Mass transfer is

governed by diffusion, convection, and migration. However, in a controlled electrochemical experiment, convection and migration can be neglected by the use of a highly concentrated supporting electrolyte and the avoidance of stirring (67). The simplest process of electron transfer starts with the analyte travelling from the bulk to the interface between electrode and electrolyte (mass transfer), followed by the electron transfer between the analyte and the electrode (heterogeneous electron transfer), and finalising with the product transfer from the electrode surface back to the bulk solution. In more complex systems, other steps such as adsorption and crystallisation may occur (Figure 1.3). It is the slowest step of the process that determines the overall rate of the reaction.

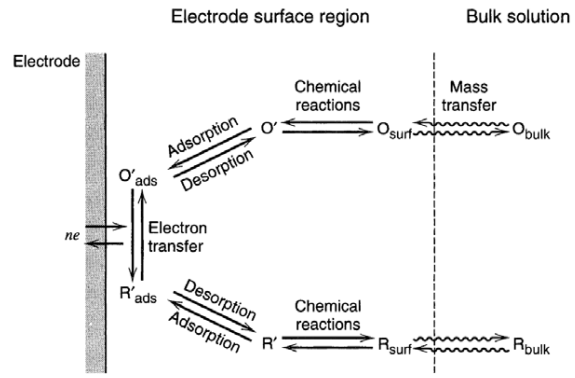

Figure 1.3. Pathway of a general redox reaction at the electrode surface. Reprinted with permission from John Wiley and Sons (66).

Depending on the electrical parameter explored, electrochemical techniques can be categorised into potentiometry, conductometry, and amperometry. Potential-controlled techniques most commonly utilised in the fundamental study of electroanalysis, rely on the interrogation of an electroactive species using an applied potential to measure the current response.

1.3.1.1 Electrochemical cell

The electrode at which the redox reactions occur is known as the working electrode (WE) and it makes up to one of the two or three electrodes used in an electrochemical cell. Electrodes are simply conductors that enable the flow of charge, and it is the external applied potential, commonly from a potentiostat, that dictates the role of each electrode during the

experiments. The potential applied flows between the WE and the counter electrode (CE). The third electrode, known as the reference electrode (RE) monitors the applied potential at the WE and it is why most electrochemical experiments use 3-electrodes in their setup (67). The three electrodes are immersed in a solution known as the electrolyte in which the analyte is found. This is the last component of a full-working electrochemical cell. Depending on the focus of the electrochemical studies, one may choose between simulating, in part, properties of the medium in which the analyte will be found in real-life applications such as the use of phosphate buffer saline solution (PBS) for biological studies, or isolating the analyte by simply providing a medium for diffusion from the bulk environment to the electrode surface.

1.3.1.2 Factors influencing electron and mass transfer

The mass transfer and electron transfer mechanism as well as their rate of reaction will be influenced by the analyte itself as well as several parameters of an electrode including electrode material, surface chemistry, and size.

a. Electrode size

The size of the electrode can play an important role regarding the diffusion dynamics and as a result current density (66). Radial and planar diffusion are two paths of diffusion that can occur at an electrode surface. The critical dimension generally determines whether an electrode is considered macro- or micro-electrode and it is defined by the thickness of the diffusion layer. If one dimension of the electrode is smaller than the critical dimension, generally below 25 μm, the electrode is considered a microelectrode (66). For macroelectrodes, where the flux of analytes towards the electrode surface is planar diffusion, Cotrell and Randle-Sevcik equations, derived from Fick's law, are used to theoretically calculate the current generated by redox reactions. Randles-Sevcik equation (Eq 1.1) is used in voltammetry as it describes the relationship between peak current (i, A) with respect to scan rate (υ, V s^{-1}), the diffusion coefficient (D_o), the electrode surface area (A, cm) and analyte concentration, (c, mol cm^{-2}) where n is the number of electrons involved in the redox reaction, t is temperature, T (K), F is the Faraday's constant (96485.3321 C mol^{-1}) and R is the gas constant (8.3145 J k^{-1} mol^{-1}).

Randles Sevcik equation can be used in different circumstances to characterise either the surface area of an electrode or estimate the experimental current when all the variables are known.

$$I_p = 0.4463 \left(\frac{n^3F^3}{RT}\right)^{1/2} AD^{1/2}cv^{1/2} \qquad \text{Equation 1.1}$$

Instead, the Cotrell equation (Eq 1.2) describes the relationship between current with time (t, s) rather than with scan rate, and it is used to estimate currents in amperometry techniques. Considering that microelectrodes have an enhanced mass transfer from radial diffusion, modifications to the Cottrell equation were reported to take into account the size and geometry of microelectrodes (68).

$$i = \frac{\mathrm{nF\ A\ C}\sqrt{\mathrm{D}}}{\sqrt{\pi \mathrm{t}}} \qquad \text{Equation 1.2}$$

Steady-state arises when the rate of the redox reaction at the electrode surface is equal to the rate of mass transfer of the analyte to the surface. This can be attained at slow-scan rates in microelectrodes and is identified by the s-shape in cyclic voltammograms. Relevant to this chapter, a band microelectrode is depicted in Figure 1.4 in which the width of the electrode band must measure less than the critical dimension to develop a microelectrode. However, even if the mass transfer is dominated by radial diffusion at slow scan rates, true steady-state responses are not obtained and instead only a pseudo-steady-state can be achieved.

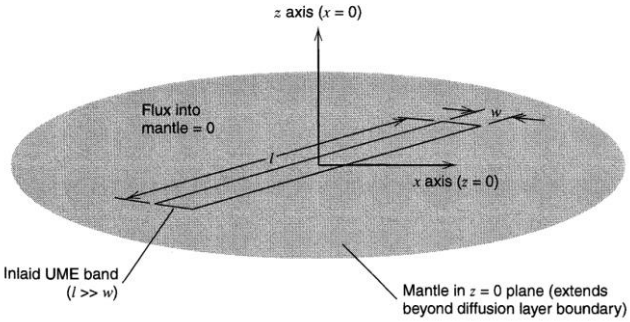

Figure 1.4 Diffusion at a band microelectrode where the length of the electrode is significantly larger than the width. Reprinted with permission from John Wiley and Sons (66).

b. Electrode material

The selection of favourable electrode material for tailorable electrochemical behaviour is key to enabling specific redox reactions. This includes electron transfer kinetics, adsorption, and electrocatalysis which are strongly influenced by the material's surface chemistry and electronic properties (69–71). Carbon electrodes are known for their chemical inertness and wide potential window and have applications in the oxidation and reduction of numerous analytes (72). There are many types of carbon electrodes including glassy carbon, boron-doped diamond, graphite, and carbon nanomaterials providing an extensive selection with further tailorable properties (69). The different electrochemical behaviours of these carbon and carbon-rich materials are typically attributed to the relative density and orientation of edge and basal planes at the electrode surface as well as the resulting surface chemistry of the multiple synthesis approaches (69),(65). A great example of such, is focused on enhancing the adsorption-limited electron transfer of dopamine via surface. This approach has been reported to enhance ET of dopamine in several carbon electrodes. Generally, oxygen-containing functional groups, including hydroxyl- and carboxyl groups, enhance the mechanism of dopamine oxidation and therefore, anodisation and acidic treatments have been utilised (73),(74),(75). Despite years of research on this subject, the detailed impact of different oxygen-

containing groups on dopamine sensitivity and ET kinetics remains a debate in the literature (76). Metal electrodes on the other hand are known for their high conductivity and good electrocatalysis, providing a surface for fast redox reactions (77,78). Platinum and gold electrodes are the most widely used metal electrodes due to their wide anodic potential window, specifically, gold is known for being more inert. However, their high cost due to the scarcity of noble metals in the Earth's crust makes their use limited to very specific applications. To enhance the performance of traditional electrode materials, nanomaterials have been used to increase the current densities, and electrode kinetics, and provide unique characteristics that are discussed in a later section (79,80).

1.3.1.3 Redox probes

Redox probes are electrochemically active molecules that follow specific electron transfer mechanisms allowing material characterisation. Outer-sphere redox probes such as ruthenium hexamine, are analytes in which the redox reaction does not involve chemical interactions with the electrode surface (69). The lack of adsorption or electrocatalytic steps, make these probes surface insensitive and ideal for studying the relative density of states (DOS) through electrode kinetics. For example, a comparison between carbon electrodes using ruthenium hexamine has been performed in which a higher density of edge planes results in faster kinetics attributed to a higher DOS (81,82). Moreover, electroactive surface areas can be determined from the current peaks of ruthenium hexamine using the Randles-Sevick equation. This has been increasingly relevant with the incorporation of nanomaterials into electrode surfaces. Inner-sphere redox probes are surface-sensitive analytes and thus are used for investigating the effect of electrode surface chemistry on ET kinetics. Potassium ferrocyanide, for example, is used to explore functionalization coverage of specific molecules. $Fe(H_2O)_6^{3+/2+}$ is widely used to provide information about oxygen-containing termination groups, in which faster kinetics are observed for greater oxygen-containing electrodes. McCreery, R. et al. (69) summarised some of the most common redox probes based on the type of ET mechanism are summarised in Figure 1.5.

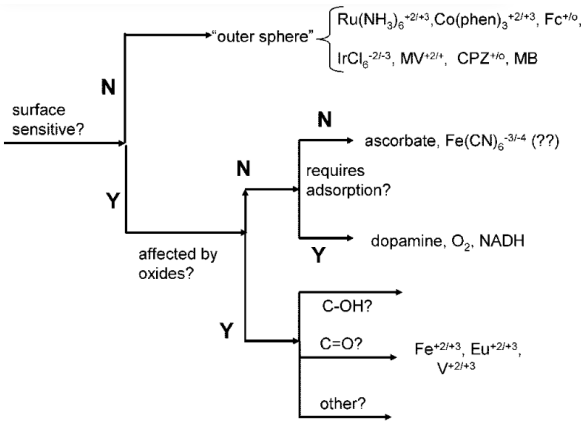

Figure 1.5 Classification of redox systems according to their kinetic sensitivity to particular surface modification on carbon electrodes. Reprinted with permission from American Chemical Society (69).

1.3.2 Analytical electrochemistry

Electrochemical sensors and biosensors are analytical devices that determine analyte concentrations by transforming biological responses to electrical signals through electrochemical reactions (83). While the terms “sensors” and “biosensors” can be used interchangeably, typically the term “biosensor” is most commonly used when a biorecognition molecule is attached to the electrode that serves as the recognition element to either increase selectivity and/or to enable the reduction or oxidation of the analyte. This biomolecule can be considered as the mediator between the electrode and the analyte of interest. The types of electrochemical biosensors may be classified by their biorecognition element which includes antibodies, enzymes, microorganisms, DNA, cells, or even a synthetic molecule capable of selectively attaching the analyte of interest. Other than this element, electrochemical sensors and biosensors both consist of an electrode, which serves as the transducer that converts the response of the bioreceptor or redox reaction directly at the electrode surface, into a quantifiable signal known as signalization (energy conversion), an electronic component that

makes the signal conditioning, such as a signal amplifier, and, finally, the display component, outputting the signal to the user through an interpretation system (Fig. 1.6) (84). As shown in Figure 1.6, similar components constitute other analytical devices, including optical and mechanical sensors.

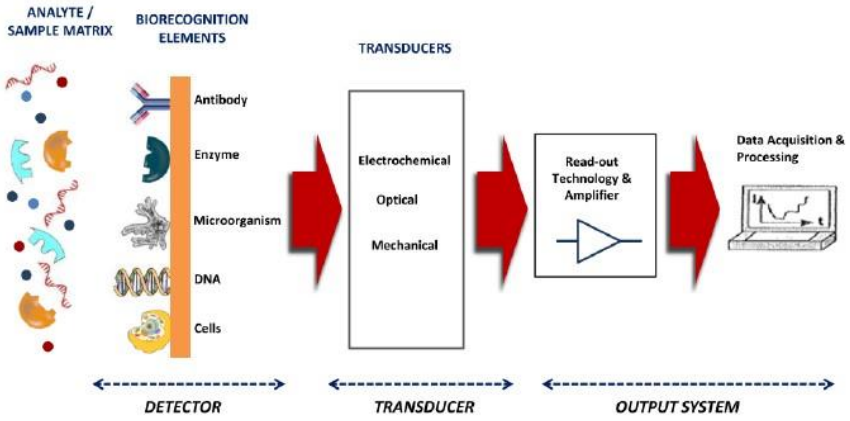

Figure 1.6 Components of a biosensor. Biorecognition element for the detection of an analyte, the transducer to translate the biological response into a signal, and the output system to allow the user to read the signal. Reprinted under the free to use Creative Commons license (http://creativecommons.org/licenses/by/3.0/) (85).

Sensors are used in a range of different applications including pollution monitoring (86), pesticide traceability (87), gas leakages (88), and other fields in which determining changes in concentration of an analyte is required. Furthermore, the ability of electrochemical sensors to measure and monitor analytes in real time has led to the development of point-of-care (POC) technologies (61,62). Specifically in the biomedical field, POC technologies have allowed the early detection of disease and, as a result, a better understanding of diseases as well as improved treatments (13,89). In addition, the development of non-invasive biosensing techniques has led to wearable devices that can monitor changes in analyte concentration in

available body fluids to also improve real-time monitoring and quality of life. Implantable biosensors have gained popularity due to their potential to increase patient comfort and reduce medical professional workload while measuring, in real-time, physiological changes (90). The content of available body fluids including urine, saliva, and tear fluid, have been investigated in search of useful and measurable biomarkers (91).

For example, secretions located in the back of the nose may be retrieved using a nasopharyngeal swab and used for testing upper respiratory tract infections. With the global pandemic Covid19, declared by the World Health Organization on the 30th of January 2020, there was an urgent need to develop early diagnostics techniques to slow down the spread and provide early care. Initial methods for diagnosis of the SARS-CoV-2 virus included the polymerase chain reaction (92) and the reverse transcription loop-mediated isothermal amplification (93) assays. Even though these techniques were non-invasive since they used nasopharyngeal swabs for sample collection and were highly sensitive with LOD of 1.5 x10^1 copies/mL and 1.0 x 10^2 copies/mL respectively, these techniques were time-consuming (1.5 – 3hrs) and expensive. Alternatively, the use of graphene enabled the development of a field effect transistor (FET)- biosensor with a reading time of <1 min and comparable LOD of 2.42 x10^2 copies/mL without the need for sample preparation (94). Upon binding of SARS-CoV-2 spike protein antigen to SARS-CoV-2 spike antibody immobilised onto graphene channel, the silicon substrate was p-doped). The resulting changes in current from an applied potential were correlated to the virus concentration. Regrettably, these electrochemical sensors were only demonstrated experimentally. Commercial availability was likely hindered by existing gaps in cost-effective large-scale synthesis, fabrication, and the development of affordable and portable potentiostats.

1.3.2.1 The use of nanomaterials for enhancing the performance of sensors and biosensors

Nanomaterials are currently used in sensors and biosensors to enhance their performance, as exemplified by the SARS-CoV-2 FET biosensor. While the chemical composition defines

certain properties, the size of nanomaterials compared to their bulk counterparts provides key features for their application in biosensing. For example, the nanostructure of zero-dimensional (0D) materials, such as nanoparticles (NPs) and quantum dots (QDs), endows the electrode surface area allowing more active sites for redox reaction or immobilisation of bioreceptors for higher particular affinity(95). One-dimensional (1D) structures, such as nanotubes have been used to enhance detection limits to the single molecular level since the diameters of nanotubes can be of similar size to biological molecules (96). The planar structure of two-dimensional (2D) materials allows the integration of electronics into wearable devices due to their unique mechanical properties such as high flexibility and mechanical strength (97).

2D materials such as MoS_2 and graphene have been widely utilised for the development of high-performance sensors and biosensors. However, these nanomaterials have some drawbacks that may limit the translation of these prototypes to feasible and commercially available devices. For example, MoS_2 has low electrical conductivity, and high hydrophobicity, and the functionalisation of its surface is quite challenging (98). Furthermore, as semiconducting channels due to their high band gap, they tend to have high electrical resistivity, and as such the signal from MoS_2-based biosensors results in high electrical noise. Graphene, however, has a small band gap allowing low electrical noise. Despite the unique properties of graphene, this 2D material also has some limitations such as multistep processing due to its lack of solubility in water and many organic solvents, as well as their low on/off ratio as FETs due to graphene's zero-gap structure (99). Other preparation approaches or further modification steps are required to synthesise graphene derivatives, such as graphene oxide (GO) and reduced GO (rGO), to ensure good dispersion and storage stability. Even though GO and rGO have shown promise in biosensing applications by overcoming some of graphene's limitations, the synthesis of bulk quantities of graphene derivatives with high-quality properties remains a challenge.

1.3.3 Electrochemical sensors for ophthalmic biomarkers

The detection of H_2O_2 as a by-product of the enzymatic oxidation of glucose for its monitoring has led to the development of glucose biosensor technologies (13). Electrochemical sensors have utilised solely amperometry and potentiometry for in-situ measurements of glucose. The designs using these transduction techniques have incorporated the enzyme glucose oxidase (GOx) as the biorecognition molecule. However, other enzymes, such as hexokinase and dehydrogenase-1-glucose derivatives, have also been explored in non-ophthalmic biosensing (100). The specificity of enzymes allows these proteins to be used as biorecognition elements in biosensors. The binding sites are formed due to a particular arrangement of the amino acids. GOx with the cofactor flavin adenine dinucleotide (FAD) (GOx-FAD^+) is immobilised on the electrode to oxidise β-D-glucose (101). As shown in equation 1, once the reduced form of FAD ($FADH_2$) reacts with oxygen, hydrogen peroxide (H_2O_2) is formed (Eq. 2). Amperometry measures the resulting current from the oxidation of H_2O_2 (Eq. 3) at a constant applied potential which can be proportionally correlated with the concentration of glucose in the sample (101). Potentiometry, specifically field-effect transistors FET biosensors, on the other hand, rely on the gated potential changes from the binding of charged biomolecules. Similar to the described mechanism, once glucose is oxidised, H_2O_2 is generated and further decomposed into oxygen, hydrogen ions, and electrons (Eq 1.3, 1.4, and 1.5) (102). As the charge carriers increase in the underlying semiconductor material with the increase of glucose, the FET drain current increases, allowing the quantification of glucose concentration.

$$GOx{-}FAD{+}{+}Glucose \rightarrow Glucolactone{+}GOx{-}FADH_2 \quad (1.3)$$

$$GOx{-}FADH_2{+}O_2 \rightarrow GOx{-}FAD{+}\ H_2O_2 \quad (1.4)$$

$$H_2O_2 \rightarrow 2H^+ + O_2 + 2e \quad (1.5)$$

1.3.3.1 Amperometric biosensors to monitor ophthalmic glucose

Incorporation of an amperometry biosensor to CLs to continuously monitor glucose in tears was first attempted as early as 1995 through the idea of developing flexible electrodes

(103). Challenged by the brittleness of wafer materials, such as glass or silicone, to develop flexible electrodes, Mitsubayashi et al. (103) used polytetrafluoroethylene membrane (PTFE) as the electrode membrane. Gold electrodes were deposited onto a hydrophilic-PTFE membrane followed by immobilisation of GOx. The non-uniform deposition of the conductive material, in this case gold, using a metal mesh with various gauges, was used to increase sensitivity. This microfabrication technology introduced surface defects to the electrode, allowing the GOx to better access the PTFE membrane, and as a result, higher currents from glucose oxidation were detected. However, the overall performance of the amperometric biosensor was reduced due to the increase in electrical resistance as a result of the reduced thickness of the gold layer from the non-uniform deposition of conductive material. Further work incorporated indium tin oxide (ITO) to produce optically transparent electrodes and avoid obstructing the view of the wearer; a key objective in ophthalmic biosensing (104). ITO is up to this day, a standard transparent conductive electrode (TCE) material used in many fields due to its high electrical conductivity and optical transparency (105). Therefore, an ITO-TCE for oxygen sensing was incorporated into a sandwich configuration between a gas-permeable membrane with a silver/silver chloride (Ag|AgCl) electrode and a non-permeable membrane. By immobilising GOx into the sensing region, the glucose biosensor achieved a linear detection of glucose concentration between 0.06 – 1.24 mmol/L.

The first fully working glucose-sensing CL was developed by Chu et al. and successfully tested *in vivo* on a rabbit in 2011 (Fig. 1.8a and b) (106). A platinum (Pt) electrode was coated onto a biocompatible and flexible polymer (PMEH) substrate, followed by immobilisation of GOx. This sensor achieved a linear range of 0.03 – 5.0 mM, which is appropriate for tear glucose monitoring. Key to the performance of this sensor was preventing enzyme leakage by coating the sensing region with PMEH, which also prevented the permeability of other chemicals. Alternatively, Parviz et al. (107) used a titania sol-gel membrane followed by a Nafion coating to avoid GOx detachment and retain enzyme activity for up to a week maintaining 80% of its initial current response after 2 days when stored in buffer at 4 ºC. The non-transparent materials

of choice for the electrodes, titanium (Ti), palladium (Pd), or Pt, were strategically located in the CLs avoiding the pupil (Figure 1.8c), and achieved an LOD of 0.01 mM which is well below the minimum concentration of glucose in tear fluid of a healthy person.

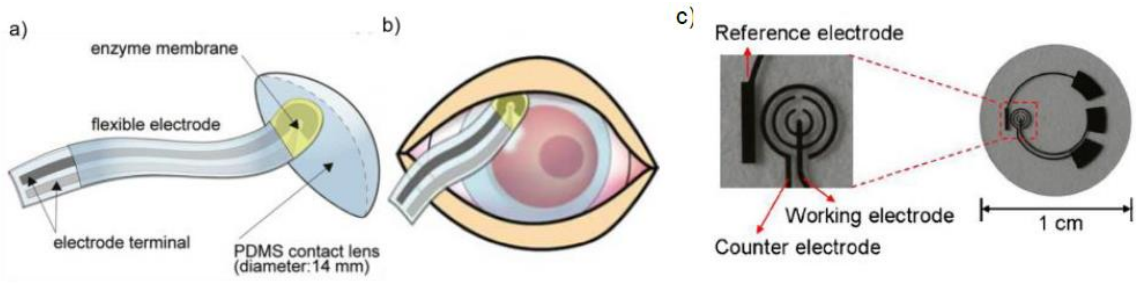

Figure 1.7. Incorporation of electrochemical sensors to contact lenses. a) Flexible electrodes were incorporated into the CLs, with GOx immobilised followed by a PMEH membrane to prevent enzyme leakage. b) *In vivo* glucose monitoring using the biosensing CLs. in a mouse eye. Reprinted with permission from Elsevier (106). c) Ti/Pd/Pt sensor components, including reference, working, and counter electrode. Reprinted with permission from Elsevier (107).

Similarly, Keum et al. (108) developed a non-transparent three-electrode configuration, using Pt and chromium (Cr) for the working electrode (WE), located strategically on CLs that achieved a linear range from 5 – 50 mg dl^{-1} (Fig. 1.9). Furthermore, it was demonstrated that interference of other molecules, including ascorbic acid, lactate, and urea, was negligible. The high stability of their Pt/Cr sensor, 63 days with <2% response deviation, was likely due to GOx being immobilised using chitosan and PVA, which are known to maintain an ideal microenvironment for enzyme activity. The main contribution of their work was incorporating a drug delivery system coupled with the glucose sensor as well as a wireless system that could remotely power, monitor, and control the smart CLs.

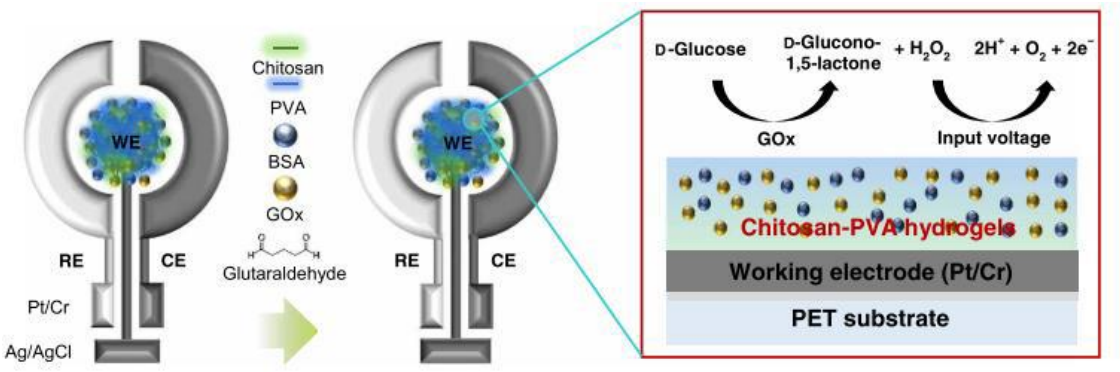

Figure 1.8. Glucose oxidase-based electrochemical sensor for the detection of glucose. Three-electrode (Working electrode (WE), reference electrode (RE), and counter electrode (CE)) amperometry biosensor for the ophthalmic detection of glucose. Glucose oxidase (GOx) was immobilised onto the WE using bovine serum albumin (BSA), polyvinyl alcohol (PVA), and chitosan. Reprinted under the free to use Creative Commons license (http://creativecommons.org/licenses/by/3.0/) (108)

1.3.3.2 Potentiometric biosensors to monitor ophthalmic glucose

In 2017, Kim et al. (102) for the first time incorporated a FET biosensor into CLs. Instead of using brittle materials, graphene was used due to its flexibility and high conductivity, as the channel material while graphene-silver nanowires (AgNWs) for the composite electrode. GOx immobilised onto the graphene channel using pyrene linkers allowed the oxidation of glucose in its presence (Figure 1.10). The biosensor achieved a LOD of 0.4 µM and a linear range of 1 µM – 10 mM, which is appropriate for tear glucose concentrations. An epoxy layer (SU8) is commonly used as a diffusive barrier to protect all the components, except for the sensing region (graphene channel), from harmful molecules. The sensor was stable for 24 hours, and in vivo measurements on a rabbit's eye showed successful measurements for up to 5 hours. The stability of this biosensor was enhanced to 48 h by the same group in 2018 by immobilising catalase (CAT) with GOx. Catalase can decompose H_2O_2 into water and oxygen molecules and as a result, decrease the degradation of GOx(109). Other improvements were the replacement of AgNWs with Ag nanofibers (AgNFs) which increased the mechanical properties of the material allowing the integration of a light-emitting diode. The light emitting

diode would light up if the glucose concentration were higher than 0.9 mM which is indicative of hyperglycemia. The LOD of this biosensor was 12.57 µM with a linear range from 0.1 to 0.9 mM.

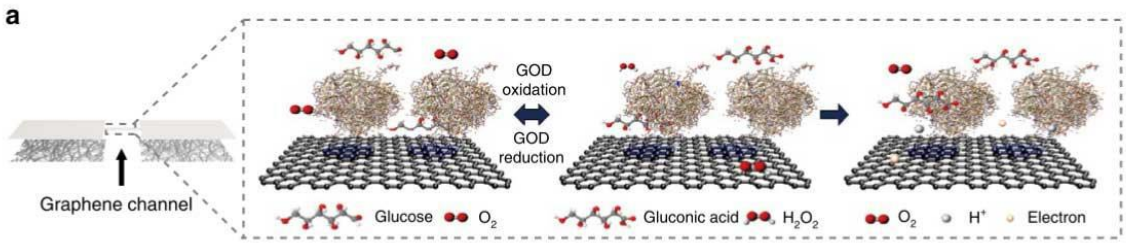

Figure 1.9. Principle of glucose detection in GOx functionalised graphene FET sensor. Reprinted under the free to use Creative Commons license (http://creativecommons.org/licenses/by/3.0/) (102).

In fact, Novartis, a pharmaceutical company, entered into a partnership with Google in 2014 to create innovative "smart" contact lenses using electrochemical sensors to assist diabetics in monitoring their blood glucose level (110). Unfortunately, the project was eventually stopped due to the lack of correlation of glucose concentration in tear fluid with blood glucose levels (111). Nevertheless, this project marked a significant milestone in the field of medical technology.

1.3.3.3 Electrochemical sensors for other ophthalmic biomarkers

Despite glucose contact lens sensors leading technological advancements in ophthalmic biomarker detection, a few reports have demonstrated their CL sensor potential for other biomarkers. Numerous enzyme-based electrochemical sensors utilise similar mechanisms, therefore it is expected that other metabolites can be detected using a similar approach. For example, by the incorporation of lactate dehydrogenase onto the Ti/Pd/Pt electrode using glutaraldehyde, the by-product of H_2O_2 was quantified and correlated to lactate concentrations in the tear fluid (112). The sensor achieved a sensitivity of 53 uA mM^{-1} cm^{-2} with a reliable response with other potential interferents. In 2020, a graphene field-effect transistor sensor enabled the real-time detection of cortisol (54). Cortisol is a hormone

produced by the adrenal glands during physiological or physical stress. Beyond monitoring cortisol levels, this work suggests an approach to better understanding the relationship between cortisol levels in tear fluid with disease. The immunosensor design consisted of the immobilisation of the monoclonal antibody through amide bonding on the surface of graphene. Combining a near-field communication chip and antenna, wireless charging, and signal to transfer to a smartphone was achieved. Another graphene field-effect transistor was developed to monitor chronic ocular surface inflammation through the detection of matrix metalloproteinase-9 (MMP-9) (113). A fragment of immunoglobin was immobilised onto the graphene channel for MMP-9 selective interaction. The source/drain electrodes consisted of a graphene/AgNWs structure, while the interconnects and the antenna were made of a network of AgNFs spun with AgNWs to provide additional conductive pathways. The NFC chip within the lens allowed control and powering from a smartphone.

Nanomaterials are under development within electrochemical sensors for contact lenses through integration into comprehensive systems. Beyond graphene, Ag NWs, and NFs, numerous other nanomaterials have potential use for electrochemical sensing applications in ophthalmic devices, driven by their combined optoelectronic and mechanical properties. While many nanomaterials demonstrate utility in electrochemical sensing, only a select few have been incorporated into contact lenses, possibly due to stringent criteria encompassing electrochemical performance, mechanical stability, optical transparency, flexibility and biological compatibility. Graphene, surpassing these criteria, extends its applications to other lens-based technologies, including a piezo-capacitive sensor for intraocular pressure monitoring and electroretinogram recordings (114,115). The limited utilisation of nanomaterials in contact lenses may stem from strict prerequisites for material and device properties. However, the potential use of other nanomaterials for these devices is promising.

1.4 MXenes

In 2011, 2D transition metal carbides and nitrides (MXenes) were first synthesised at Drexel University, USA (116). MXenes have a general $M_{n+1}X_nT_x$ formula in which M stands for a transition metal, X is a carbide or nitride, T represents the surface functional groups (for example, -OH, -O or -F) and n = 1- 4 (117). These surface terminations make MXenes hydrophilic in nature enabling their dispersion in multiple solvents and allowing their easy processing into thin films, coatings, or powders (118). This 2D family has grown rapidly with about 30 different MXene compositions experimentally synthesised in less than a decade and about 70 theorised to exist (119). The multiple compositions and structures of MXenes, their rich surface chemistry as well as the various synthesis and processing methods allow for tunability of properties, such as optoelectronic, magnetism, transport, and electronic properties, essential for multiple applications (Figure 1.11 a) (120–122). With a significant prominence in energy applications, the applications of MXenes keep diversifying and gaining importance throughout the fields of research (Figure 1.11a-c) (123). $Ti_3C_2T_x$, the first synthesised MXene, continues to be the most extensively researched due to its distinctive combination of properties, encompassing high conductivity, mechanical robustness, and chemical stability (Figure 1.11d). Its versatile characteristics make it a promising candidate for a wide range of applications, driving sustained interest and exploration in the scientific community.

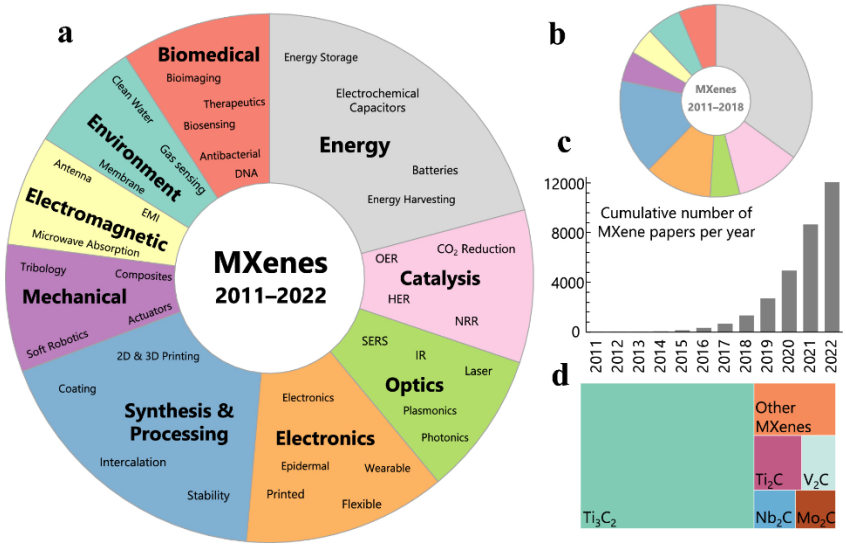

Figure 1.11 Explored applications and properties of MXenes over time (123). a) Pie chart depicting the distribution of publications across various MXene applications relative to the total number of MXene publications. A comparison with a similar chart from 2018 is shown in b). c) Bar chart illustrating the cumulative number of MXene publications per year. d) Comparison of the total publications on different MXenes, emphasising the dominance of $Ti_3C_2T_x$. Reprinted with permission from Springer Nature.

1.4.1 Properties and Applications of pristine $Ti_3C_2T_x$ electrodes

The rare combination of solution processing, high conductivity, and numerous fabrication approaches make MXenes attractive for multiple applications. Beyond the tunable electronic properties of the large family of MXenes, the combination of optical, mechanical, and biological properties enables MXenes to compete in a wide variety of applications with other nanomaterials. This section considers the properties of pristine MXene electrodes, and their applications.

1.4.1.1 Electrical properties

The high electrical conductivity of $Ti_3C_2T_x$ (<20 000 S cm^{-1}) (124) has led to its use in multiple applications with the significant benefit that MXenes can be used without the need for conductive additives or current collectors. For example, the use of pristine MXenes electrodes for wireless communication was first reported in 2017 (125). A. Sarycheva et al.(126) developed three types of devices, a dipole antenna, transmission line, and radio-frequency identification tags, to study the advantage of the high conductivity of MXenes over other nanomaterials. Even the thinnest (114 nm) spray-coated MXene antenna reached satisfactory return loss (< -10 dB), calculated by the scattering parameter S_{11}. An 8-µm thick $Ti_3C_2T_x$ antenna outperformed (-65 dB) any other reported nanomaterial-based antennas of similar thicknesses. While not fully understood, nanomaterials have been shown to overcome the depth skin limitation that metal antennas encounter when reducing their thickness. This

highlights the potential of MXenes over traditional metals and other nanomaterials to develop flexible and transparent high-performing antennas. Transmission lines, which transfer the signal and are essential elements for RF devices, made of spray-coated MXenes had 50-fold and 300-fold lower losses than that of graphene-based and silver paint-based devices. RFID tags using MXene antennas were also demonstrated. Impedance matching was controlled by the geometrical design attaining a reaching distance of up to 8 meters. The performance of MXene antennas has also been demonstrated for microwave frequencies, which may be implemented for 5G networks (127). Another application in which MXenes have overcome the skin depth limitation of metals when approaching the nanometre scale and surpassing their performance is in electromagnetic interference (EMI) shielding (128). The need for flexible microelectronics to have a protection barrier against the multitude of electromagnetic pollutants is of greater importance than ever considering the Internet of Things era. A $Ti_3C_2T_x$ spray coating of 40 nm in thickness achieved an electromagnetic interference shielding effectiveness (SE) of 21 dB which corresponds to the interception of > 99% interception of electromagnetic waves(129). Additionally, other compositions including Ti-, Mo-, and V-based MXenes, have also reached an EMI SE above 20 dB at 5 μm thicknesses.

1.4.1.2 Optoelectronic properties

The optical properties of MXenes have enabled MXenes to be used in optoelectronic applications(130). Spectroscopy analysis reveals different optical spectra of MXene compositions with absorption peaks varying in wavelength throughout the UV-to-NIR region (131). The absorption peak at around 780 nm of $Ti_3C_2T_x$ is attributed to transverse surface plasmon resonance adding plasmonic behaviour to the list of MXenes properties (132,133). Moreover, a single layer of $Ti_3C_2T_x$ only absorbs about 3% of visible light making it possible to develop transparent conductive electrodes (TCE) reaching an electrical figure of merit of 14(134). Pristine $Ti_3C_2T_x$ TCEs have been successfully used for developing a multitude of devices(130) including electrochromic supercapacitors (135), intraocular lenses (4) and light-emitting diodes (136).

1.4.1.3 Electrochemical properties

Their ability to intercalate a variety of ions including Li^+, Na^+, K^+, and Mg^{+2} enables MXenes to be used as electrodes for energy storage in batteries and supercapacitors (137). A study using *in situ* X-ray absorbance spectroscopy on $Ti_3C_2T_x$ demonstrated that titanium changes its oxidation state during electrochemical cycling suggesting a pseudocapacitive storage mechanism (138). Pseudocapacitive behaviour explains the high volumetric and gravimetric capacitance that MXenes have attained in aqueous electrolytes (137). Moreover, by controlling the chemical composition (X=Ti, Mo, Nb, etc), the number of layers (n), and surface terminations it is possible to optimise the capacitance of pristine MXene electrodes to tune the capacitance of MXenes. Extended cyclability has been reported for over 500,000 cycles while maintaining capacitance above 90% (139). Most work on MXenes for energy storage uses traditionally glassy carbon as a current collector. It is important to note that due to the lack of capacitive behaviour, the use of glassy carbon does not contribute to the excellent performance of MXenes as electrode materials for energy storage. However, studies have been performed to demonstrate the potential to use pristine MXene electrodes without the need for current collectors for energy storage. While the volumetric capacitance of Mxene-coated yarns (260 F cm^{-3} in 1M H_2SO_4), for example, is lower than that of $Ti_3C_2T_x$ vacuum-filtered electrodes (1500 F cm^{-3}) due to the yarn volume, it still surpasses that reported for carbon-coated yarn electrodes demonstrating the potential for wearable energy storage devices (140).

MXenes have also been used for electrocatalysis in hydrogen evolution reactions, carbon dioxide reduction reactions, and nitrogen reduction reactions (141). Density functional theory calculations have shown that the most electroactive sites of MXenes are the oxygen termination groups (142). Moreover, low adsorption free energy has been reported towards certain molecules and tunability in affinity can be achieved by the number of layers (n), surface chemistry, and composition of the Mxene(142). Another important advantage of MXenes towards industrialisation is that the elements of MXenes are significantly more Earth-abundant

compared to traditional electrocatalytic materials such as noble metals and therefore MXene electrodes become more cost-effective.

The combination of rich surface chemistry, electroactive surface area high electrical conductivity (up to 20,000 S cm^{-1}) (124) also make $Ti_3C_2T_x$ promising in analytical electrochemistry. For example, the increase in sensitivity to different analytes including redox probes (143), neurotransmitters (144) and environmental pollutans (143) has been attributed to the increase in electroactive surface area and electrical conductivity of the electrode material upon the addition of $Ti_3C_2T_x$. Yet, there is a lack of fundamental studies that explore the electron transfer kinetics at the pristine MXene surface. Most reported Mxene-based sensors are chemically modified electrodes in which MXene is used with varying components such as gold nanoparticles (145), silver nanoparticles(146) or other nanomaterials(147) on the surface of glassy carbon electrode(147). These constructs of electrochemical sensors make it very difficult to fully understand the contribution of MXenes to the faradaic response rising from the reduction or oxidation of the analyte of interest at the electrode surface.

1.4.1.4 Biological properties

Since 2017, when $Ti_3C_2T_x$ was shown to be cytocompatible (148), biomedical research in MXenes has significantly increased. The cytocompatibility of other MXenes compositions including Ti_2CT_x(149) Mo_2CT_x (150) Nb_2CT_x (151) and $Ta_4C_3T_x$ (152) has been demonstrated towards a variety of cell lines. Furthermore, thorough investigations have included *in vivo* studies that have demonstrated the potential to use MXenes in biomedical devices. For example, neuronal cells were incubated with a 200 nm-thick $Ti_3C_2T_x$ electrode used as a high-resolution neural interface (153). After a 7-day incubation period, the percentage of viable cells was the same compared to the polystyrene positive control. Furthermore, the ability of MXenes to be functionalised with multiple molecules has enhanced their dispersibility and stability in different solvents and allowed for improvement in their biocompatibility. For example, the modification of $Ti_3C_2T_x$ and Ti_2CT_x with collagen, a positively charged biomolecule, increased cell viability and reduced ROS production. The modification of $Ti_3C_2T_x$ with soybean

phospholipid produced an improvement in colloidal stability in various solvents including culture media. Due to the lack of stability in a biological environment, Nb_2CT_x flakes were surface-modified with polyvinylpyrrolidone (151). The steric hindrance of organic chains allowed the enhancement of colloidal stability in physiological environments. PVA has also been used to improve cytocompatibility. Mo_2C-PVA flakes up to a concentration of 400 ug mL^{-1} showed no significant cytotoxicity after 48 hr incubation towards breast cancer (4T1) and normal fibroblast (L929) cell lines. Moreover, PVA conjugation resulted in a pH-dependent biodegradation rate of Mo_2C-PVA flakes with an increase stability in acidic conditions favouring longer use as photothermal agents in acidic tumour microenvironments. Within an *in vivo* study carried out in 4T1 breast tumour model, the Mo_2C-PVA flakes remained in the body for 2.15 h before degradation, and even though there was retention of Mo in the liver and spleen, the Mo levels in these major organs decreased over time (150).

The potential of MXenes ©n the bi”medi’al field has been demonstrated by their use in diagnostic imaging, photo- and chemo-therapy, biosensing, and antimicrobial applications (154). For example, due to the higher photothermal conversion efficiency (30.6%) and higher extinction coefficient (25.2 L g^{-1} cm^{-1}) of $Ti_3C_2T_x$ compared to that of Au nanorods or graphene, $Ti_3C_2T_x$ flakes were used as photothermal agents for the ablation of tumours (152). Furthermore, the ability of MXenes to be conjugated has allowed their applications as drug carriers. After modification of the $Ti_3C_2T_x$ surface with soybean phospholipid, the anti-cancer drug doxorubicin was electrostatically adsorbed followed by hyaluronic acid encapsulation (155). The electrostatic adsorption of doxorubicin imparted stimuli-responsive drug release characteristics, triggered by the acidic microenvironment of tumours and temperature changes induced by radiation. MXenes have also been used as contrast agents for enhancing current diagnostic imaging. For example, in fluorescence imaging, MXene quantum dots have been utilised due to their high photostability and tunable wavelength. Alternatively, due to the high photothermal conversion, soybean phospholipid functionalised Ta_4C_3 flakes were used in

photoacoustic imaging for those diseases that do not exhibit photoacoustic contrast at early stages.

1.5 Gap in knowledge

In the realm of ophthalmic diagnostics integrated into contact lenses, the exploration of biomarkers has been constrained despite technological advancements. While glucose has been a primary focus, its suitability for diabetes monitoring is compromised due to the delayed reflection of blood glucose concentrations in real-time. The recent integration of electrochemical sensors onto contact lenses owes its progress to the incorporation of nanomaterials, particularly harnessing the optoelectronic capabilities of graphene and Ag NWs and NFs. These materials excel in transmitting visible light while establishing a conducive network for electron pathways. Despite these significant advances, a remarkable gap persists, given the multiple nanomaterials employed in electrochemical sensors including graphene derivatives, MXenes, and gold and silver nanoparticles.

The unexploited potential of MXenes represents a noteworthy oversight in electrochemical sensing. Despite extensive research on their electrochemical properties and documented success in energy storage applications, MXenes have yet to be systematically explored as pristine electrodes for electrochemical sensing. Moreover, the optoelectronic and mechanical properties of $Ti_3C_2T_x$, suggest their viability in developing transparent and flexible sensors for ophthalmic diagnostic devices. Preliminary reports indicate MXene'' feasibility for use as a transparent conductive electrode within an accommodating intraocular lens design(4). Biocompatibility assessment using an *in vitro* lens epithelial cell model underscores their compatibility in an ophthalmic environment associated with the lens. However, their assessment for corneal epithelial compatibility has not been established. Considering the electrochemical, optoelectronic, mechanical and biological properties of $Ti_3C_2T_x$, it was hypothesised that pristine $Ti_3C_2T_x$ can be incorporated as a flexible, transparent conductive

electrode onto a contact lens for electrochemical detection of biomarkers in the tear fluid, exemplified using hydrogen peroxide. The aim of this research was to demonstrate how the properties of $Ti_3C_2T_x$ can contribute to the development of contact lens diagnostics and $Ti_3C_2T_x$ suitability for these applications.

1.5.1 Research objectives

1. To synthesise $Ti_3C_2T_x$ MXene and fabricate a pristine electrode with a defined area for use in electroanalytical measurements.
2. To investigate the impact of material and electrode parameters in the electrochemical performance of pristine $Ti_3C_2T_x$ electrodes.
3. To optimise pristine $Ti_3C_2T_x$ electrode and the experimental parameters for the detection of a biomarker, hydrogen peroxide in simulated tear fluid.
4. To incorporate pristine $Ti_3C_2T_x$ electrode onto a contact lens without impacting its electrochemical performance.
5. To evaluate the compatibility of the integrated $Ti_3C_2T_x$ electrode on a contact lens with an ophthalmic environment.

2 Pristine $Ti_3C_2T_x$ electrode: synthesis, fabrication, and characterisation

2.1 Introduction

This chapter begins with the synthesis and characterisation of $Ti_3C_2T_x$ which is the foundation for a good-performing MXene electrode. The very first reported MXene in 2011 was developed using a top-down approach for synthesis (116). However, since then, bottom-up approaches have also been reported for the synthesis of Mo_2C and V_2C via chemical vapour deposition (156),(157). While chemical vapour deposition is an excellent method for producing high-quality large crystals of MXenes, this approach is limited to only a few specific MXenes and small quantities (158). Top-down approaches involving selective etching continue to be the most common in MXene research. In the following sections, MXene top-down synthesis approaches with a focus on $Ti_3C_2T_x$, solution processing, and characterisation are reviewed.

2.1.1 MXene synthesis and processing

2.1.1.1 Synthesis

MXenes can be synthesised from MAX phases with the formula $M_{n+1}AX_n$ and non-MAX phases materials (more than one 'A' layer) (137). These precursor materials are layered MXenes held together by layers of the A elements (11 to 16 group in the periodic table). The synthesis of MAX phases and non-MAX phases can take place in a pressureless inert atmosphere, by hot pressing, or in an isotactic pressing manner. Their formation mechanism is dependent on whether individual elements (M, A, X) or powder mixtures (MX or MA) are used (159). Reports suggest that when elemental powders are used, intermetallic intermediates are formed, followed by nucleation of carbon in the interstices. In contrast, the use of powder mixtures (carbides and nitrides) results in available C or N vacancies for M or A diffusion for the MAX phase formation.

The ability to selectively etch away the A layer from MAX phases arises from the difference in bond strength between the M-A and M-X layers (116). M-A layers are held together by metallic bonding, while the M-X layers have ionic/covalent bonding. Theoretical predictions have been made to estimate the exfoliation energy based on bond energy (160). Findings show that the

exfoliation energy is strongly related to the composition of the MAX phase including M- and X-element, and less so on the structure (n) of the MAX phase. The highest difference between M-A and M-X bond strength results in a lower exfoliation energy meaning easier exfoliation.

$Ti_3C_2T_x$ is typically synthesised from its parent material Ti_3AlC_2 (Figure 2.1). A common approach to chemically exfoliate the Al layers is by the use of hydrofluoric acid (HF) (116).The use of such strong acid enables the oxidation of A element in which the proton (H^+) is the oxidising agent and the F^- acts to solubilise the by-product (Al^{+3}). Similar exfoliant mechanisms are followed with different proposed methods including in-situ HF, alkali-, halogen- and molten-salt-based protocols (159). Once the A layer has been etched and exfoliated, the resulting material is multilayer mXene, where layers are held together via van der Waals forces arising from the interaction between surface terminating chemical groups introduced during etching. To achieve single to few layers of $Ti_3C_2T_x$, intercalation agents are used to delaminate multilayer mXene, these agents weaken the interaction between layers and with the help of mechanical agitation, separating them. Typical chemical intercalants include cations while solvents and organic molecules have been previously used as physical intercalants.

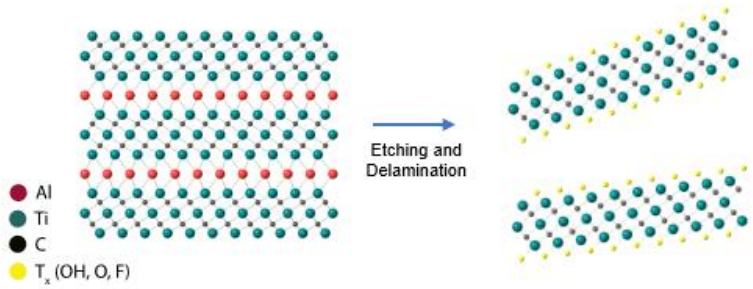

Figure 2.1. MXene synthesis via top-down approach. Ti_3AlC_2 MAX phase structure and $Ti_3C_2T_x$ MXene structure where A is aluminium (Al), M is titanium (Ti), X is carbon (C) and T_x are the hydroxyl, oxygen, and fluorine termination groups (OH, O and F)

Variation of the synthesis protocol for both the precursor material Ti_3AlC_2 and $Ti_3C_2T_x$ itself is the most important parameter for the successful synthesis of MXenes and the tailoring of its

characteristics. For example, large flake sizes are typically desired for highly conductive devices. To develop large MXene flakes, efforts in controlling three different parameters have been made over the past few years. (1) The size of the MAX phase crystal determines the largest size of MXene flakes that can be obtained. Therefore, the largest Ti_3AlC_2 MAX phases are usually pre-selected via particle sedimentation of sieving (161)·(124). (2) The mechanical stress applied during delamination is another factor that reduces the size of flakes. Therefore, soft delamination methods have been developed to avoid the breakage of flakes obtaining sizes up to 40 μm (162)·(124). (3) Over-etching is another occurrent issue that tends to reduce the size of flakes. This has been one of the main focuses of research into MXene synthesis, in which synthesis temperature, etchant concentration, and etching time have been optimised through experimental and theoretical studies. By controlling the synthesis parameters of the MAX phase, the quality of MXenes has also been improved resulting in enhanced oxidation stability. In 2021, the current gold-standard synthesis for Ti_3AlC_2 was proposed by modifying the ratio of elemental powder to include excess Al (124). The synthesised $Ti_3C_2T_x$ had enhanced conductivity (<20,000 S cm^{-1}) and enhanced oxidation stability of up to 10 months for $Ti_3C_2T_x$ colloids in water. Moreover, the quality of the carbon for the MAX phase has also been demonstrated to influence the quality of MXene and its stability. Finally, surface terminations can be controlled by the synthesis protocol of MXene. Typically, HF-containing protocols will result in -O, -OH, and -F terminations, in which the ratio will be influenced by the ratio of chemicals during etching.

2.1.1.2 MXene processing

The hydrophilic nature of MXenes originated from the surface terminations, and the high surface charge (-30 mV) make MXene colloids stable in water without any post-processing steps (137). This is an enormous advantage since as-synthesised MXene can be used to fabricate devices in a wide variety of ways. Depending on the application of the MXene electrode, a fabrication technique may be selected to attain the desired electrode properties. For example, for transparent and conductive electrodes, spin- or spray-coating may be the best

approach since these techniques enable sample homogeneity and controlled deposition of a few MXene layers (163,164). This is of extreme importance to attain continuous electron pathways without losing optical transparency. On the other hand, patterned MXene electrodes may be produced through screen-printing using masks or sacrificial layers to obtain microelectrodes with high-resolution (165,166). Digital printing including injecting printing and three-dimensional (3D) printing have been used for developing high surface area MXene structures (167,168). For coating 3D structures that act as scaffolds for MXene electrodes, such as for pressure sensors or wearable devices, dip-coating has shown to be the most efficient (140,169). Vacuum-filtering and blade-coating are methods where self-standing films can be produced with controlled thickness and aligned flake structures due to the gravitational force or applied shear force during processing, respectively (161). Obtaining highly conductive films largely relies on the quality of the MXene flake as well as their lateral size (124). However, it is also possible to reduce the weak interflake connection by the shear force applied during blade-coating to reduce film resistivity and increase film strength (161).

The range of fabrication techniques that have been used to develop high-quality pristine MXene electrodes are in part due to the ease of control of the rheological properties of the MXene colloidal solution. A thorough study into the viscous and viscoelastic properties of single- and multilayer- $Ti_3C_2T_x$ solution has provided guidance to tailor MXene ink properties for specific manufacturing approaches through the manipulation of flake size and concentration (170). For example, when the viscosity modulus dominates the flow properties, observed in dilute solutions of single-flake MXenes, manufacturing that involves a high processing rate, such as spin- and spray-coating, is favourable. Contrastingly, those manufacturing approaches that require high elasticity at low frequencies, such as inkjet printing, may use higher concentrations of MXene so that upon printing the higher interaction between particles may be enough for the MXene structure to hold itself. Another approach would be to reduce the boiling point of the MXene ink so that upon printing the structure can self-sustain. For this reason, solvent exchange is another approach to modify the MXene ink formulation and extend the number of

processing techniques that can be used to fabricate MXene electrodes. Several solvents including ethanol, dimethyl sulfoxide, N,N-dimethylformamide, and propylene carbonate have been used to disperse MXenes resulting in high stability colloids (171). It has been demonstrated that organic solvents can be used to attain a nematic liquid-crystals of MXenes. This is relevant for the development of, for example, MXene fibres in which the formation of MXene liquid crystal is critical for wet-spinning aligned structures to attain high conductivity (172). Moreover, the solvent exchange can be performed through simple redispersion of dried MXene flakes in the desired solvent.

Relevant for industrialisation, is the ability to scale the production of MXene electrodes cost-effectively. To achieve this, the scalable synthesis of MXenes needed to be first addressed. An advantage of MXenes over other nanomaterials is that they are commonly produced from a top-down approach, as previously discussed. The solution-processing required for MXene synthesis can be applied to traditional chemical engineering processes making MXenes attractive to industrial companies such as Murata Manufacturing Co. Ltd. (173). In 2020, the first large batch (50 g) of $Ti_3C_2T_x$ was produced maintaining the structure and high-quality properties of MXenes synthesised at a lower scale (174). As a result, the bulk production of high-quality MXene electrodes for commercialization has become attractive. For example, the large-scale fabrication of blade-coated MXene films and MXene-coated yarns was demonstrated by producing samples larger than 1 meter long with conductivities exceeding 15000 S cm^{-1} and 7500 S cm^{-1}, respectively (161). Moreover, as the world is entering the era of the Internet of Things (IoT), wearable and portable devices are in the spotlight of electronics research. The good mechanical properties and biocompatibility of MXenes have attracted attention for developing flexible and biocompatible electrodes. Additionally, the good adhesion of MXenes to fabrics has been shown to withstand washing cycles which is relevant to translating wearable electrodes to real-life applications (175).

2.1.2 MXene characterisation

Material characterisation has been crucial for the development of material synthesis and processing methods, and their application in various fields. While the chosen characterisation techniques should be relevant to analyse specific properties of MXenes, certain key techniques are performed as standard routines along their synthesis. In the following section, general techniques, as well as relevant techniques for this thesis, will be discussed, along with how they characterise M'ene's physical, chemical, optical, and electronic properties.

2.1.2.1 X-ray diffraction

Interrogating the MXene and its precursor material with incident X-rays provides crystallographic information and confirmation of MXene synthesis. MAX phases have a hexagonal crystal structure which they inherit from MXenes. As shown in Figure 2.2, the c-lattice of Ti_3AlC_2 accounts for two $Ti_3C_2T_x$ structures and two layers of Al. In the case of MXene, it is the MXene community itself that has adopted a similar terminology in which the c-lattice parameter considers also two MXene flakes together with their surface termination and intercalated molecules. By determining the c-lattice parameter important information about MXene synthesis, intercalation mechanisms, and interlayer spacing can be determined.

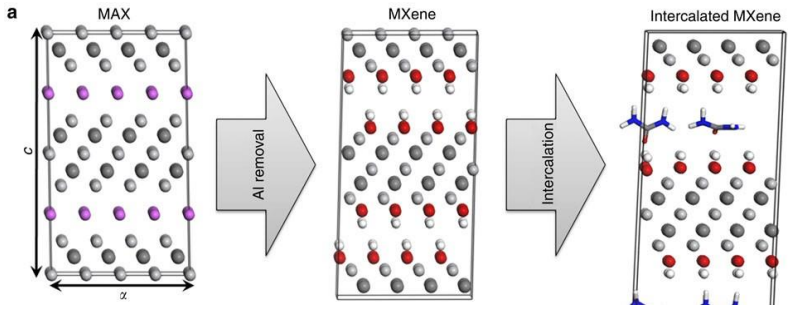

Figure 2.2 The crystallographic structure of a) Ti_3AlC_2 MAX phase and b) $Ti_3C_2t_x$ MXene, with relevant labels of XRD terminology including c-lattice parameter, d-spacing, and interlayer spacing. Reprinted with permission from Springer Nature (176) .

Considering the anisotropic structure of MAX and MXene, upon powder texturing or flake alignment (via vacuum filtering) the 00l peaks are overemphasised in the scattering spectra.

The 00l peaks relate to the c-lattice parameter. A negative shift of the 002 peak between MAX and MXene samples, is attributed to an increase in interlayer spacing from the etching of the A layer, the gain of the surface terminations, and the intercalated molecules including water. This is the standard method to confirm the successful synthesis of delaminated MXene. The 002 peak is used to determine the c-lattice parameters using the Miller indices relationship for hexagonal crystal shown in equation 2.1. In which the d-spacing (d) is calculated using the relationship between scattering angle and wavelength (Bragg's law) and the location of the 002 peak. Typically, Cu radiation is used as the source and therefore the wavelength to calculate the d-spacing is 1.57 A. Due to the straightforward and non-invasive determination of the c-lattice parameters of MAX phases and MXenes which enables the confirmation of MXene synthesis and delamination, XRD is one of the most common techniques used to monitor step-by-step MXene synthesis.

Equation 2.1. Relationship between Miller indices of a hexagonal crystal structure with the d-spacing, a-, and c-lattice parameters.

$$\frac{1}{d^2} = \frac{4}{3}\left(\frac{h^2 + hk + k^2}{a^2}\right) + \frac{l^2}{c^2}$$

2.1.2.2 Scanning electron microscopy

Scanning electron microscopy (SEM) imaging, is a standard characterisation of MXene to visualise the material. Considering the numerous studies that present images of the material at every stage of its synthesis, it is easy to identify some key characteristics of delaminated MXenes that can support material characterisation. An accordion-like structure is characteristic of multilayer MXene as the Al layers have been etched away and there is a certain degree of increase in interlayer spacing. However, an impactful publication by M. Shekhirev et al., highlighted that while it is common to see this structure, a more compact structure can also be observed for multilayer MXene. Once MXene is delaminated, the stacking of single layers in self-standing films or coatings can be observed at high magnifications, and in certain cases, it can resemble closely the MAX phase structure. Moreover, SEM of single flakes is

usually performed to accurately determine the flake size, confirm delamination, or observe any defect such as breakage or taring usually rising from harsh etching conditions.

An additional energy-dispersive X-ray spectroscopy (EDS) detector can provide further information about the chemical composition of the sample when performing SEM. When a secondary electron beam is shone on a sample, electrons in the inner shells are excited leaving a hole behind. When valence electrons fill the vacancies in the inner shells, energy in the form of x-ray is released. An EDS spectrum is developed by measuring the energy of emitted photons by the sample. EDS should only be used as a complementary and qualitative analysis of the transition metal and identification of impurities.

2.1.2.3 Four-Point Probe

The four-point probe is a non-destructive technique typically used to determine the conductivity of thin films when the thickness is known. Four probes are placed in a linear arrangement in which a current is passed between the outer two probes while the inner two probes measure the change in voltage. Following Eq 2.2, the instrument calculates and provides the sheet resistance which then can be converted to conductivity using Eq. 2.3.

Equation 2.2 Sheet resistance equation, where I is the applied current, ΔV is the voltage measured by the inner probes.

$$R_s = \frac{\pi}{\ln(2)} \frac{DV}{I}$$

Equation 2.3 Conductivity equation where R_s is sheet resistance (ohms) and t is the thickness in (m)

$$\sigma = R_s t$$

Conductivity values of $Ti_3C_2T_x$ coatings or films are a good indication of the quality of the films as it has been previously highlighted that conductivity is impacted by flake defects. Therefore, 4-point probe measurements are typically performed as a quality check after MXene synthesis. Especially when $Ti_3C_2T_x$ is used as a conductive material or electrode, which is the

case for this work, reporting their conductivity serves as a confirmation that an adequate material has been synthesised.

2.1.2.4 Dynamic Light Scattering

Dynamic light scattering (DLS) also known as photon correlator spectroscopy is a technique used to measure the hydrodynamic radius of nanoparticles in solution. It illuminates the sample and with a photodetector measures the scattering intensity fluctuations to determine their Brownian motion using a correlation function. Using the Stokes-Einstein equation (Eq. 2.4), it correlates the diffusion coefficient (D) of the particles to their radius (r). As shown below, D is dependent on the absolute temperature (T) and the dynamic viscosity (ɳ).

Equation 2.4 Stokes-Einstein Equation. Relationship between the diffusion coefficient (D), and the hydrodynamic radius (r) of colloid particles.

$$D = \frac{k_B T}{6\pi \eta r}$$

While DLS assumes a spherical particle, a study performed by Maleski et al. confirmed that the hydrodynamic radius determined using DLS is indicative of the length of MXenes flakes. Since then, DLS has been safely used as a good estimation of the flake size distribution in MXene colloidal solution.

2.1.2.5 Ultraviolet-visible spectroscopy

Ultraviolet-visible (UV-vis) spectroscopy is another optical technique that provides meaningful information about a material. It is an absorption or reflectance spectroscopy that uses light in the ultraviolet (190-380 nm) and visible (380-750 nm) regions to excite electrons to a higher energy state (electronic transitions). The instrument used in this technique is called a UV-vis spectrophotometer and it calculates the absorbance by comparing the light transmitted through the blank sample to the light transmitted through the analyte-containing sample.

In the case of MXenes being plasmonic materials with characteristic absorption peaks, UV-vis spectroscopy can be used for MXene identification. For $Ti_3C_2T_x$, the absorption peak located

around 780 nm is attributed to a plasmon resonance. Therefore, after MXene synthesis, recording the UV-vis spectra of the sample can serve as a complementary confirmation that MXene has been successfully synthesised and delaminated. This characterisation can also be useful during processing, to confirm that MXene has been successfully incorporated into a substrate.

Additionally, UV-vis spectroscopy can serve as an analytical technique for the quantification of MXene concentration using Beer-Lambert Law (Eq. 2.5). According to Beer-Lambert Law, absorption (A, unitless) is proportional to the molar absorptivity of the material (ε), the pathlength of light (l) through the sample and its concentration (C). While the molar absorptivity of $Ti_3C_2T_x$ MXene is reported in the literature, it is recommended to perform a standard curve after one synthesizes MXenes. The concentration for the standard curve samples can be determined by weighing a vacuum-filtered film and dividing it by the volume of the colloid filtered. This allows a better estimation of the molar absorptivity of the following batches if the same synthesis method is followed. The ability to determine the concentration based on the UV-vis spectra has encouraged research to use UV-vis spectroscopy to monitor oxidation and degradation from the material. This is possible considering that when $Ti_3C_2T_x$ degrades it transforms to TiO_2 and/or agglomerates and sediments at the bottom of the vial, resulting in an overall decrease in MXene concentration. Beyond, colloids, UV-vis spectroscopy can also be used to determine the thickness of thin coatings in future work. The thickness of the standard curve samples is usually determined using SEM imaging.

Beer-Lambert Law:

$$A = \varepsilon b C \qquad \text{Equation 2.5}$$

Most recently, UV-vis spectroscopy has been used in conjunction with electrochemical techniques to understand some oxidation mechanisms during the charge and discharge of energy storage devices. While MXene research using UV-vis spectroscopy is expanding, their

use as MXene identification and concentration determination remains as a standard characterisation during synthesis and processing.

2.1.3 Gap in knowledge

While $Ti_3C_2T_x$ synthesis, processing, and characterisation are well established in the literature, the selection of protocols for electrode fabrication is application-dependent. Tailored to this thesis, the synthesis and characterisation of the $Ti_3C_2T_x$ electrodes were developed using protocols predictive to give the best electrochemical performance for sensing. Moreover, while pristine MXene electrodes have been used for a variety of electrochemical applications, they have not been explored as electrochemical sensors for analyte quantification. Therefore, it was hypothesised that utilizing the high-Al MAX phase for MXene synthesis, would result in electrical conductivities appropriate for the development of pristine $Ti_3C_2T_x$ electrodes for analytical electrochemistry. This work aimed to develop a reproducible electrode design that would enable a study involving solely the electrochemical activity of MXenes in the following chapters.

2.1.4 Research objectives

1. To synthesise single $Ti_3C_2T_x$ MXene flakes via HF-HCl etching from high-Al MAX phase and characterise accordingly.
2. To design pristine $Ti_3C_2T_x$ in which parameters can be modified to be studied against electrochemical performance in future chapters.
3. To demonstrate robust fabrication protocol for reproducible electrochemical performance throughout electrode batches.

2.2 Materials and Methods

2.2.1 Materials

- Hydrofluoric acid (HF, 48 wt. % in H_2O, ACS reagent, US)
- Hydrochloric acid (HCl, 12 M, purity ≥ 37%, Sigma-Aldrich, US)
- Lithium chloride (LiCl, purity ≥ 99.9%, Acros Organics, USA)
- Ti_3AlC_2 MAX phase (A.J. Drexel Nanomaterials Institute, Drexel University, USA)
- Deionised (DI) water
- Potassium chloride (KCl, 99.0 – 100.5%, ACS reagent, UK)
- Polystyrene cuvettes, 1 cm, (Sigma-Aldrich, UK)
- Hexaammineruthenium (III) chloride ($(Ru(NH_3)_6Cl_3$, 98%, Sigma-Aldrich)
- Hydrophilic polyvinylidene difluoride (PVDF) membrane (0.22 mm, Merk Chemicals LTD)
- Polyimide electrical tape (PI, RS Components LTD, UK)
- pH test strips (Merck, US)

2.2.2 MXene synthesis

2.2.2.1 Etching

$Ti_3C_2T_x$ flakes were synthesised from the high-aluminum Ti_3AlC_2 MAX phase using the HF-HCl etching method. The Al layer was first chemically etched from the MAX phase. The etchant consisted of a mixture of 12 M HCl, DI water, and 50 wt% HF in a volume ratio of 6:3:1. Once the etchant was prepared, 1 g of MAX phase was added slowly (1 g/5 mins) to the etchant in a polyethylene bottle. A magnetic stirrer was added, and the bottle was lightly capped to allow gas release. The solution was left to stir for 24 h at 35 degrees Celsius (^oC) at 400 rounds per minute (rpm). The resulting acidic solution was centrifuged for 5 mins at 3,500 rpm obtaining a clear supernatant which was decanted into a waste container and the sediment was redispersed in DI water. This cycle was repeated until the pH, measured with a pH strip,

reached 6. After the last centrifugation run, the supernatant was decanted, and the neutralised sediment was kept for delamination.

2.2.2.2 Delamination

For delamination, 1 g LiCl was mixed with 50 mL of DI water. The 0.5 M LiCl solution was used to redisperse the neutralised sediment. The solution was left stirring for 24 hours at 400 rpm. The solution was collected and through a series of centrifugation runs at 3500 rpm with the first lasting only 5 mins and the following lasting 1 hr, delaminated MXene was washed. The supernatant of the last wash containing single-layered $Ti_3C_2T_x$ was decanted and stored in a closed container in the fridge until use.

2.2.3 Colloidal solution processing and characterization

2.2.3.1 UV-vis spectroscopy

The UV-vis spectrum of as-synthesised MXene using recorded with the Evolution 201 UV-vis spectrophotometer (Thermo Scientific, USA) with a path length of 10mm. This technique was also used to develop a calibration curve of MXene colloidal solutions with a series of concentrations (10 - 40 μg/mL) to determine the extinction coefficient (molar absorptivity) for the $Ti_3C_2T_x$ solution. With a initial MXene solution of known concentration (described in Section 2.2.4.1) in DI water, a series of dilutions were performed. Then, 1 mL of each sample was pipetted into a quartz cuvette and measured from 200 – 1000 nm. DI water was used as a blank for all measurements.

2.2.3.2 Flake size isolation

To isolate the different flake sizes contained in the as-synthesised MXene colloidal solution, various centrifugation steps were performed. First, the as-synthesised MXene solution was split into four 50-mL centrifuged tubes and centrifuged for 30 mins at 4,000 rpm. The resulting supernatants were all carefully decanted into the same container and stored in the fridge until characterised. Then, the sediments were redispersed in 50 mL of DI water and centrifuged for 30 mins at 3,500 rpm. The supernatants were stored and the sediments were

redispersed as previously described. Similar steps were taken for consecutive centrifugation runs of 2,500 rpm, 1,500 rpm, and 500 rpm. The sediments, containing MAX phase, or multilayer MXene, of the last centrifugation run of 500 rpm were discarded.

2.2.3.3 Flake size reduction

To reduce the size of $Ti_3C_2T_x$ flakes, bath sonication and probe sonication (50% amplitude, 8:2 sec ON: OFF) were performed for different duration times (detailed in results) using an ice bath to avoid heating the MXene colloidal solutions.

2.2.3.4 Dynamic Light Scattering

To estimate flake size dimensions and determine the polydispersity index, DLS was used with a 90-degree scattering optics spectrometer was utilised (Zetasizer Nano ZS, Malvern analytical, UK). The sample of interest was diluted until visually translucent and 1 mL of a MXene sample was pipetted into a polystyrene cuvette. Three measurements were averaged for each sample.

2.2.4 MXene film fabrication and characterisation

2.2.4.1 Vacuum-filtered films

To fabricate self-standing films, a known volume of solution was vacuum assisted filtered using a PVDF membrane. Depending on the volume of the MXene solution filtrated, the filtration took from 2 to 6 hours. The resulting film was left in the desiccator overnight to further dry before characterization.

2.2.4.2 Determination of concentration

The MXene film was removed from its filtration paper, and weighted. The MXene colloidal concentration was calculated by dividing the weight of the dried film (mg) by the volume of the solution filtered (mL).

2.2.4.3 Thickness determination

The thickness of films was measured using a digimatic micrometer (absolute d2, Multitoyo). 5 measurements were taken per film and averaged.

2.2.4.4 Conductivity

Sheet resistance was measured using a 4-point probe (Jandel Engineering LTD). These parameters were used to calculate the conductivity of each MXene film following Equation 2.2 and 2.3.

2.2.4.5 X-Ray Diffraction

X-ray diffraction (Rigaku Smartlab) was performed in pressed MAX powder as well as MXene film for alignment using CuKalpha radiation (λ =1.54 A).

2.2.5 MXene electrode fabrication and material characterisation

2.2.5.1 Fabrication

Rectangles of 15 mm in length and varying widths (2, 3, and 4 mm) were cut from the $Ti_3C_2T_x$ self-standing film. Two pieces (6 x 20 mm^2 and 6 x 10 mm^2) of Kapton tape were used to encapsulate the MXene films. To develop one electrode design, named basal-plane-electrode (BPE), the smaller piece of Kapton tape (6 x 10 mm^2) had been previously hole-punched to expose a MXene area of circular geometry with varying diameters of 2, 3, and 4 mm. To fabricate the other electrode designed, named edge-plane electrode (EPE), once the MXene film was encapsulated by the two pieces of Kapton tape, a cross-sectional area of MXene was exposed by performing a cut parallel to the width of the MXene film. Scanning electron microscopy measurements

2.2.5.2 Scanning electron microscopy

The sample preparation for SEM (Zeiss Supra 50VP) was done by cutting a vacuum-filtered film and placing it either horizontally or vertically to the bolt sample holder to obtain a top or cross-sectional image, respectively. Before measurement, the samples were platinum-coated. The measurements were performed at an electron height tension of 5 kV in high vacuum mode.

2.2.5.3 Energy Dispersive X-Ray Spectroscopy

Chemical compositions of the MXene electrodes were determined using an Oxford Instruments Aztec EDS system, equipped with an Oxford Instruments X-Max 80 X-Ray detector. For SEM imaging and EDS mapping, the SEM/EDS was operated at 10 kV accelerating voltage at high vacuum.

2.3 Results and Discussion

2.3.1 MXene synthesis and characterisation

The successful synthesis and delamination of $Ti_3C_2T_x$ was confirmed using X-ray diffraction (XRD, Figure 2.3). The increase in *d*-spacing from 9.7 to 12.4 angstroms (A), after the removal of the Al layer, calculated from the (002) peak at 9.12° and 7.13°, respectively, is attributed to the termination groups (T_x) of delaminated $Ti_3C_2T_x$ and intercalated water molecules. In addition, only (00*l*) peaks are observed for the film sample, indicating that the $Ti_3C_2T_x$ sheets are all aligned along the basal direction with no residual Ti_3AlC_2 or other impurities present (177). This confirms the removal of the Al layer, delamination of single MXene flakes with lithium ions, and suitability of the produced film to study the $Ti_3C_2T_x$ flake orientation.

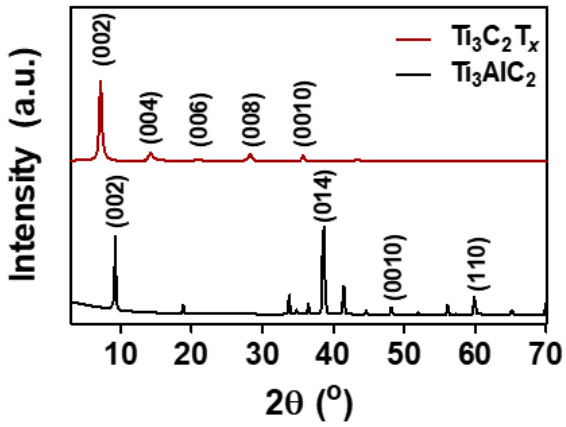

Figure 2.3. X-ray Diffraction spectra of Ti_3AlC_2 and $Ti_3C_2T_x$. Reprinted with permission from (299). Copyright 2024, American Chemical Society.

2.3.2 Optical characterisation

The optical properties of MXenes are another way to identify the material. As shown in Figure 2.4, Ti_3C_2Tx shows a characteristic peak at 770 nm as well as around 330 nm. J. K. El-Demellawi et al. attributed the peak around 770 nm to be due to the plasmon resonance, while the peak around 330 nm is from interband transitions using electron energy loss spectroscopy (178). The UV-vis spectra of the different concentrations (10, 15, 20, 25, 30, 35, and 40 µg/mL) of as-synthesised colloidal solution in DI water are shown in Figure 2.4a.

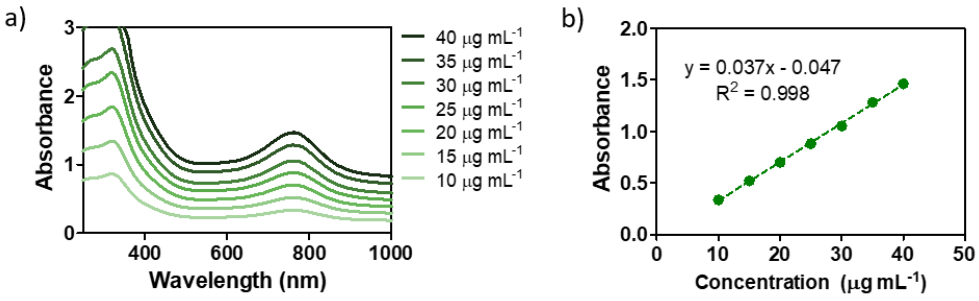

Figure 2.4. Characterisation of $Ti_3C_2T_x$ colloids in water using UV-vis spectroscopy. a) UV-vis spectra of delaminated $Ti_3C_2T_x$ in DI water with concentrations ranging from 40 to 10 µg mL^{-1} b) Calibration curve of $Ti_3C_2T_x$. The absorbance at local maxima (770 nm) is plotted against their respective colloidal concentration (µg mL^{-1}). A linear trend line was fitted (R^2 = 0.998) and its formula is shown.

The local absorption maxima at 770 nm of the different known concentrations of $Ti_3C_2T_x$ were used to make a calibration curve as shown in Figure 2.4b. Having calculated the extinction coefficient to be 37.5 L g^{-1} cm^{-1}, which corresponds to the slope of the calibration curve, it is possible using Beer-Lambert's Law (Eq. 2.5) to determine the concentration of other $Ti_3C_2T_x$ colloidal solutions by measuring its maxima local absorbance and knowing the optical path length (L).

2.3.3 Flake size reduction and characterisation

Difficulties in sorting out different flake sizes limit the investigation of size-dependent properties[6]. The effect of the flake size of $Ti_3C_2T_x$ on electrochemical and optical properties has

been explored by Maleski et al. (179), allowing the enhancement of transparent and conductive electrodes, for example. Since part of this study will focus on investigating the properties of $Ti_3C_2T_x$, once MXene was synthesised and characterised through the UV-vis spectra, the isolation of different flake sizes was the next step.

The first approach considered was taking advantage of the differences in particle sedimentation rates due to the different mass and size of individual flakes. The size distributions of the supernatants obtained from multiple centrifugation steps are shown in Figure 2.5a. Also shown in Figure 2.5b is the resulting z-average (nm), which is the intensity-weighted mean of the hydrodynamic radius of the particles in solution, and the polydispersity index (dimensionless).

a)

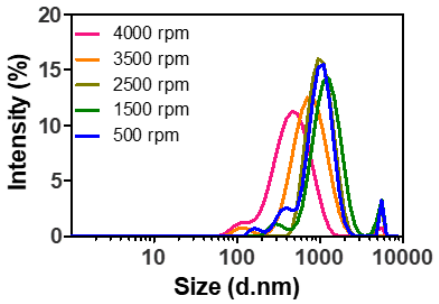

b)

Processing	Z-average (nm)	PDI
4000 rpm	374 ± 8	0.311 ± 0.028
3500 rpm	613 ± 6	0.249 ± 0.014
2500 rpm	1028 ± 19	0.359 ± 0.013
1500 rpm	1276 ± 20	0.391 ± 0.003
500 rpm	1332 ± 21	0.551 ± 0.103

Figure 2.5. Characterisation of $Ti_3C_2T_x$ flake size separation using dynamic light scattering. a) Flake size distribution of supernatants obtained from centrifugation runs (mean of 3 measurements, n=1). b) Table providing the processing steps in the centrifuge (4000 – 500 rpm) for 30 mins of each supernatant and its respective z-average (nm) and polydispersity index (PDI).

It is worth noting that DLS assumes spherical particles; fortunately, correlations to microscopy-derived size distributions allow the determination of flake length and width without expensive and time-consuming scanning electron imaging. An SEM analysis made by Maleski and coworkers determined that $Ti_3C_2T_x$ flakes have a length-to-width size ratio of 1.6:1 (179,180). Furthermore, a comparison between SEM images and DLS measurements of $Ti_3C_2T_x$ determined that the width size is closest to the Z-average. Therefore, thanks to this study, it is

possible to use the DLS measurement to closely approximate the MXene flake's true size and distribution.

Results (Figure 2.5b) showed that the higher speed in the centrifuge would separate smaller flake sizes and an increase in flake size was observed with decreasing speed, as expected. The polydispersity index indicates how broad is the size distribution; a PDI larger than 0.7 indicates a very broad distribution and suggests that it is not suitable for DLS measurements (181).The relatively high PDI (>0.3) of some of the batches could have been reduced by more centrifugation steps for longer periods, since for this study it would be best to have the lowest PDI possible for accurate size-dependent properties determination. However, a problem encountered with the centrifugation steps approach for isolating flake sizes is the low amount of material for each flake size obtained.

In need of larger and more consistent amounts of material per flake size, a different approach was taken. It is possible to break flakes into smaller particles by the introduction of energy into a colloidal solution. Furthermore, by varying the amount of energy and the time applied, breaking the particles into different sizes can be controlled. The amount of energy can also be varied by using different instruments. A high-shear mixer, also known as a homogenizer, uses a rotor at various speeds (3,000 – 4,000 feet/min) for flake size reduction. The bath and the probe ultrasonicator use power (20-40 and 200-400 kW, respectively) to generate acoustic energy to break flakes by cavitation (182) These three instruments were used for breaking the flakes into different sizes as described in materials and methods. The resulting colloidal solutions were characterised using the DLS. Figure 2.6a shows the size distributions and Figure 2.6b their respective Z-average (nm) and PDI.

a)

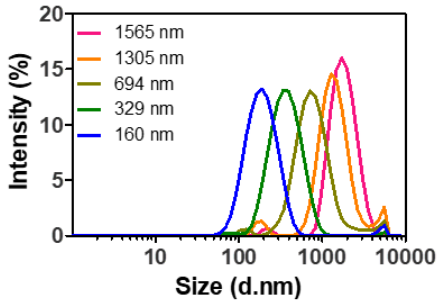

b)

Processing	Z-average (nm)	PDI
As-synthesized	1565 ± 13	0.252 ± 0.07
20 min H + 35 min BS	1305 ± 24	0.364 ± 0.03
60 min BS	694 ± 10	0.343 ± 0.01
5 min PS	329 ± 4	0.221 ± 0.02
135 min PS	160 ± 1	0.302 ± 0.01

Figure 2.6. Characterisation of $Ti_3C_2T_x$ flake size reduction using dynamic light scattering. a) Flake size distribution of the MXene colloidal solutions obtained from the size reduction method (mean of 3 measurements, n=1). b) Table providing the processing steps using a homogeniser (H), a bath sonicator (BS), and a probe sonicator (PS) and their resulting Z-average (nm) and polydispersity index (PDI).

Results (Figure 2.6) showed that with increasing time of the applied energy, the flake size was reduced significantly from 1565 nm to 160 nm, as desired. Considering that the resulting colloidal solutions of different flake sizes had the same volume and concentration since only mechanical or acoustic energy was introduced, this approach was chosen for size reduction and isolation of flake sizes for all the experiments.

2.3.4 Electrode fabrication and characterisation

The self-stacking of flakes during vacuum-assisted filtration of MXene colloidal solution results in a semi-oriented structure of MXene flakes (Figure 2.3). When sufficient flakes are stacked on top of each other, self-standing MXene films are produced. The conductivity of the vacuum-filtered film resulted to be 14,327 S cm^{-1} which is characteristic of highly conductive $Ti_3C_2T_x$. Here in, a straightforward protocol for the fabrication of bare electrode MXenes using self-standing film is proposed (Figure 2.7). Kapton tape is utilised to encapsulate the MXene electrode to maintain a constant surface area which is essential for reporting in analytical electrochemistry(66). For the first electrode design (Figure 2.7b), the desired electrode area is determined by the diameter of the hole punched through the Kapton tape. Due to the stacking of flakes during filtration, the basal plane of MXene flakes is

predominantly exposed to the environment. Therefore, these electrodes are referred to as BPE. Interested in shining light on the differences in electroactivity between basal- and edge-plane, as well as flake orientation, the second electrode designed exposes the cross-sectional area of the film (Figure 2.7c). This is achieved by first encapsulating the MXene film with Kapton tape, followed by a cut perpendicular to the basal plane. The geometrical surface area is then approximated by the length (3 mm) and thickness (5 µm) of the MXene electrode. This electrode design is then referred to as the EPE. As highlighted in Figure 2.7, these electrode designs allow easy control of certain material parameters, including the size of the flakes conforming to the electrode, electrode thickness and geometrical surface area (d or l) relevant for Chapters 3 and 4.

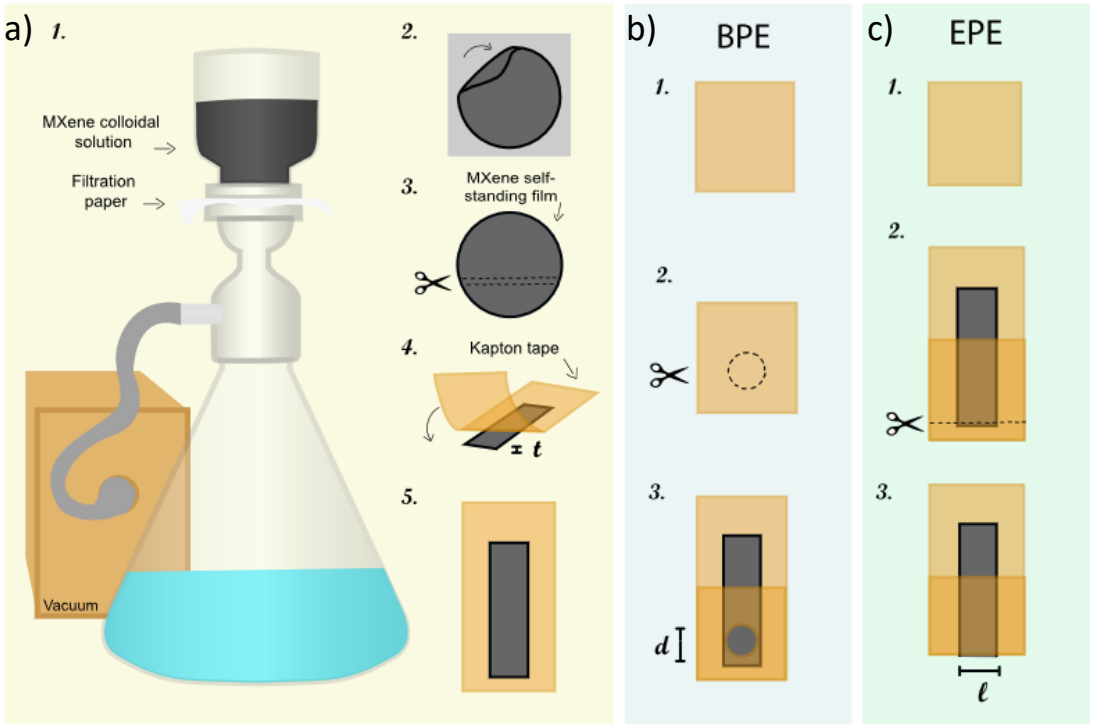

Figure 2.7 Fabrication of pristine $Ti_3C_2T_x$ electrodes. (a) Schematic of fabrication protocol of basal-plane electrodes (BPE, b-3) and edge-plane electrodes (EPE, c-3) using vacuum-assisted filtration for MXene self-standing films (a-1) and Kapton tape (a-4) for electrode encapsulation.

Moreover, relevant to the thesis was the development of pristine $Ti_3C_2T_x$ electrodes to understand their potential without the contribution of glassy carbon electrodes. As shown in Figure 2.7, the fabrication of these electrodes only required Kapton tape and a vacuum-filtered film of the electroactive material of interest. Kapton tape was selected as the substrate of choice for encapsulation due to its flexible structure, which enabled it to take advantage of the strong mechanical properties of MXene vacuum-filtered films. Optical images of the MXene working electrode show the flexible electrode structure developed (Figure 2.8).

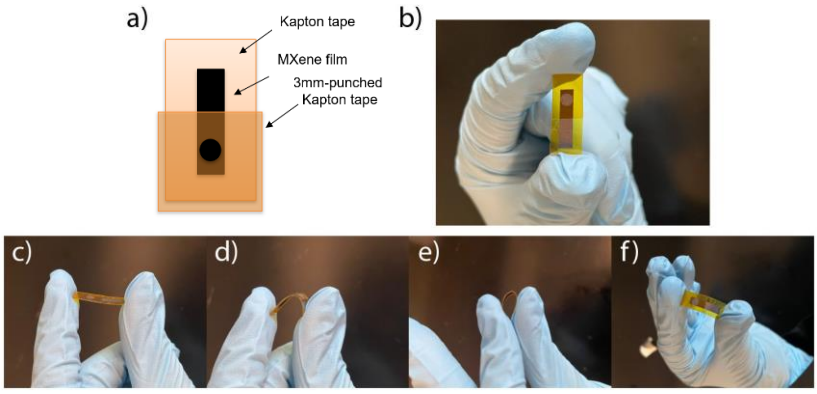

Figure 2.8. Flexibility visualisation of basal-plane electrode design. a) Schematic of MXene working electrode components. b) Photograph of $Ti_3C_2T_x$ working electrode. Series of photographs bending the MXene electrode (c-e) and showing how it recovers to its initial shape without any visual damage (f).

While many processing methods of MXene colloidal solutions may attain an orderly structure of MXene flakes, vacuum filtration was selected for simplicity of fabrication, handling, and thickness control. Figure 2.9a shows the SEM of the BPE. Due to the resulting arrangement of MXene flakes, the electrode is composed of mostly titanium atoms of the outer MXene layers represented with EDS mapping (Figure 2.9b). The high carbon content shown in the EDS spectra (Figure 2.9c) rises from the Kapton tape encapsulating the MXene electrode (Figure 2.9b). The stack of flakes can be visualised in an SEM micrograph of the edge-plane electrode,

or EPE (Figure 2.9d), in which edges are exposed to the surface. EDS mapping reveals prominent sports of C atoms at EPE (Fig 2.9e). The EDS spectra present the content of Ti and C atoms of the EPE (Figure 2.9f). Moreover, chlorine, fluorine, and oxygen were identified (Figure 2.9c,f) and attributed to the termination groups acquired during wet synthesis. Aluminium (Figure 2.9f) is likely a sample holder contaminant as it was not observed on BPE.

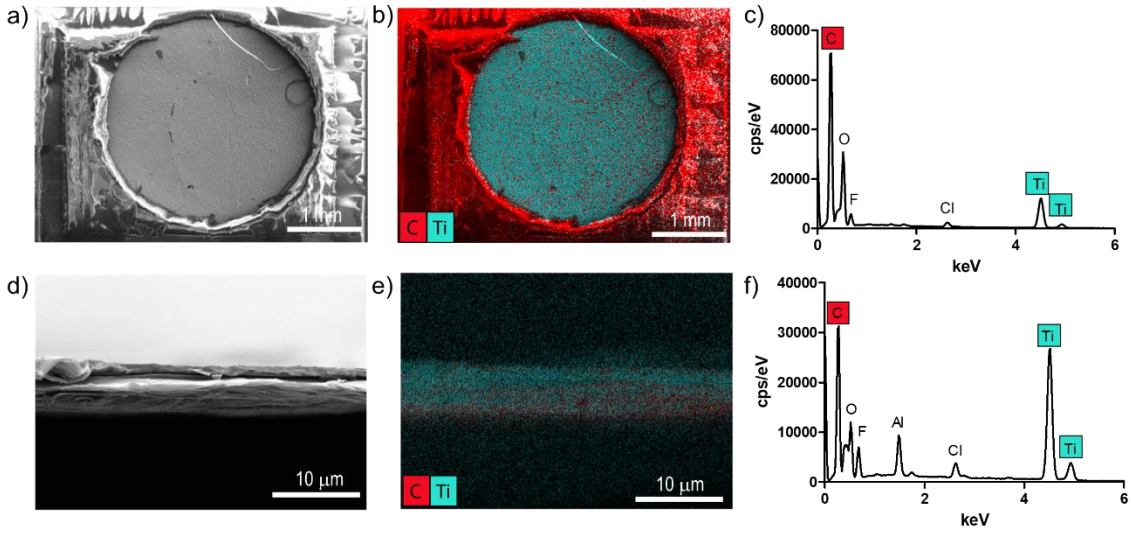

Figure 2.9. Material characterisation of pristine $Ti_3C_2T_x$ electrodes. Scanning electron microscopy images of (a) basal-plane electrode (BPE) and (d) edge-plane electrode (EPE). Overlapping energy dispersive X-ray spectroscopy EDS) map of C and Ti of the (b) BPE and (e) EPE with their respective spectra (c and f). Adapted with permission from (299). Copyright 2024, American Chemical Society.

2.3.1 Uniformity of film and electrode reproducibility

To test the suitability and reproducibility of these electrodes, we studied the uniformity of the MXene film from which electrodes were made. The schematic in Figure 2.10 shows the location from which the electrodes (optical photograph) were obtained. The representative cyclic voltammograms of these electrodes in ruthenium hexamine are shown in Figure 2.10b. The characteristic redox peaks of ruthenium hexamine appear around -0.2 V as expected. No significant difference ($p<0.05$, n-6) was observed for the cathodic peak current (Figure 2.10c) and ΔE (Figure 2.10d). This suggests that a uniform film was developed when using vacuum-

assisted filtration. While only a limited number of electrodes can be fabricated from one single film, the potential of using other methods of processing should be assessed to develop numerous electrodes from the same processing batch. It has been shown that blade coating allows the manufacturing of large-area films with a well-defined thickness.

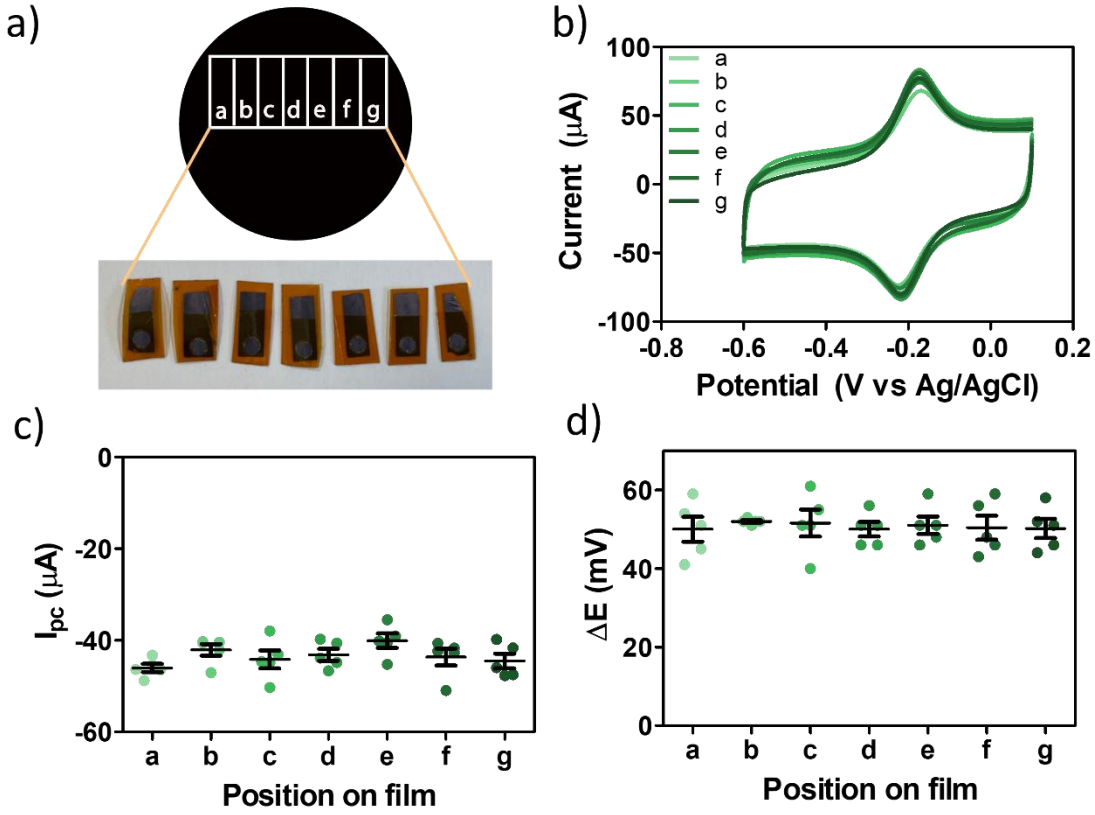

Figure 2.10. Impact of film uniformity on electrode reproducibility. a) Schematic of a film indicating electrode location and optical image of the corresponding electrodes. b) Representative cyclic voltammograms in 5 mM ruthenium hexamine and 1 M KCl at 20 mV s^{-1} of electrodes in different locations. c) Cathodic peak current (I_{pc}, uA) and d) peak separation potential (ΔE, mV). (Mean ± standard error, $p<0.05$, n=5, one-way ANOVA with Turkey's comparison). Reprinted with permission from (299). Copyright 2024, American Chemical Society.

The variation between different batches of these MXene electrodes was also investigated. Figure 2.11 shows that no significant difference in cathodic peak current and ΔE was observed

between different batches of MXene electrodes. These findings highlight that MXene electrochemical sensors can be made with high reproducibility.

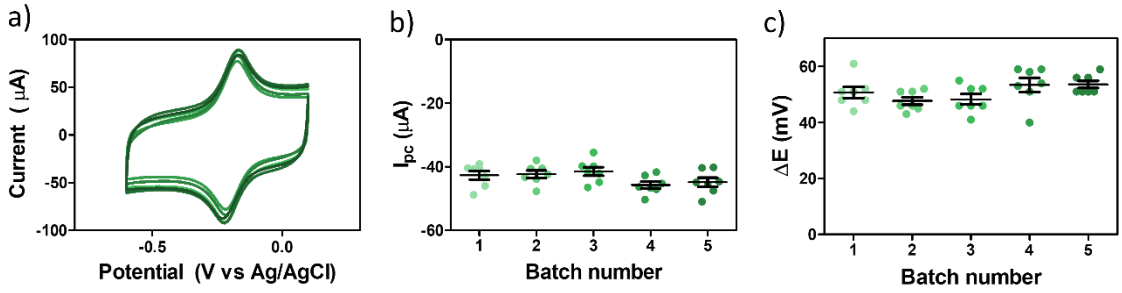

Figure 2.11 Batch reproducibility of $Ti_3C_2T_x$ electrodes. a) Cyclic voltammograms of representative $Ti_3C_2T_x$ electrodes from 5 fabricated batches. Cyclic voltammetry was run in 5 mM ruthenium hexamine in 1 M potassium chloride at 20 mV s^{-1}. b) Reduction peak current (I_{pc}, mA) and (c) redox peaks separation (ΔE, mV) of cyclic voltammograms. (Mean ± standard error, $p<0.05$, n=5, one-way ANOVA with Turkey's comparison). Reprinted with permission from (299). Copyright 2024, American Chemical Society.

2.4 Conclusion

The importance in understanding the impact of synthesis and processing was emphasised as critical aspects for conducting studies and developing MXene-based devices. The selected synthesis method, HF-HCl etching and LiCl delamination, was performed successfully to produce single $Ti_3C_2T_x$ flakes with high conductivity (14,327 S cm^{-1}). This was confirmed through numerous characterisation methods including XRD, SEM, EDS, DLS, UV-vis spectroscopy, and 4-point probe measurements. Additionally, the proposed electrode design for $Ti_3C_2T_x$ enables the manipulation of electrode dimensions, surface area, thickness and flake orientation, relevant for future chapters. The successful use of pristine $Ti_3C_2T_x$ electrode for electrochemical measurements was demonstrated by the observed redox peaks of ruthenium hexamine. Finally, reproducibility of the electrode fabrication protocol within and between electrode batches was confirmed. This will enable the systematic exploration and optimization

of both the material and electrode parameters specifically tailored for electrochemical sensing applications.

3 Pristine $Ti_3C_2T_x$ Electrodes Enable Flexible and Transparent Electrochemical Sensors

3.1 Introduction

The successful incorporation of platform diagnostics into contact lenses relies on the introduced technology not hindering the primary design features of the lenses. Contact lenses need to be flexible, since 'soft' polymers are used in their production, and they need to be optically transparent. As demonstrated in Chapter 2 $Ti_3C_2T_x$ MXene can be used to manufacture a flexible electrode, however its electrochemical performance under bending conditions is yet to be assessed. Moreover, it is also important to assess if an optically transparent electrode can be produced.

The use of MXenes has contributed significantly to the advancement of wearable and portable devices due to their unique properties including high conductivity, tailorable optical properties, and high mechanical stability(183–185). This has been key as we enter the era of the Internet of Things requiring flexible, transparent, and self-powered technologies for niche applications (186,187). Some examples of MXene-based devices include wearable antennas (188), flexible sensors (189–191), accommodating intraocular lenses (4), smart windows (192) and triboelectric nanogenerators for self-powering devices (193) and human-machine interfaces (194,195). Transparent, flexible, and wearable energy storage devices have also been reported due to MXene's excellent capability of ion intercalation and pseudocapacitance properties (196–198). Despite the electrochemistry field taking advantage of the optoelectronic and mechanical properties of MXenes, these are yet to be fully explored for electrochemical sensing.

3.1.1 Flexible electrochemical sensors

With the increasing interest in wearable and portable devices, the field of electroanalytics has also explored flexible electrochemical sensors (199–202). For example, textile and epidermal electrochemical sensors have gained significant attention from the biomedical field for the continuous monitoring of diseas (200,203) Multiple bodily fluids can be used for non-invasive monitoring of biomarkers for disease, however, this requires

electrodes to have different mechanical properties that traditional electrode materials, such as metals, do not possess (199). One approach to developing a flexible electrochemical sensor is through the incorporation of rigid electrodes into flexible substrates. This is the current approach to incorporating electronics into contact lenses as described in Section 1.3.3 (106–108). However, the use of rigid electrodes in flexible substrates limits their use in certain applications such as tattoo-sensors due to the mismatch of mechanical properties of skin and rigid electrodes (203). Current strategies for the development of flexible electrodes include the use of polymer-nanomaterial composites and layered structures. For example, nanomaterial-based inks have been used to design electrodes onto flexible substrates such as paper, polyethylene terephthalate (PET), PI, PMMA, and polyurethane (204). Another approach is to develop conductive fibres by electrospinning or using nanomaterial coatings on natural or synthetic fibres to construct flexible networks as working electrodes. Conductive fibres can also be spun to form yarns to weave or knit wearable devices (200). Alternatively, it is possible to directly dip coat or screen-print onto cloths or fabric using conductive inks (200). While generally nanomaterials are used for enhanced electrochemical performance, 1D and 2D nanomaterials can also contribute to the mechanical stability (199). Due to their high aspect ratio, these materials have another advantage i.e. a lower percolation threshold than NPs, and therefore less material is needed to form conductive networks (199). In particular, 2D materials have been reported to have a low contact resistance between flakes, resulting in highly conductive electrodes. This property is, however, highly dependent on fabrication protocol, electrode composition, and flake alignment.

Several flexible electrochemical sensors have been developed by combining the unique properties of different nanomaterials. For example, a flexible polyolefin film was modified with graphene oxide followed by electrodeposition of Au-NPs for the detection of uric acid (UA) and dopamine (DA). The LOD achieved were 10 nM and 1.47 μM for DA and UA respectively (205) Similar LODs (<1.5 μM) were reported for AA, UA, and DA with wide linear ranges (10 – 1000 μM) using an MXene-MoS_2-modified carbon fibre paper (206). These

analytes have also been detected by self-reducing Au-Pd NPs onto a previously MXene drop-casted laser-inscribed porous graphene (LSG). The flexible electrode achieved similar linear ranges and low LOD to the previous work (207). A similar approach utilized a mixture of $Ti_3C_2T_x$ -CuO was deposited onto carbon cloth for the detection of cadmium (Cd^{+2}) and lead (Pb^{+2}) ions (208). The wide linear range for Cd^{+2} (4 – 80, 80 – 800 μM) and Pb^{+2} (4-1200 μM) was achieved with low LOD, 0.3 and 0.2 μM, respectively (208). Other environmental pollutants, harmful to human health such as phytoregulator a-naphthalene acetic acid (NAA) in a linear range of 0.02 – 40 μM and a LOD of 1.6 nM can be electrochemically detected by flexible MXene-based electrodes (209). Another sensor for NAA consisted of a hybrid of phosphorene and $Ti_3C_2T_x$ that was deposited onto a laser-induced porous graphene (LIPG) structure. While most 2D-based electrochemical sensors were reported to be stable over multiple measurements (<10) and reproducible with only <5% change in current response, all the aforementioned reports failed to test them against stress, which is key for reliable electrochemical measurements of flexible electrodes.

There are several methods to characterize flexible devices including bending. The main two parameters that determine flexibility are the bending angle (theta) and the bending radius of curvature (R). G.-F. Li and colleagues demonstrated only a 3% variability in the current response of an electrode before and after 100 bends for the non-enzymatic detection of glucose(210). However, they failed to report the bending angle. This study used a layered Pt/PVA-$Ti_3C_2T_x$/Pt-$Ti_3C_2T_x$ structure combined with a multifluidic design achieved an appropriate linear range of detection (0-8 mM) for glucose in sweat without interference from sweat accumulation. Another article reported no significant difference in the oxidation current response of rifampicin, an anti-tuberculosis drug, using an MXene-based electrode while bent under measurement compared to its natural state (211). This sensor was developed by the incorporation of TFA and Nb_2C onto carbon cloth, however, the bending angle was not reported either. Another study that successfully investigated the impact of bending on electrochemical performance was the flexible graphene/Ag NPs for the detection of H_2O_2 (212). This work

showed that the sensitivity decreased after bending the electrode 20 times around a 5 mm in diameter cylinder. Only by investigating the impact of bending on the electrochemical performance of electrodes, the relevance of work on flexible sensors can be assessed. Moreover, considering the difference in stress applied at different bending angles, it is important to report either the bending angle or the bending radius of curvature, which is rarely presented in the Methods of most published work. In this manner, a straight comparison of electrode composition can be performed and optimised for the real-life application of electrochemical sensors.

In summary, the use of nanomaterials has facilitated the creation of high-performing and mechanically stable electrochemical sensors. Despite MXenes being employed as coatings or additives to enhance electrochemical performance in various flexible sensors, the exploration of their application as pristine materials remains unexplored. Utilising pristine $Ti_3C_2T_x$ sensors could unlock a new frontier in sensor technology, offering unprecedented possibilities for flexible sensors in niche applications such as contact lens diagnostics. Further research in this direction holds great potential for advancing the capabilities of electrochemical sensors in diverse applications.

3.1.2 Transparent electrochemical sensors

The optoelectronic field of research has led the development of transparent electrodes for applications in solar cells, touch screens, smart windows, and light-emitting diodes (213). Most recently, the development of transparent electrochemical sensors has begun to gain momentum in new fields due to the exciting opportunities that these can provide. For example, in biological research, the ability to simultaneously track biochemical fluctuations in cells while observing their morphological changes enables a better understanding of cell behaviour (214). In wearable devices, one application is a seamless electrochemical sensor that can monitor glucose in sweat, which would add to the development of skin electronics (215). The growing interest in imperceptive electronics underscores the significance of unobtrusive and visually discreet wearable devices, particularly in enhancing the user experience, comfort, and

societal integration of assistive technologies (216). In neuroscience, the use of transparent electrodes has enabled synergistic therapeutic and diagnostic methods which could be extended to electrochemical detection of neurotransmitters with the appropriate material selection (217). Integrating transparent electrochemical sensors into windows, glasses, or contact lenses could allow for the detection of environmental or physiological changes without compromising the user's vision. These are a few examples that demonstrate the desire to develop transparent electrochemical sensors as the next generation of analytical detection.

Transparent or semi-transparent electrochemical sensors are typically fabricated using one or more of the following components: typical transparent conductive oxides (TCOs) such as Sn-doped In_2O_3 (ITO), conductive polymers such as polydimethylsiloxane (PDMS), or nanomaterials, most commonly CNTs. For example, a transparent sensor for the detection of

the oxidative stress biomarker 8-hydroxydeoxyguanosine was achieved by deposition of Au nanotriangles and Pt NPs onto ITOs (218). While TCOs have demonstrated potential for transparent electrochemical sensing, their relatively high cost limits their use in several applications. Instead, the combination of nanomaterials with polymers is more commonly reported. For example, a transparent sensor for the detection of hydrogen peroxide was developed by transferring CNTs onto PDMS before complete polymerization followed by an electrodeposition of Au NPs (214). Depending on the amount of CNTs deposited, the transmittance of the electrode varied between 90 % to 50 %. This allowed direct visualization of the cells and monitoring of morphological changes during stretching. A similar approach was performed to detect hydrogen sulphide by using Au nanowires instead of NPs to increase the mechanical and optical properties of the sensor. Other polymers such as poly-(3,4-ethylenedioxythiophene) (PEDOT) and poly(ethylene terephthalate) (PET) have been used as substrates for CNT-based transparent sensors for hydrogen peroxide and dopamine (219),(220),(221).

Electrospun fibres and metal meshes have also been used to develop transparent sensors. To monitor glucose in sweat non-invasively, an electrode was made of electrospun nanofibers

made with polyvinyl alcohol (PVA), β-cyclic oligomer (CO), 1,2,3,4-butanetetracarboxilic-acid (BTCA) and Au NPs with a coating of glucose oxidase (GOx) immobilised with β-CO. The resulting sensor achieved a linear range between 0.1 – 0.5 mM with a sensitivity of 47.2 μA mM and LOD of 0.01 mM. Au-mesh network has also been used as a substrate for the immobilisation of nickel alkylthiolate ($Ni(SR)_2$) for the non-enzymatic detection of glucose(222). This transparent network achieved a sensitivity of 675.97 μA mM^{-1} cm^{-1} and a LOD of 2.2 μM. Furthermore, a comparison was conducted between Au-mesh and FTO, and it was found that Au-mesh performed significantly better. When using Au-mesh, the detection of human blood glucose levels fell within a wide linear range, indicating superior electrocatalytic performance compared to FTO. Another metallic network consisting of Ni-mesh, was decorated with Au NPs and PEDOT:poly(styrene sulfonate) (PSS) for dopamine detection with 85% optical transmittance (223). This work highlighted the importance of monitoring neurotransmitter release upon neuron activation which can be achieved using transparent sensors.

While there is still a limited number of publications reporting on transparent electrochemical sensors, the evident benefits and the pressing need for their development become apparent as interdisciplinary technological innovations advance at a rapid pace. The use of zero- and one-dimensional nanomaterials such as metal NPs and CNTs, have been key for achieving high sensitivity and low LOD while maintaining high optical transmittance. However, 2D materials, specifically MXenes, have yet to be explored for transparent electrochemical sensors, considering these have achieved reasonable figures of merit in optoelectronics and demonstrated excellent electrochemical properties. It is essential to highlight that these distinctive properties have been utilised in various applications, including energy storage and electrochromic devices, which further supports their potential use in transparent electrochemical sensors.

3.1.3 Gap in knowledge

Despite progress in the field of transparent and flexible electrochemical sensors, only a few reports have focused on incorporating these into contact lenses. Notably, only graphene, Ag NWs and NFs have been used in these attempts lacking an evaluation of sensor performance under bending conditions and without an assessment of the impact of transparency on electrochemical performance (Section 1.3.3). Whilst MXenes have shown great potential as transparent and electrochemical electrodes for numerous applications, their use as electrochemical sensors has yet to be investigated. Numerous studies on MXene-based electrochemical sensors have reported high sensitivity to various analytes including redox probes, neurotransmitters, and environmental pollutants (143,144) Current approaches in their development involve either drop-casting a MXene composite containing other nanomaterials such as Au and Pt nanoparticles or employing a layer-by-layer deposition onto current collectors (146,147,224) However, conventional current collectors, like screen-printed electrodes (225,226) and glassy carbon (227,228) are bulky and rigid, limiting their use as flexible sensors. Alternatively, using soft and conductive substrates like carbon cloth, hydrogels or graphene electrodes enables the development of flexible sensors and their incorporation onto wearable devices (189,190,210,229) This has been demonstrated for skin patches allowing non-invasive sweat analysis (210) However, these sensor designs lack transparency due to opaque components within the electrodes constraining MXene-based electrochemical sensors in niche applications such as optoelectronics, specifically contact lens diagnostics. To overcome this limitation, it was hypothesised that pristine $Ti_3C_2T_x$ electrodes, known for their stacked layers with high mechanical properties (161) remarkable conductivity (230) and optically transparency (231) could be employed. This study aimed to explore the mechanical stability and optoelectronic properties of pristine $Ti_3C_2T_x$ MXene as an electrode for analytical electrochemistry using an outer-sphere redox probe. Building from Chapter 2, the study began with the BPE and evolved to the development of transparent electrodes.

3.1.4 Research objectives

1. To investigate the influence of material parameters (flake size and orientation) and electrode parameters (electrode thickness and size) of pristine $Ti_3C_2T_x$ on the electrochemical behaviour
2. examine the electrochemical performance of pristine $Ti_3C_2T_x$ electrodes under bending conditions.
3. To develop transparent pristine $Ti_3C_2T_x$ electrodes and investigate its impact on electrochemical performance.

3.2 Materials and Methods

3.2.1 Materials

- Pristine $Ti_3C_2T_x$ BPE and EPE (Section 2.2.5)
- Potassium chloride (KCl, 99.0 – 100.5%, ACS reagent, Sigma-Aldrich)
- Hexaammineruthenium (III) chloride ($(Ru(NH_3)_6Cl_3$, 98%, Sigma-Aldrich)
- Glass slides (Leika biosystems)
- Double-sided tape (3M, UK)
- Borosilicate glass rod (4 mm, Goodfellow Cambridge Ltd.)

3.2.2 Flake size reduction and physical characterisation

To reduce the size of $Ti_3C_2T_x$ flakes obtained from the synthesis protocol described in Section 2.2.2, probe sonication was selected based on concluding remarks of Section 2.3.3. Probe sonication (50% amplitude, 8:2 sec ON: OFF) was performed over 20 mins using an ice bath to avoid heating the MXene colloidal solutions. To estimate flake size dimensions and determine the polydispersity index, DLS was used with a 90-degree scattering optics spectrometer was utilised (Zetasizer Nano ZS, Malvern Panalytical, UK). The sample of interest was diluted until visually translucent and 1 mL of a MXene sample was pipetted into a

polystyrene cuvette. Three measurements were averaged for each sample. To confirm the flake size, scanning electron microscopy (Zeiss Supra 50VP scanning electron microscope) images were recorded of single flakes drop-casted on a porous anodic alumina membrane.

3.2.3 Preparation of transparent electrodes by spray-coating

To fabricate transparent electrodes, thin $Ti_3C_2T_x$ films were deposited onto a glass substrate. As-synthesised MXene colloidal solution (5 mg mL^{-1}) was spray-coated over 40 mins. To achieve electrodes with varying thicknesses, the lower section of the substrate (working electrode) was masked at specific time intervals (5, 10, 15, 20, and 25 minutes) during the deposition process. Meanwhile, the deposition of $Ti_3C_2T_x$ over the higher section of the substrates continued uninterrupted throughout the entire deposition period.

3.2.4 UV-vis spectroscopy measurements

To characterise the transparency of spray-coated electrodes, their UV-vis spectra were recorded using the Evolution 201 UV-vis spectrophotometer (Thermo Scientific, USA) scanning from 200-1000 nm. An uncoated glass substrate was utilised as the blank sample.

3.2.5 Electrochemical measurements

Electrochemical studies were performed using a CH 760E potentiostat (CH instruments, Texas). The three-electrode system used consisted of an Ag|AgCl (3 M KCl) reference electrode, a platinum wire auxiliary electrode, and pristine $Ti_3C_2T_x$ as the working electrode. Electrodes were characterised using 5 mM ruthenium hexamine in 1 M KCl using cyclic voltammetry. Cyclic voltammograms were recorded in potential windows between +200 and -700 mV at a scan rate of 5 or 20 mV s^{-1}. Measurements of the capacitance were measured in 1 M KCl with the same electrochemical parameters.

3.2.6 Flexibility test

To assess the electrochemical performance of pristine $Ti_3C_2T_x$ electrodes 3 conditions were considered. The first one was the control, which consisted of the pristine electrode in its natural form (straight) during measurement. To consider a bending state during measurement, the

electrode was wrapped around a 4 mm in diameter glass rod using a double-sided tape to immobilise the electrode (Condition A). Finally, the to consider them impact of bending cycles, the electrode was manually bent along its diameter 100 times 180 degrees (50 times inwards and 50 time outwards). Upon the electrode returning to its natural form after the bending cycles, the electrochemical measurement was recorded.

3.2.7 Electrochemical set up for transparent electrodes testing

The thicker section of the $Ti_3C_2T_x$ coating on a glass substrate was initially secured to the potentiostat using the alligator clip. Subsequently, the transparent/thinner $Ti_3C_2T_x$ sections of the coating were immersed into the electrolyte at a depth of approximately 5 mm. To guarantee exclusive contact of the electrolyte to the transparent segment of the coating, the alligator clip was fixed to the electrochemical beaker's wall before the electrochemical measurement.

3.2.7.1 *Determination of working electrode surface area*

The free software Image J (Wayne Rasband) developed in the Research Services Branch of the National Institute of Mental Health was utilised to determine the geometrical surface area of the transparent electrodes.

After conducting the electrochemical test, the electrode was extracted from the electrolyte, and photographs were captured alongside a ruler to establish scale. Subsequently, the photographs were uploaded to Image J to determine the electrode surface area. Through visual observation and manual determination, the area was precisely delineated. This was facilitated by the observable darkening of the electrode's colour, indicating its wet condition after exposure to the electrolyte.

3.2.8 Data analysis

The cyclic voltammograms were recorded using CHI 700 potentiostat. The anodic/cathodic peak potential and the current were obtained from the voltammograms using CHI 760E software. The geometric surface area (A, cm^2) of the film electrodes was calculated using the diameter or the length (Section 2.2.5.1) and thickness (Section 2.2.4.3) of the electrodes. All statistical analyses were performed using GraphPad Prism 7, a statistical software. The data underwent analysis using either a one-way ANOVA with Tukey's post hoc or an unpaired t-test for comparison of two data sets, with a significance level set at $p > 0.05$. Data was expressed as the mean plus or minus the standard error of the mean.

3.3 Results and Discussion

3.3.1 Impact of MXene flake size on electrode electroactivity

To investigate the impact of flake size on the electrochemical activity of pristine MXene, BPEs containing different flake sizes were fabricated as described in Section 2.3.4. The starting flake size distributions were measured via DLS and are shown in Figure 3.1a (methods detailed in Section 2.2.3.1), where the as-synthesised $Ti_3C_2T_x$ colloidal solution is referred to as “large flakes” (L-flakes) with an average hydrodynamic diameter of 1750 nm ± 65 nm and a PDI of 0.542. The flake size is typically inherited from the precursor Ti_3AlC_2 phase crystal size and the high polydispersity is attributed to the synthesis conditions whereby flakes are broken into smaller sizes (232). Probe sonication reduced the flake (S-flakes) as shown in their DLS distribution (Figure 3.4a) to an average size of 270 nm ± 2 nm with a PDI of 0.219 (methods detailed in Section 2.2.3.3) The inset of Figure 3.1a shows SEM images of the flakes deposited on a porous alumina substrate, clearly illustrating the difference in size between L- and S-flakes (methods detailed in Section 2.2.5.2).

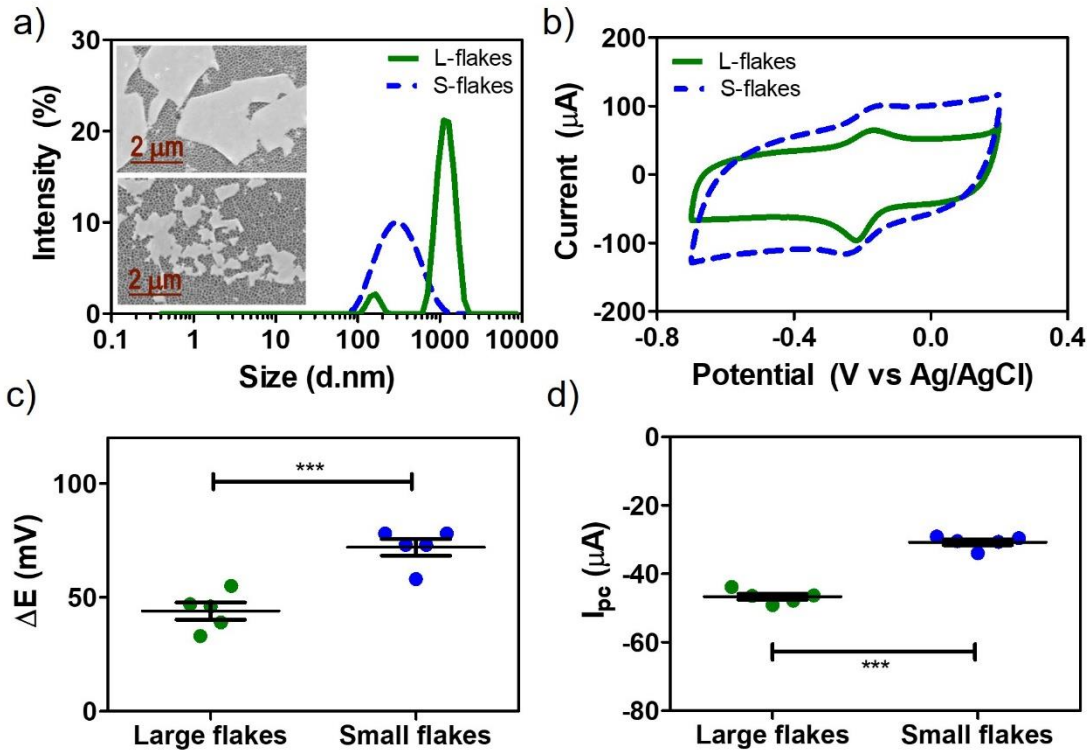

Figure 3.1. Effect of $Ti_3C_2T_x$ flake size on electrochemical behaviour of electrodes. a) Size distribution of as-synthesised (L-flakes, d=1750 nm) and probe-sonicated (S-flakes, d=270 nm) MXene colloidal solutions. Inset: Scanning electron microscopy images of large (top) and small (bottom) flakes of colloidal solution. b) Cyclic voltammograms of $Ti_3C_2T_x$ pristine electrodes fabricated with MXene colloids with large (L-) and small (S-) flakes in 5 mM ruthenium hexamine and 1 M KCl at a scan rate of 5 mV s^{-1}. c) Peak separation potential (ΔE, mV, mean ± standard error, $p<0.001$, n=5) and (d) reduction peak current (I_{pc}, µA, n=5, mean ± standard error of the mean, $p<0.0001$, unpaired t-test with Turkey's comparison) of L- and S-flake electrodes. Reprinted with permission from (299). Copyright 2024, American Chemical Society.

L- and S-flake electrodes were investigated using the outer sphere redox probe, and ruthenium hexamine using cyclic voltammetry (Figure 3.1b). The combination of a capacitive window with the faradaic peaks observed for ruthenium hexamine shows the pseudocapacitive behaviour of pristine $Ti_3C_2T_x$ electrodes(196). The S-flake electrode cyclic voltammogram shows a wider capacitive box which is likely due to greater ion diffusion as previously reported for small $Ti_3C_2T_x$ flakes (179). A slanted voltammogram for the S-flake electrodes was observed which combined with the significant increase in the difference between the cathodic and anodic peak potentials (ΔE) in S-flake electrodes when compared to L-flake electrodes ($p<0.0001$, n=5, Figure 3.1c), suggests higher resistivity for S-flake electrodes (233). The small flakes within the S-flake electrodes likely cause an increase in flake-to-flake contact resistance as previously reported (179) The cathodic current peak for L-flake electrodes was significantly higher than that and S-flake electrodes ($p<0.001$, n=5, Figure 3.1d) dropping from -46.7 μA to -30.7 μA. The smaller peak current observed for the S-flake electrode is likely due to the increase in capacitance obscuring the faradaic current and making its determination less accurate. In summary, L-flake electrodes showing a higher peak current are more sensitive due to using outer-sphere redox probes in addition to their better kinetics.

3.3.2 Impact of geometrical size and thickness of the electrode

Figure 3.2a shows cyclic voltammograms of BPEs with varying thicknesses (2, 4, and 8 μm) developed with the L-flake colloidal solution. There was a significant increase in ΔE (63 ± 3 mV for 2 μm, 76 ± 8 mV for 4 μm, and 88 ± 6 mV for 8 μm; $p<0.05$, n=6) with increased electrode thickness. This suggests an increase in resistivity and slower kinetics of the MXene film with increased thickness. Moreover, from the cyclic voltammograms of ruthenium hexamine, the capacitive box increased with increasing thickness, but no noticeable difference was observed in the faradaic current (Figure 3.2a). The faradaic current was then divided by the capacitive current to understand the impact of electrode thickness on the Faradaic signal. Figure 3.2b shows that with increased electrode thickness, the ratio of faradaic-to-capacitive

current decreased. This is most likely due to the increased thickness of the electrode providing more pathways for positively charged potassium ions from the electrolyte to penetrate the electrode structure and occupy electroactive surface sites of MXene flakes within the electrode, thus enhancing the capacitive current, while the redox probe only accesses the electrode surface.

Figure 3.2c shows voltammograms of electrodes made with varying diameters (2, 3, and 4 mm) with constant thickness (4 μm). There was no significant difference in ΔE (59.2 ± 4 mV for 2 mm, 56.2 ± 8 mV for 3 mm, and 63 ± 4 mV for 4 mm) with increased electrode diameter when performing a one-way ANOVA analysis. Furthermore, Figure 3.2d shows that the ratio of faradaic-to-capacitive current increases with an increase in surface area. This most likely is due to increased surface roughness when increasing the geometrical surface area of the electrode. MXene electrochemical sensors of any diameter and with minimal thickness would provide the greatest faradaic-to-capacitive current ratio.

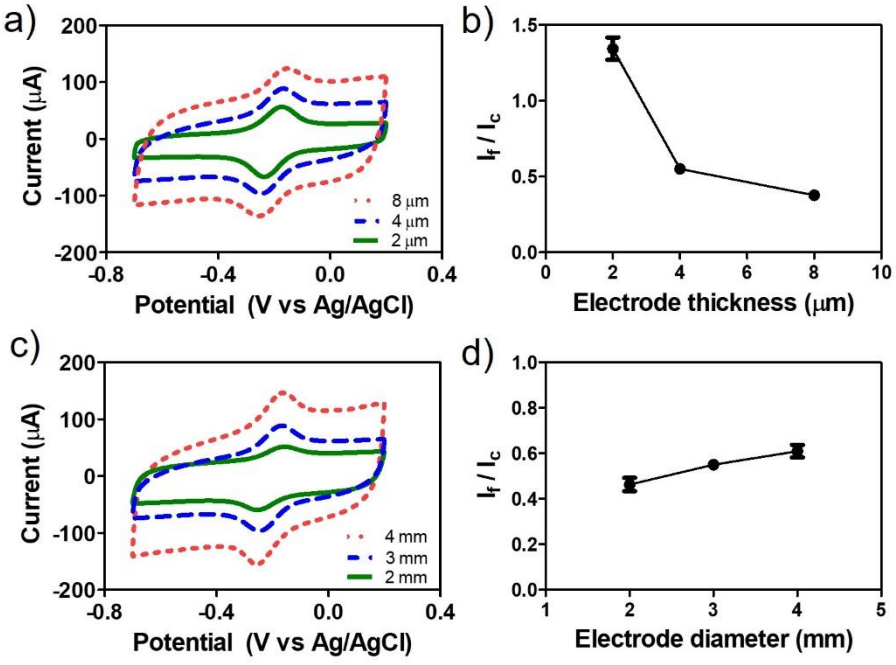

Figure 3.2 Effect of electrode thickness (μm, a-b) or diameter (mm, c-d) of pristine $Ti_3C_2T_x$ electrodes on their electrochemical behaviour. Cyclic voltammograms (a, c) of 5 mM ruthenium hexamine in 1 M KCl at 5 mV s^{-1}. Corresponding ratios of faradaic (I_f) to capacitive

(I_c) currents (b,d). (n=5, Mean ± standard error of the mean). Reprinted with permission from (299). Copyright 2024, American Chemical Society.

3.3.3 Impact of Flake Orientation

Due to the 2D structure of MXenes, the sites exposed at the electrode surface will vary by chemical structure. The outer layers of $Ti_3C_2T_x$ MXene comprise titanium atoms terminated by oxide, hydroxide, and fluoride groups on the basal plane, while little is known about the termination groups at the edge plane in which carbide layers are found between the titanium layers (Figure 3.3a). To investigate the differences in electroactivity of flake orientation, two electrode designs were prepared taking advantage of the organised structure (XRD, Section 2.3.1) of vacuum-filtered $Ti_3C_2T_x$ films. The SEM image of the top section of the film (Figure 3.3b) shows wrinkles of the overlapping layers while the cross-sectional SEM image of the film (Figure 3.3c) shows the stack of layers exposing the edges of the $Ti_3C_2T_x$ flakes. The inset of Figure 3.3b and c present optical images of the electrodes fabricated, predominantly exposing the basal plane of $Ti_3C_2T_x$ flakes (BPE) or the edge-plane of $Ti_3C_2T_x$ flakes (EPE). This further confirms the suitability of the electrode designs to investigate flake orientation.

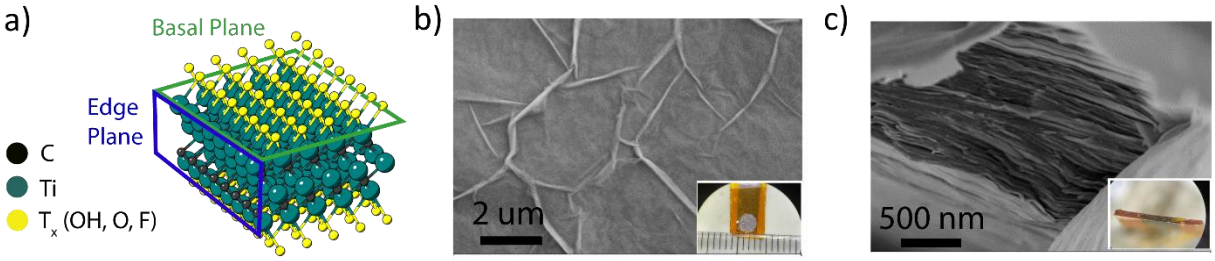

Figure 3.3. $Ti_3C_2T_x$ flake orientation within electrode. A) Schematic of $Ti_3C_2T_x$ structure highlighting its basal and edge planes. Scanning electron microscopy (SEM) micrographs of b) horizontal and c) cross-sectional plane of vacuum filtered films. The insets show optical images of their respective electrodes. Adapted with permission from (299). Copyright 2024, American Chemical Society.

Cyclic voltammograms of BPEs and EPEs were obtained in ruthenium hexamine (Figure 3.4d) and the current response was normalised by the electrode geometrical area. The normalised cathodic peak current of the EPE was significantly higher than that of the BPE ($p<0.0001$, $n=6$, Figure 3.6e). This is most likely due to two factors. First, the EPE being an ultra microband electrode, with thickness (or width) below 25 µm, resulted in a 2D diffusion system different from that of BPE, which is a macroelectrode(66). Second, the nonuniformity of the edges exposing variations in surface area between the $Ti_3C_2T_x$ flakes, as seen in the SEM image of Figure 3.4c, likely leads to a poor representation of the electroactive surface area, resulting in a larger experimental current observed for EPE. The ΔE of BPEs was significantly smaller ($p<0.0001$, $n=6$) than that of EPE (Figure 3.4f). This contradicts the initial assumption that transversal electron pathways in BPE would be less favourable compared to the electron pathway along the direction of $Ti_3C_2T_x$ layers in EPE. Hence, the variation in ΔE between the two electrode designs may be attributed to the double layer formation at the electrode surface. However, additional studies are necessary for a comprehensive understanding of these differences. While BPEs showed better kinetics than EPEs, the high current density of EPEs highlights their potential to be used as sensors with high sensitivity. Future work on single-flake analysis would contribute to the understanding of how exposed carbon layers at the edge of MXene flakes impact electrochemical properties.

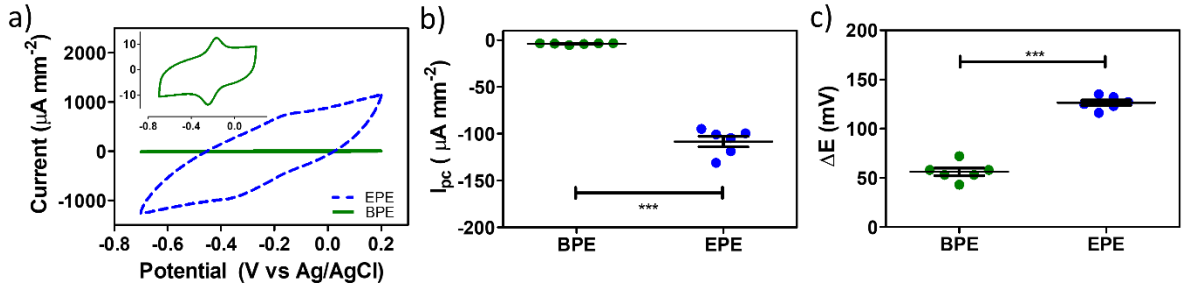

Figure 3.4 Effect of $Ti_3C_2T_x$ flake orientation on electrochemical behaviour of electrodes. a) Cyclic voltammograms of $Ti_3C_2T_x$ basal-plane electrodes (BPE) and edge-plane electrodes (EPE) in 5 mM ruthenium hexamine and 1 M KCl at a scan rate of 5 mV s^{-1}. B) Reduction peak

current (I_{pc}) and (c) peak separation potential (ΔE, mV) of BPEs and EPEs. (n=6, mean ± standard error of the mean, $p<0.0001$, unpaired t-test with Turkey's comparison)

3.3.4 Flexible $Ti_3C_2T_x$ Electrodes

To test the potential of pristine $Ti_3C_2T_x$ electrodes as flexible sensors, measurement under different conditions (described in detail in Section 3.2.6) were recorded in ruthenium hexamine. Figure 3.5b shows representative cyclic voltammograms of ruthenium hexamine under the two conditions and control electrode, where no particular differences were observed. There was no significant difference in the cathodic peak current (Figure 3.5c) and ΔE (Figure 3.5d) when the electrode was measured during flexible conditions when compared to control BPE electrodes. These findings are consistent with previous work in which micro-supercapacitors utilizing pristine MXene demonstrated remarkable flexibility, retaining 85% of their capacitance even after undergoing 1600 bends(234). These results highlight the ability of pristine MXene electrochemical sensors to provide reproducible responses even when flexed, making them well-suited for sensing applications requiring functional stability under motion (235,236).

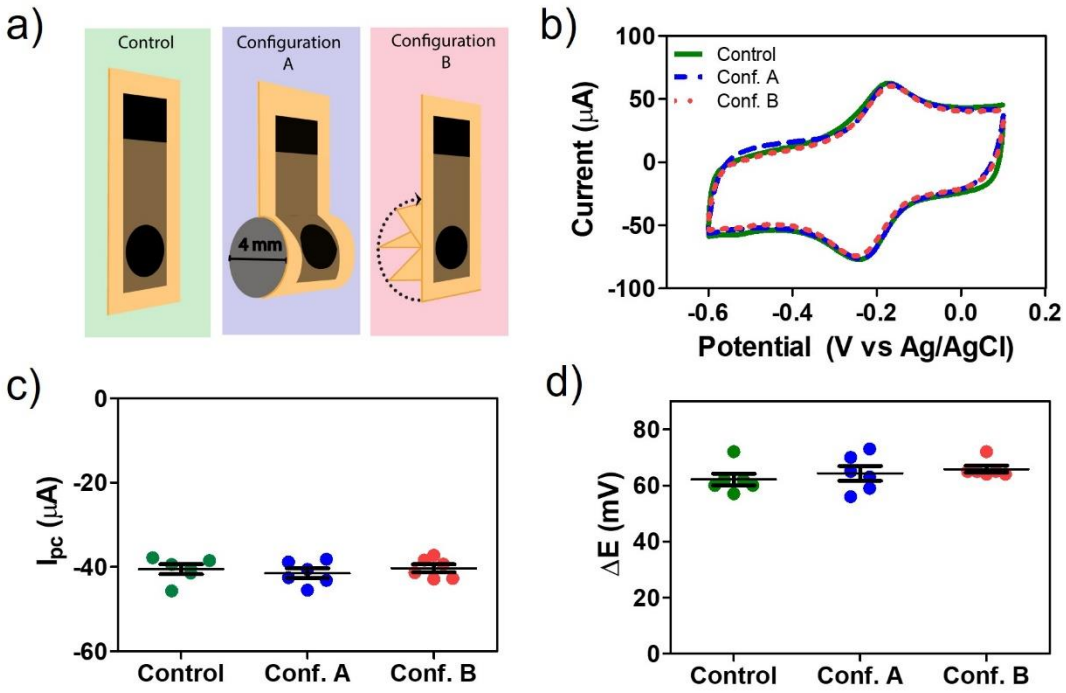

Figure 3.5. Impact of mechanical stress on electrochemical behaviour of $Ti_3C_2T_x$ electrodes. a) Schematic showing the difference between the control electrode, (Configuration A) the bent electrode during measurement, and (Configuration B) an outward bend out of 100 bends (50 inwards and 50 outwards) along the electrode diameter before measurement. b) Cyclic voltammograms of electrodes in 5 mM ruthenium hexamine in 1 M potassium chloride at 20 mV s^{-1}. c) Reduction peak current (I_{pc}, mA) and (d) redox peaks separation (mV) of cyclic voltammograms. (n=6, $p<0.001$, mean ± standard error of the mean, one-way ANOVA). Reprinted with permission from (299). Copyright 2024, American Chemical Society.

3.3.5 Transparent $Ti_3C_2T_x$ electrode

To explore the potential of $Ti_3C_2T_x$ as transparent electrochemical sensors, thin-film electrodes were developed by spray-coating MXene onto glass substrates. Increasing deposition times resulted in decreasing optical transparency (Figure 3.6a, section 3.2.3). The thickness of the top section of the electrodes was deliberately increased to ensure a good electrical connection. The transmittance spectra of the resulting electrodes indicate an

absorption peak at around 780 nm (Figure 3.6b), which is consistent with the plasmonic absorption peak characteristic of $Ti_3C_2T_x$ (237). The transmittance is also reduced at lower wavelengths due to inter-band transitions (238). Nonetheless, the visible transparency of each electrode was evaluated at the standard reference point of 550 nm, resulting in decreasing values of 97.9 % (a), 73.8 % (b), 57.4 % (c), 44.3 % (d), and 32.6 % (e) with increasing MXene deposition time. Based on the previously reported relationship between the absorbance and thickness of $Ti_3C_2T_x$ coatings, the spin-coated MXene electrodes were estimated to have thicknesses of 1.8 nm, 26.4 nm, 48.2 nm, 70.8 nm, and 97.6 nm, respectively, with increasing deposition time (239).

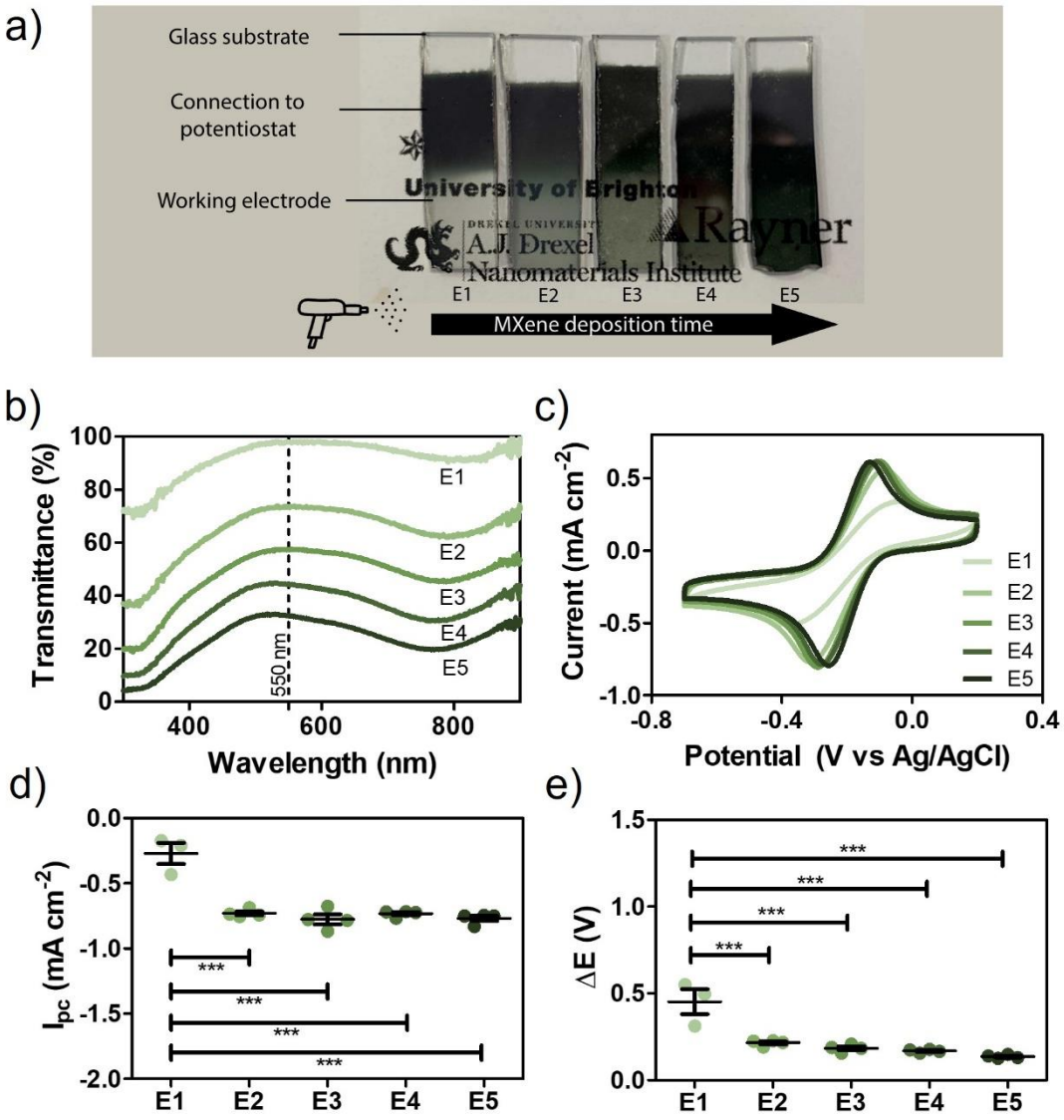

Figure 3.6. Impact of optical transmittance on electrochemical behaviour of $Ti_3C_2T_x$ electrodes. a) Spray-coated $Ti_3C_2T_x$ electrodes on top of paper-printed logos. b) Transmittance (%) spectra in the UV-visible region. c) Cyclic voltammogram of 5 mM ruthenium hexamine in 1 M potassium chloride at 20 mV s^{-1}. d) Reduction peak current (mA cm^{-2}) and peak separation potential (V) of corresponding Cyclic voltammograms (n=4, $p<0.001$, mean ± standard error, one-way ANOVA).

Figure 3.6c shows the cyclic voltammograms of ruthenium hexamine. For comparison between the impact of degrees of transparency of the electrodes in electrochemical behaviour, the current was normalised by the electrode surface area that was in contact with the electrolyte.

The redox peaks observed at around -0.2 V confirmed that $Ti_3C_2T_x$ can be used as a transparent electrode for the electrochemical reduction and oxidation of electroactive species, suggesting their use for transparent sensors. These cyclic voltammograms also demonstrate the ideal faradaic-to-capacitive current ratio previously discussed, in which faradaic current dominates the response. Figure 3.6d shows that the reduction peak current (mA cm^{-2}) of the transparent electrodes remained stable ($p<0.0001$, $n=4$) at a transmittance of 73.8% and below (electrodes E2-5). These findings suggest that comparable sensitivities can be attained at a relatively high transmittance of 73.8%. The decrease in electrochemical performance of the thinnest electrode studied (E1) is probably due to a non-uniform coverage considering the estimated thickness of 1.8 nm is close to monolayer coverage. A similar conclusion is obtained from Figure 3.6e in which the separation peak potential (V) is not significantly decreased beyond an electrode transmittance of 73.8%. There is a slight trend of decreasing ΔE with increasing thickness which is attributed to an increase in electron pathways within the coating. This work demonstrates the potential of $Ti_3C_2T_x$ to be utilised as transparent sensors without compromising electrode performance.

3.4 Conclusion

The findings of this chapter highlight key parameters to consider in the development and optimization of $Ti_3C_2T_x$ that can provide enhanced performance. For example, larger flakes and thin film electrochemical sensors provided the greatest faradaic signal on top of the capacitive current. Moreover, the initial difference with flake orientation encourages further investigation on basal vs. edge-plane. This work demonstrated that pristine $Ti_3C_2T_x$ films can be made into transparent and flexible electrochemical sensors while maintaining their excellent electrochemical activity. Results support the initial hypothesis that $Ti_3C_2T_x$ is a promising material for contact lens diagnosis due to its excellent stability under bending and transparent conditions. This research lays the foundation for continued investigation into pristine $Ti_3C_2T_x$ electrodes for advancing ophthalmic diagnostic technologies.

4 Assessment of pristine $Ti_3C_2T_x$ electrodes for detection of H_2O_2

4.1 Introduction

In the preceding chapter, the electrochemical characterisation of pristine $Ti_3C_2T_x$ electrodes highlighted their exceptional mechanical and optoelectronic properties which suggest suitability towards lens-based diagnostics. The comprehensive understanding gained from the exploration has paved the way for the current investigation, where the focus is shift towards the specific application of these electrodes in the electrochemical detection of H_2O_2 within the complex matrix of tear fluid. Having provided an insightful overview of tear fluid composition and various ophthalmic biomarkers, the attention in narrowed to the critical role of H_2O_2 in tear fluid.

4.1.1 Reactive oxygen species in the eye

Reactive oxygen species (ROS) are generated as natural by products of various biological processes including mitochondrial metabolism and can be found in different parts of the body. These ROS encompass free radicals such as superoxide anion (Ox-) and hydroxyl radical (HO) as well as nonradicals such as H_2O_2 (240). ROS are important species that participate in cellular signalling, immune response, and redox regulation. The production of ROS is counterbalanced by an antioxidant defence system based on enzymatic components including superoxide dismutase (DOS), peroxidases (GPXs) and ascorbic acid. When this antioxidant system fails to control ROS levels, oxidative stress occurs which can cause tremendous biological damage (240). Oxidative damage has been associated with chronic and degenerative diseases, with acute pathologies and aging (241).

Beyond the natural production of ROS in the eye, external stimuli also contribute to ROS production. UV-radiation is one of the main factors that generate exogenous ROS via photochemical reactions (242) However, ionizing radiation, cigarette smoke (243), and other pollutants also influence the imbalance of ROS in the eye (241). The excessive ROS production in the eye, has been associated with numerous interior eye pathologies in the conjunctiva, cornea, iris, retina and lens (244) While the pathogenesis of keratoconus, for example, is not

fully understood, studies have found elevated levels of ROS in the cornea (245,246). Additionally, the thinning and deformation of cornea is thought to be due several genetic and other environmental factors (247). An elevated ROS concentration in the aqueous humour has also been demonstrated to trigger several mechanism resulting in abnormal trabecular meshwork behaviour and increased intraocular pressure (248). Uveitis, dry eye, and conjunctiva disorder are other examples in which oxidative stress has played a major role in the development of the eye pathologies (244).

From the different ROS, the relevance of monitoring H_2O_2 in tear fluid has been highlighted in several publications. For example, to monitor the efficiency of nano-SOD1 in catalysing the dismutation of the superoxide radical, H_2O_2 was measured in the tear fluid (249). In this work, the nano-SOD1 served as a ROS scavenger to reduce the inflammation of inner vascular tract of the eye of rabbits with an immunogenic uveitis model. The determination of H_2O_2 concentration in tear fluid and corneal epithelial cells has also yielded insights into the impact of sleep deprivation on oxidative stress (250). The results showed that in sleep-deprived mice, H_2O_2 increased threefold by day 5 in tear fluid, while no significant changes were observed in corneal epithelial cells. These findings were further supported by the observed decrease in antioxidant capacity in tear fluid. Monitoring H_2O_2 has also served to determine glucose levels in the tear fluid as H_2O_2 is a by-product of the enzymatic oxidation of glucose (251). *In vitro* investigations have also emphasised the potential significance of monitoring H_2O_2 levels in tear fluid for 1) assessing cell treatments for the reduction of ROS species (252), 2) external mechanical and optical stimuli on ROS species (214,253) and 3) the impact of ROS species in the cell developmental process (254).

4.1.2 Electrochemical sensors for H_2O_2

H_2O_2 is an electroactive molecule capable of being electrochemically reduced (Equation 4.1) or oxidised (Equation 4.2) for its detection and quantification (255,256).

Numerous electrocatalytic materials and proteins have been used to develop electrochemical sensors for the detection of H_2O_2 (257). Protein-based biosensors typically have a biorecognition elements immobilised at the electrode surface, such as peroxidase, catalase and haemoglobin, that contain hemoproteins(258). Hemoproteins are a class of metalloproteins with iron-containing redox centres capable of oxidizing H_2O_2. The challenge in designing these sensors, is the electron transfer (ET) between the electrode and the active site, redox centre, that is deeply buried within the polypeptides. Moreover, the stability of these sensor is limited due to the strict storage requirements that some proteins like enzymes need. To overcome these challenges, direct ET has been achieved using materials such as iron-based metal hexacyanoferrate (Prussian blue), metals, metals oxides and nanomaterials (77,259). Their ability to electrochemically oxidise or reduce H_2O_2 lie in the high electrocatalytic activity of the material.

$$H_2O_2 + 2e^- \rightarrow 2OH^- \qquad \text{Equation 4.1(256)}$$

$$H_2O_2 \rightarrow O_2 + 2H^+ + 2e^- \qquad \text{Equation 4.2(255)}$$

In 2017, the first $Ti_3C_2T_x$-glassy carbon sensor for H_2O_2 was reported, showcasing the potential of $Ti_3C_2T_x$ -coated glassy carbon in reducing H_2O_2 (260). This initial work suggested a limit of detection (LOD) of 3.5 nM and a sensitivity of 596 mA cm^{-2} nM^{-1}. Since then, various composite materials utilizing $Ti_3C_2T_x$ have been developed to enhance the sensitivity of H_2O_2 sensors. For instance, S. Neampet et al. (261) utilised a mixture of platinum (Pt) nanoparticles (NPs), polyaniline (PANI), and $Ti_3C_2T_x$ drop-casted onto a screen-printed electrode to monitor H_2O_2[24]. The resulting composite exhibited a lower LOD of 1 μM compared to other counterparts, attributed to the increased surface area from the multilayer $Ti_3C_2T_x$, enhanced conductivity from PANI, and improved electron transfer facilitated by Pt NPs. Additionally, the incorporation of lactate oxidase allowed for the detection of lactate by quantifying the generated H_2O_2 during lactate oxidation. Enzyme-based sensors have also been developed for H_2O_2 detection, such as the flavin adenine dinucleotide/$Ti_3C_2T_x$ coating on glassy carbon. This composite enhanced redox transfer and electrocatalytic reduction of both H_2O_2 and FAD(262).

In addition to enzyme-based sensors, $Ti_3C_2T_x$ has also been employed in composites with other materials to expand the range of applications for H_2O_2 detection. For instance, F. Zhu et al (263). developed a composite sensor by electro-depositing Prussian Blue onto glassy carbon, followed by a layer of chitosan and, finally, the addition of $Ti_3C_2T_x$[26]. This sensor offered the advantage of performing amperometric measurements at a fixed potential of 0.0 V vs Ag|AgCl, effectively minimizing potential interference from other molecules. Furthermore, nanomaterials such as iron oxide (Fe_2O_3) nanoparticles (264), copper oxide (Cu_2O) nanoparticles (265), cobalt oxide (Co_3O_4) nanoparticles (266), molybdenum disulfide (MoS_2) (267), graphene (267), and silver (Ag) nanoparticles (268) have been effectively utilised in conjunction with $Ti_3C_2T_x$ to develop H_2O_2 sensors with improved performance characteristics.

The practical applicability of $Ti_3C_2T_x$-based sensors has been extensively validated through testing in diverse real samples, encompassing biological and food matrices. For instance, the lactate oxidase-based sensor effectively identified H_2O_2 in milk samples, presenting a valuable tool for quality control in the dairy industry (261). Likewise, the flavin adenine dinucleotide (FAD)-based sensor with $Ti_3C_2T_x$ coatings demonstrated its efficiency in detecting H_2O_2 in ovarian cell lines, showcasing potential applications in biomedical research and diagnostics (262).

Furthermore, the development of affordable electrochemical sensors targeting H_2O_2 remains a challenge, primarily influenced by the cost of electrode material and sensor fabrication. Addressing this, the substitution of noble metals like platinum by the utilization of nanomaterials composed of Earth-abundant elements emerges as a viable strategy. This rationale supports the reported cost-effectiveness and affordability of the $Ti_3C_2T_x$ /Co_4O_3-based electrochemical sensor (266). Its performance in quantifying H_2O_2 released by cancerous and normal cell lines, along with their overall reactive oxygen species (ROS) production was demonstrated using a portable potentiostat. The compactness and portability of such sensors is crucial for widespread availability in point-of-care settings, aligning with the objectives of predictive, preventive, and personalised medicine. These ongoing advancements and versatile

applications of $Ti_3C_2T_x$-based sensors for H_2O_2 detection continue to propel advances in analytical chemistry, fostering breakthroughs across numerous fields.

4.1.3 Gap in knowledge

While monitoring H_2O_2 in tears is recognised as important, there remains a significant gap in the development of lens-based diagnostics for H_2O_2. Despite the development of numerous H_2O_2 electrochemical sensors, their incorporation to lenses has not been explored. $Ti_3C_2T_x$ has been integrated into composite electrodes or chemically modified layers of glassy carbon electrodes for H_2O_2 quantification. However, the specific contribution of $Ti_3C_2T_x$ in sensing H_2O_2 remains unclear due to the presence of different electroactive components in the electrode. Despite $Ti_3C_2T_x$ use to enhance conductivity in electrochemical sensors, the lack of comprehensive studies on pristine $Ti_3C_2T_x$ has impeded the optimization of MXene electrodes.

Given the successful demonstration of $Ti_3C_2T_x$ as a redox-active material with terminated titanium outer layers, it is hypothesised that pristine $Ti_3C_2T_x$ electrodes is an attractive candidate for electrocatalytic activity towards H_2O_2. The relevance of investigating electrode parameters of $Ti_3C_2T_x$ pristine electrode, highlighted in Chapter 3, encourages a similar approach for the optimisation of pristine $Ti_3C_2T_x$. This study aims to showcase the utility of pristine $Ti_3C_2T_x$ electrodes for the electrochemical detection of H_2O_2 and optimize their performance in tear fluid.

4.1.4 Research objectives

1. To optimize pristine $Ti_3C_2T_x$ electrodes by adjusting material, electrode, and experimental electrochemical parameters for the detection of H_2O_2.
2. To investigate the impact of typical sterilization methods for biomedical devices on electrochemical performance.
3. To evaluate electrode performance in simulated tear fluid, considering potential interferent agents and electrode fouling.

4.2 Materials and Methods

4.2.1 Materials

- Hydrogen peroxide (H_2O_2, 30% w/w, contains stabilizer, Sigma-Aldrich)
- Sodium chloride (NaCl, 99+%, ACS reagent, Thermo Scientific Chemicals)
- Potassium chloride (KCl, 99.0 – 100.5%, ACS reagent)
- Sodium citrate ($Na_3C_6H_5O_7$, >99%, Sigma-Aldrich)
- D-Glucose ($C_6H_{12}O_6$, >99.5%, Sigma-Aldrich)
- Urea ($(NH_2)_2CO$, 99.0 – 100.5%, ACS reagent, Sigma-Aldrich)
- Calcium chloride ($CaCl_2$, 93%, Thermo Scientific Chemicals)
- Sodium carbonate (Na_2CO_3, 99.95%, Thermo Scientific Chemicals)
- Potassium hydrogen carbonate ($KHCO_3$, >99.5%, Merck)
- Sodium phosphate dibasic (Na_2HPO_4, 98+%, Thermo Scientific Chemicals)
- Potassium phosphate monobasic (KH_2PO_4, 99.5 – 100.5%, ACS reagent, Sigma-Aldrich)
- Hydrochloric acid (HCl, 37%, ACS reagent, Sigma-Aldrich)
- Sodium hydroxide (NaOH, Fischer Scientific Chemicals)
- Bovine serum albumin (BSA, >98%, pH 7, Sigma-Aldrich)

4.2.2 Electrolyte preparation

PBS with a concentration of 0.1 M was prepared by making up concentrations of 137 mM NaCl, 2.7 mM KCl, 8mM Na_2HPO_4 and 2 mM KH_2PO_4 DI water. The pH was then adjusted to 7.4 using NaOH (10 M).

Complex salt solution (CSS) was developed by making up concentrations of 90 mM NaCl, 16 mM KCl, 1.5 $Na_3C_6H_5O_7$, 0.2 mM $C_6H_{12}O_6$, 1.2 mM $(NH_2)_2CO$, 0.5 mM $CaCl_2$, 12 mM Na_2CO_3, 3 mM $KHCO_3$, 24 mM Na_2HPO_4 in DI water. The pH was then adjusted to 7.4 using HCl (10 M).

Simulated tear fluid (STF) was prepared by using CSS to dilute BSA with a final protein concentration of 10 mg mL^{-1}.

4.2.3 Electrochemical measurements

Electrochemical measurements were recorded using a CHI1021 potentiostat at 100 mV s^{-1}. Cyclic voltammetry was performed at 100 mV s^{-1} or 20 mV s^{-1}. Amperometry was performed by applied a constant potential at -250, -450, -650, -850, -1050 or -1250 V vs Ag|AgCl.

4.2.4 Data analysis

Amperometry recordings were smoothed using the CHI software. Background currents were subtracted using Igor software. Capacitances were calculated as follows mF= 2 current/scan rate. One way-ANOVA or two-way ANOVA were the statistical studies performed and used as stated in the text. A p-value <0.05 was considered significant.

4.3 Results and Discussion

4.3.1 Potential window

Understanding the potential window in which pristine $Ti_3C_2T_x$ electrode does not oxidises nor reduces the electrolyte components is essential to conduct experiments. Phosphate buffer saline (PBS) solution was selected as it is a common electrolyte containing an osmolarity and salt concentration similar to that of biological fluids. Figure 4.1a shows a cyclic voltammogram of a pristine $Ti_3C_2T_x$ electrode cycled between 1 and -2 V (vs Ag|AgCl) at 100 mV s^{-1}. It can be observed that around -1.3 V, the current takes off which can be attributed to the reduction of water to hydrogen gas and hydroxide ions. This is also known as hydrogen evolution, which is the limiting border of the stable negative potential window. When the electrode is scanned positively, a small peak is first observed at around 0.15 V followed by a larger peak around 0.45 V. These two peaks are attributed to the opening of MXene layers conforming the electrode by the intercalation of ions. Additionally, it is at this range that the

irreversible oxidation of titanium from $Ti_3C_2T_x$ occurs. Right after these two peaks are observed, overpotential is observed. This attributed to the oxidation of water into oxygen, also known as oxygen evolution. Considering the relevance of retaining an unmodified electrode for current studies, the limit of the positive potential window is determined by the irreversible oxidation of titanium rather than by the overpotential of the oxygen evolution at + 0.2 V.

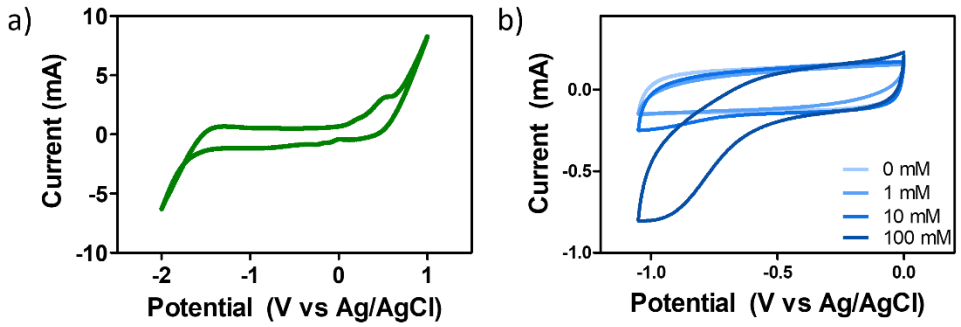

Figure 4.1. Cyclic voltammograms of $Ti_3C_2T_x$ electrodes in 0.1M PBS with and without H_2O_2. a) Determination of negative stable potential window of pristine $Ti_3C_2T_x$ electrode in 0.1 M PBS at 100 mV s^{-1}. b) Cyclic voltammograms of pristine $Ti_3C_2T_x$ electrode in 0.1 M PBS with additions of H_2O_2 (0 – 100 mM).

Having determined the potential window of pristine $Ti_3C_2T_x$ electrode in this electrochemical configuration, cyclic voltammetry was selected as the technique to visualize the oxidation or reduction of H_2O_2 at the electrode surface. As shown in Figure 4.1b, the addition of different concentrations (0.1, 1, 10 and 100 mM) of H_2O_2 alters the cyclic voltammogram. No particular peaks are observed for reduction nor oxidation of H_2O_2. However, at around -0.5 V, an increase in current occurs with the increase of H_2O_2 concentration. This suggests that faradaic current raises from the reduction of H_2O_2 at the electrode surface. Moving forward, amperometry is selected as the electrochemical technique to investigate the reduction of H_2O_2 considering its ability to discriminate faradaic currents from capacitive currents. The initial constant applied potential, to investigate material parameters, was selected to be -0.65 V vs Ag|AgCl as it is at this potential that an increase in current is identified with 1 mM addition of H_2O_2.

4.3.2 Material and electrode parameters

Considering the impact of flake size and electrode thickness observed on the reduction of ruthenium hexamine in Chapter 3, a similar study is performed for H_2O_2. It is important to note, that these two molecules follow different electron transfer mechanisms and therefore it is not possible to extrapolate previous conclusions. Electrodes of 4 and 8 μm thickness were used to quantify the amperometric response of pristine $Ti_3C_2T_x$ electrode to an in-situ addition of 1 mM H_2O_2 at -0.65 V vs Ag|AgCl in 0.1 M PBS. There was no significant difference between electrode thickness for large flake electrodes demonstrating that the current response to H_2O_2 is independent of thickness (Figure 4.2a). The performance of electrodes composed of small (260 nm) and large (>1 μM) flakes with a thickness of 4 μm was also compared. As shown in Figure 4.2b, an increase in current response is observed for the electrode composed of small flakes. shows no significant different in current response to the addition of 1 mM of H_2O_2. This suggests that electrodes with smaller flakes can achieve higher sensitivities towards H_2O_2. Further investigation on the mechanism of detection may unravel more understanding on the impact of edge effects on the reduction of H_2O_2.

The flake size-dependent electrochemical behaviour of $Ti_3C_2T_x$ electrodes towards H_2O_2 and ruthenium hexamine may be attributed to differences in molecular size and electron transfer mechanisms between these molecules and the electrode. The smaller size of H_2O_2 is likely to access a higher surface area, given the 3D structure of the electrodes. Consequently, an increase in surface roughness resulting from a decrease in flake size is expected to provide a larger surface area for H_2O_2 reduction. In contrast, ruthenium hexamine, being a larger molecule and following outer-sphere electron transfer, may not be impacted by a slight increase in surface area due with a decrease in $Ti_3C_2T_x$ flake size. Instead, the increase in resistance and capacitance resulting from smaller flake sizes, as discussed in Section 3.3.1 (Figure 3.1), may overshadow the current response. Additionally, it is important to note that two different electrochemical techniques, amperometry and voltammetry, were employed for reduction of H_2O_2 and ruthenium hexamine, respectively, therefore preventing a direct comparison.

However, this underscores the significance of systematically characterizing material parameters for the detection of different analytes of interest.

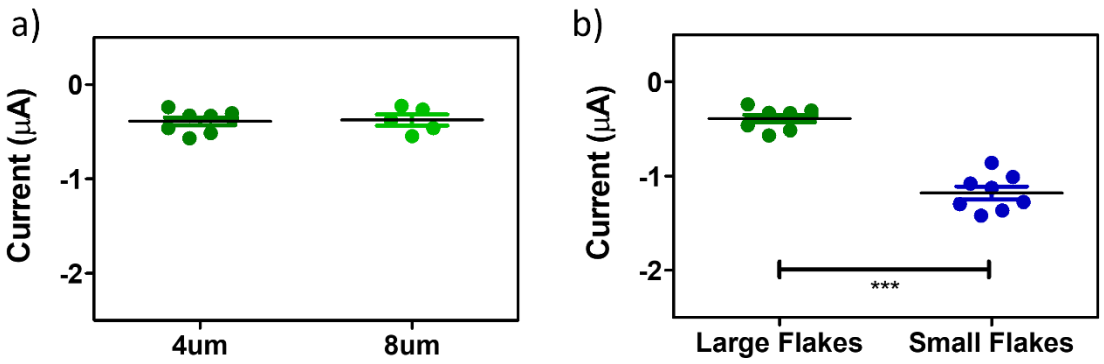

Figure 4.2. Impact of material parameters in electrochemical response of $Ti_3C_2T_x$ to 1 mM of H_2O_2. a) Current response to 1 mM of H_2O_2 at -650 mV vs Ag|AgCl of electrodes of (a) 4 μm or 8 μm thickness and b) electrode made of large or small flakes. (n=6, $p<0.0001$, data shown as mean ± standard error of the mean, unpaired t-test)

Figure 4.3 depicts the optical images illustrating discernible distinctions in vacuum-filtered films composed of flakes with different sizes. Specifically, films comprised of large flakes (Figure 4.3a) exhibit a uniform appearance, while films composed of small flakes (Figure 4.3b) exhibit noticeable macroscale cracks on the surface. Consequently, extra caution was necessary when handling small-flake films during the electrode fabrication process to prevent their breakage. It is well-known that large flakes tend to produce mechanically more stable films compared to small flakes.

Considering the requirement of developing highly mechanically stable electrodes capable of bending without breaking, the study proceeded with large flakes as the primary focus. However, it was also acknowledged that the design of the electrochemical sensor may necessitate higher sensitivity. To address this consideration, a mixture of large and small flakes could be contemplated, as it could offer the benefits of a highly stable electrode derived from large flakes, along with the larger sensitivity towards H_2O_2 provided by small flakes. Small flakes

are also considered in the following chapter in which a different substrate is considered for the development of this electrode.

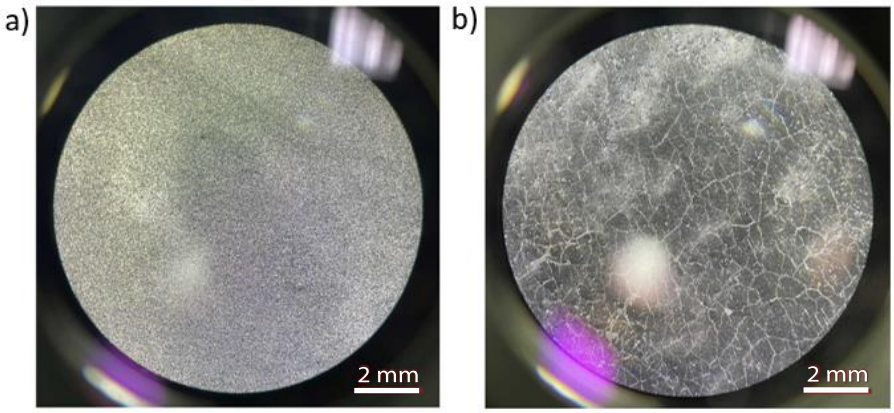

Figure 4.3. Images using an optical microscopy of vacuum-filtered films of (a) large and (b) small $Ti_3C_2T_x$ flakes.

4.3.3 Electrochemical parameters

To optimise the electrochemical parameters of the experiment, amperometric curves were obtained at various applied voltages (-250, -450, -650, -850, -1050, and -1250 mV), as shown in Figure 4.4a. Notably, a negative jump in current was observed every 50 seconds, starting at t=100 seconds, corresponding to the increase in H_2O_2 concentration from 0 to 1 mM. Figure 4.4b displays the corresponding calibration curves (n=5).

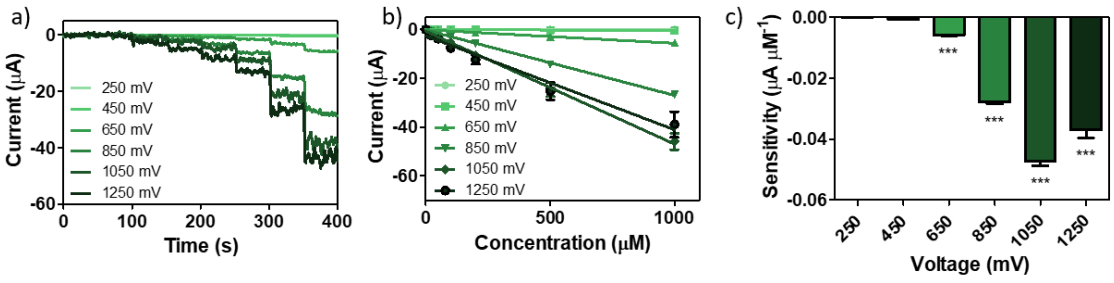

Figure 4.4. Calibration curves of H_2O_2 at different applied potential using $Ti_3C_2T_x$ electrodes. a) Amperometric responses to changes in H_2O_2 concentration (20, 50, 100, 200, 500 1000 μM) every 50 s starting at t=100 s at different applied potentials (250 – 1250 mV). b) Corresponding calibration curves of H_2O_2 at different applied potentials. c) Sensitivity (μA $μM^{-1}$) towards H_2O_2 at different applied potentials. (n=5, $p<0.001$, data shown as mean ± SD, one-way ANOVA with Tukey's post-test)

Linear regression analysis was performed for each calibration curve, revealing strong correlations for all curves, with coefficients of determination (R^2) as shown in Table 4.1. The slopes of the linear regressions were determine and are indicative of the sensitivity of the electrode towards the reduction of H_2O_2 (Table 4.1). These slopes were expressed in units of μA $μM^{-1}$, signifying the sensitivity of the electrode (Figure 4.4c). Given that the highest sensitivity was achieved at a voltage of 1050 mV, further experiments were conducted using this optimised parameter.

Table 4.1. Impact of applied potential in the sensitivity of pristine $Ti_3C_2T_x$ towards the electrochemical reduction of H_2O_2.

Applied potential (mV)	**Sensitivity (x10^4 μA $μM^{-1}$)**	**R^2**
-250	1.377	0.907
-450	6.612	0.905
-650	59.76	0.980
-850	279.8	0.995
-1050	473.7	0.962
-1250	371.4	0.850

4.3.4 Impact of sterilization

The next aim was to investigate the impact of common sterilization methods for biomedical devices on the electrochemical performance of the pristine $Ti_3C_2T_x$ sensor.

Considering the impending cytocompatibility assessment of pristine $Ti_3C_2T_x$ electrodes in the following chapter (Chapter 5), the impact of UV-sterilization, a standard sterilization method in cell culture, was investigated. The effect of UV-sterilization on the electrochemical detection of H_2O_2 was examined by subjecting the fabricated electrodes to a 1-hour UV-sterilization process. A comparative analysis was then conducted between the UV-sterilised electrodes and a control group consisting of non-sterilised electrodes. The amperometric response to an *in-situ* addition of 500 µM of H_2O_2 with an applied voltage of -1050 mV (vs Ag|AgCl) was recorded (Figure 4.5a). Evaluation of the results, as depicted in Figure 4.5b, revealed no statistically significant difference between the UV-sterilised group and the control group. In accordance with literature, exposure of 1 hr to UV radiation is not enough time to degrade $Ti_3C_2T_x$. This was demonstrated in a study where the photocatalytic degradation of $Ti_3C_2T_x$ was induced only after 3 hours of UV radiation (269). Moreover, it is likely that the potential degradation of pristine $Ti_3C_2T_x$ electrodes, is further decrease from that reported in literature considering that in this work, $Ti_3C_2T_x$ is in its dried state, as opposed to being suspended in water. The dissolve oxygen in $Ti_3C_2T_x$ colloids tend to accelerate $Ti_3C_2T_x$ oxidation (270).

In the context of exploring the potential application of pristine $Ti_3C_2T_x$ in contact lens diagnostics, the impact of autoclave sterilization, a standard procedure for contact lenses, was assessed (271). The electrodes were subjected to autoclaving for a duration of 20 minutes. Similarly, the autoclaved electrodes were compared with the control group of non-sterilised electrodes in terms of their amperometric response to H_2O_2 detection. Amperometric response was measured at a constant applied potential of -1050 mV (vs Ag|AgCl), with an in-situ addition of H_2O_2 (500 µM) at t=50 seconds (Figure 4.5ac). The resulting data, depicted in Figure 4.5d, indicated no significant disparity between the autoclaved group and the control group. The lack of impact on the electrochemical properties of $Ti_3C_2T_x$ MXene aligns with previous work (272). A study investigating the impact of several sterilization methods demonstrated no impact on electrical conductivity, electrochemical impedance nor surface morphology after autoclave sterilization of $Ti_3C_2T_x$ electrodes (272). Moreover, their work

suggests that the pre-intercalated water molecules from environmental humidity were likely evaporated during autoclave sterilization. Finally, the successful removal of pathogens of contaminated $Ti_3C_2T_x$ samples with Escherichia coli was confirmed through bacterial count. These parallel outcomes from the autoclave study reinforce the conclusion that autoclave sterilization, like UV-sterilization, does not compromise the electrochemical performance of the $Ti_3C_2T_x$ sensor, affirming its suitability for biomedical device sterilization in various industries.

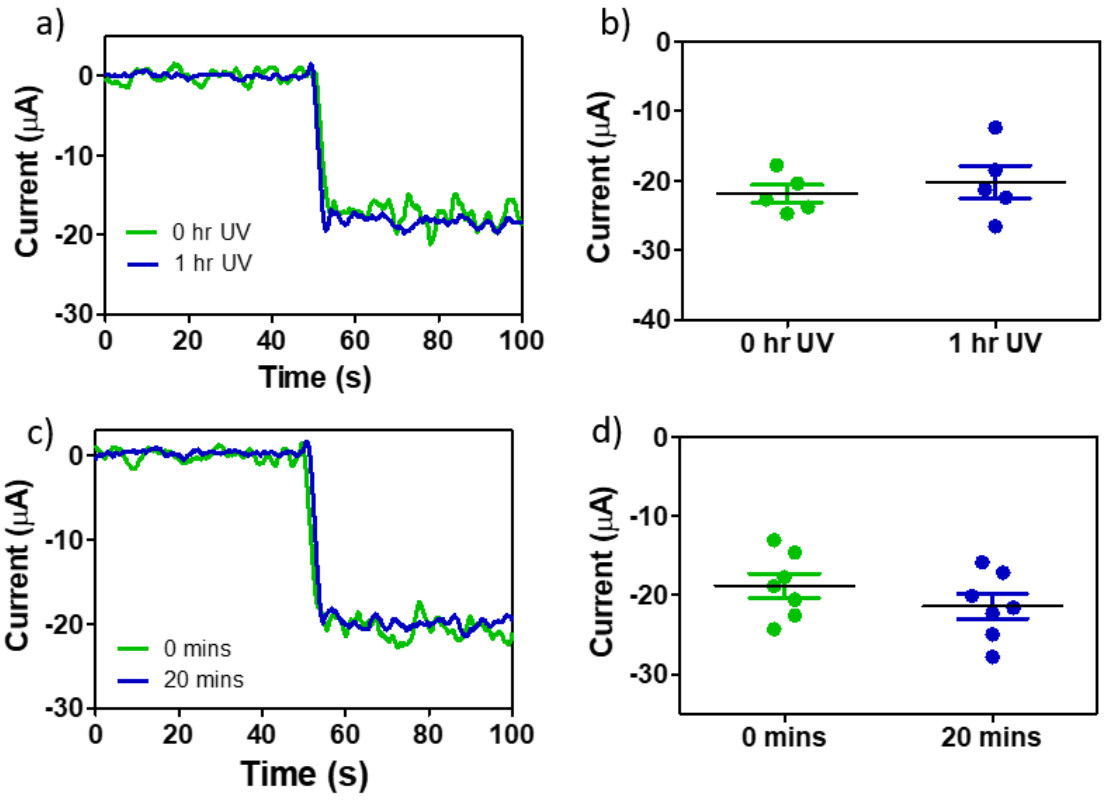

Figure 4.5. Impact of typical sterilization methods on the electrochemical performance of pristine $Ti_3C_2T_x$ as a sensor for H_2O_2 a) Amperometric response to addition to H_2O_2 (500 μM) at t=100 seconds in 0.1 M PBS between UV-sterilised (1 hr) and non-sterilised (0 hrs) electrodes. Applied voltage of 1.05 V (vs Ag|AgCl). b) Corresponding current response to 500 μM H_2O_2. c) Amperometric responses of autoclaved (20 mins) and non-autoclaved (0 mins) $Ti_3C_2T_x$ electrodes to an addition of 500 μM H_2O_2 at time 50s. d) Comparison between current response. (n=6, $p<0.0001$, data shown as mean ± standard error of the mean, unpaired t-test)

4.3.5 Electrode Fouling

Investigating electrode fouling during electrochemical measurements is very important in order to ensure accurate and reliable results. Electrode fouling can arise from various factors, including the presence of proteins in the electrolyte, which can interfere with the signal and compromise the detection of target analytes. This becomes particularly significant when studying electrochemical processes in physiological environments, such as the eye, where tear fluid acts as the electrolyte.

In this study, the effects of electrode fouling and protein interference on the electrochemical detection of H_2O_2 were explored. The focus was on assessing the capacitance and faradaic currents as well as signal stability of pristine $Ti_3C_2T_x$ electrodes in different electrolytes, including 0.1 M phosphate-buffered saline (PBS), simulated tear fluid (STF) with and without (complex salt solution (CSS)) protein. Figure 4.6a illustrates representative cyclic voltammograms of the electrodes in 0.1 M phosphate-buffered saline (PBS), complex salt solution (CSS), and simulated tear fluid (STF). A subtle decrease in the capacitive box can be observed for the electrodes immersed in CSS and STF compared to those in PBS. This observation was further supported by Figure 4.6b, where a significant reduction in capacitance (measured in millifarads, mF) was evident for CSS ($p< 0.05$) and STF ($p<0.05$). Remarkably, no notable disparity in capacitance was observed between CSS and STF, suggesting that the presence of protein (10 mg/mL) neither interferes with nor contributes to the intercalation of ions between the layers of the MXene electrodes.

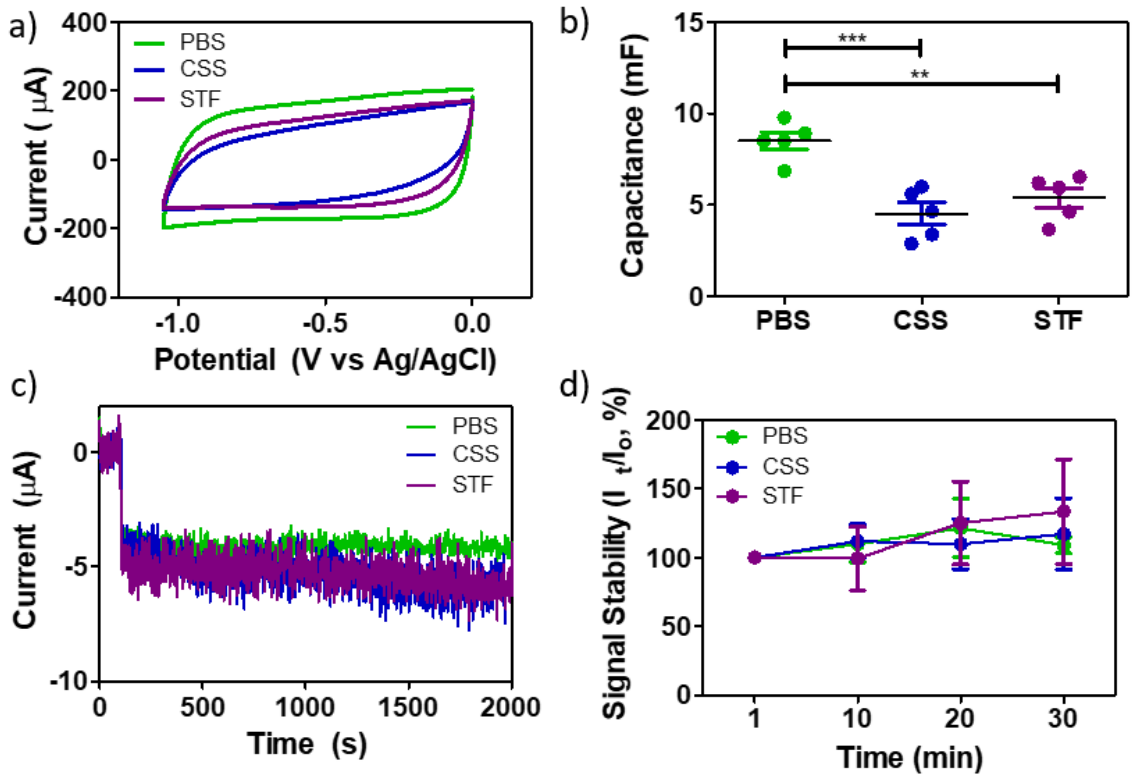

Figure 4.6. Electrochemical fouling of $Ti_3C_2T_x$ electrodes in simulated tear fluid. a) Cyclic voltammograms of pristine $Ti_3C_2T_x$ electrodes in 0.1 M phosphate buffer saline (PBS), complex salt solution (CSS) and CSS containing BSA (10 mg mL) named simulated tear fluid (STF). b) Capacitance (mF) at -525 mV (vs Ag|AgCl) (n=5, $p<0.05$, data shown as mean ± SD, one-way ANOVA). c) Amperometric response to 500 μM of H_2O_2 at t=100 s (-1050 mV). d) Signal stability (%) from initial response (t=1 min) to H_2O_2 at 10, 20 and 30 mins. (n=5, data shown as mean ± SD, two-way ANOVA)

A similar investigation was conducted to examine the impact of electrolyte composition, with or without proteins, on the detection of H_2O_2. The amperometric response to an in-situ addition of H_2O_2 (500 μM) was compared among the three electrolytes. The faradaic response, resulting from the reduction of H_2O_2, was recorded over a 30-minute duration, as displayed in Figure 4.6c. The current values were normalised based on the initial response and analysed at 10-minute intervals (Figure 4.6d). Notably, no significant difference ($p<0.05$) was observed between electrolytes, suggesting the absence of electrode fouling during the measurements

despite the presence of proteins. However, an increase in signal response ($p=0.02$) after the 30-minute period for all three electrolytes was observed. This is likely due to a better penetration of the electrolyte through the electrode. Therefore, if H_2O_2 measurements were to be recorded over time, a fitting curve to take into account the swelling of the electrode over time would ensure an accurate reading of H_2O.

4.3.6 Electrode selectivity

Considering the complexity of tear fluid, which comprises various ions, proteins, and biomolecules, it is crucial to assess the selectivity of the pristine $Ti_3C_2T_x$ electrode in electrochemical detection of H_2O_2 by examining potential interferent agents. To evaluate selectivity, dopamine, glucose, potassium chloride (KCl), ascorbic acid (AA), and urea were added at the same concentration as H_2O_2 (500 μM) during a constant potential of -1050 mV vs Ag|AgCl.

Figure 4.7a demonstrates that only the addition of H_2O_2 at t = 50 s and t = 225 s resulted in an increase in faradaic current. Statistical analysis revealed significant differences ($p < 0.0001$) between the addition of 500 μM of H_2O_2 and the addition of 500 μM of any other molecule (Figure 4.7b). Conversely, no significant differences were observed between the addition of any of the other molecules, indicating that none of the analytes were reduced at this potential. This outcome is expected since most of these molecules can only be oxidised at positive potentials. Consequently, none of these molecules present a challenge for the selective detection of H_2O_2. By assessing the response of the pristine $Ti_3C_2T_x$ electrode to various interferent agents, it is evident that the electrode exhibits excellent selectivity for H_2O_2 detection. This selectivity is essential in accurately measuring H_2O_2 levels in tear fluid, as interferent molecules commonly present in tear fluid do not interfere with the electrochemical detection of H_2O_2 using the $Ti_3C_2T_x$ electrode.

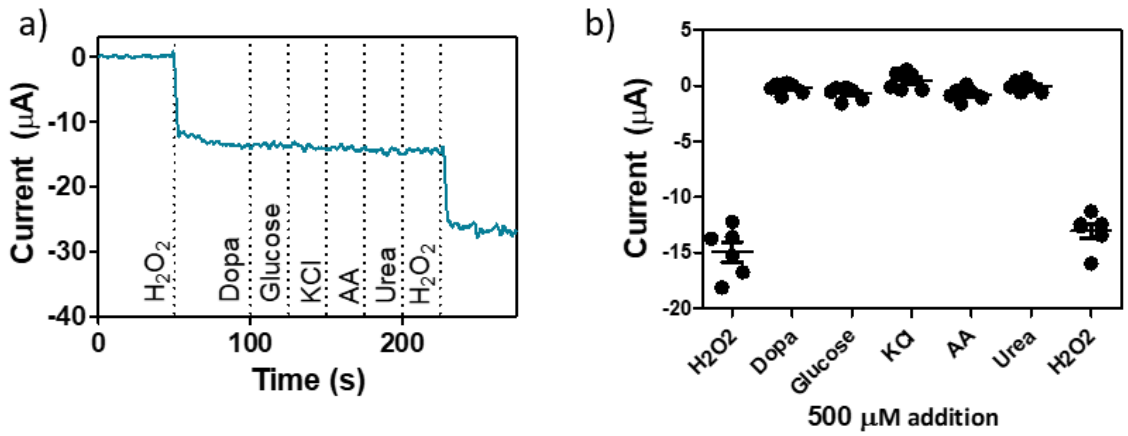

Figure 4.7. Selectivity of $Ti_3C_2T_x$ electrodes towards the electrochemical detection of H_2O_2. a) Amperometric responses to 500 μM additions to (50 s) hydrogen peroxide (H_2O_2), (100 s) dopamine, (125 s) glucose, (150 s) potassium chloride (KCl), (175 s) ascorbic acid (AA), (200 s) urea, and (225 s) H_2O_2. Constant applied potential -1050 vs Ag|AgCl. b) Quantified current to the additions to different analytes. (n=6, $p<0.05$, data shown as mean ± SD, one-way ANOVA)

4.3.7 Stability of electrode in stimulated tear fluid

Finally, the effect of electrode incubation in simulated tear fluid for 24 hours in its electrochemical performance towards H_2O_2 detection was investigated. As shown in Figure 4.8a, the section of the working electrode was submerged into simulated tear fluid containing 10 mg mL^{-1} of BSA in an Eppendorf tube. Considering the electrode would be reutilised, to avoid the impact of any potential puncturing from the alligator clip on the second measurement, aluminium foil was utilised to protect the electrode. The aluminium foil covering the area in which the potentiostat is clipped, can be observed in Figure 5.8a. Amperometry responses to 500 μM of H_2O_2 in simulated tear fluid were recorded at -1050 mV vs Ag|AgCl. Representative traces of measurements of the same electrode before (t=0 hrs) and after (t=24 hrs) are shown in Figure 5.8b. The current responses were quantified and plotted for comparison (Figure 5.8c). A paired t-test statistical analysis showed no significant differences on the current responses

before and after incubation. These results suggest the electrode stability without protein fouling the electrode. Moreover, this highlights the potential of pristine $Ti_3C_2T_x$ electrode for electrochemical measurements in biological fluids such as tear fluid which contains one of the highest concentrations of protein in the body.

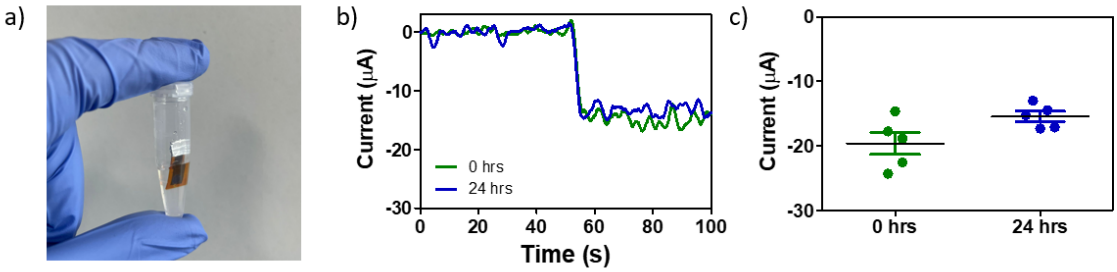

Figure 4.8. $Ti_3C_2T_x$ electrode stability over 24 hrs. a) Optical photograph of working electrode being incubated in simulated tear fluid for 24 hrs in an Eppendorf tube. b) Amperometric responses to 500 μM additions to (50 s) H_2O_2 in simulated tear fluid at -1050 V vs Ag|AgCl at t = 0 hrs and at t = 24 hrs. c) Quantified current response to the additions of H_2O_2. (n=5, $p<0.05$, data shown as mean ± standard error of the mean, paired t-test).

4.4 Conclusion

In this chapter, a pristine $Ti_3C_2T_x$ electrode was for the first time used to electrochemically detect H_2O_2. The potential window in 0.1 M PBS was determined, revealing the sensor's operating window in biologically relevant ion concentrations. The experiment results demonstrate the capability to use pristine $Ti_3C_2T_x$ without any other electroactive material for the detection of H_2O_2. The current response to additions of H_2O_2 was independent of thickness, suggesting that the sensor performance is not affected by this parameter. However, by reducing the flake size of the electrode, the sensitivity of the sensor could be improved. Unfortunately, electrodes made with large flake $Ti_3C_2T_x$ resulted in the most stable film, while small-flake electrodes crumble and needed more care when handling. For this reason, studies were performed in large-flake electrodes.

To improve the sensitivity, different applied voltages were tested using amperometry. An applied voltage of -1050 mV vs Ag|AgCl was found to achieve the highest sensitivity for H_2O_2 detection. At this specific potential, the sensor demonstrated excellent selectivity by not responding to additions of other analytes at the same concentration, confirming its specificity for H_2O_2. To assess the sensor performance for a real-life application in tear fluid, tests were carried out in simulated tear fluid containing biologically relevant concentrations of protein. Results revealed that the presence of protein did not interfere with the accurate detection of H_2O_2 which is crucial for the translation of this application. Additionally, its performance over a period of 30 minutes was demonstrated. Moreover, after a 24-hr incubation in simulated tear fluid, the sensor's response was successfully maintained. These results highlight the robustness and suitability of pristine $Ti_3C_2T_x$ electrode for the detection of H_2O_2 in tear fluid.

5 Incorporation and characterization of pristine $Ti_3C_2T_x$ electrode on a contact lens hydrogel

5.1 Introduction

Building on the findings presented in Chapter 4, where pristine $Ti_3C_2T_x$ demonstrated successful electrochemical detection of H_2O_2 in simulated tear fluid, the current chapter delves into a more extensive exploration. The focus now shifts towards investigating the feasibility of incorporating $Ti_3C_2T_x$ electrodes onto contact lenses, aiming for a comprehensive evaluation encompassing both electrochemical and biological aspects. While Chapter 4 addressed a critical knowledge gap concerning the potential of $Ti_3C_2T_x$ in detecting H_2O_2 in simulated tear fluid, further endeavours are essential to optimize the sensor for practical application in lens-based sensor diagnostics for the anterior eye. This chapter commences with a review of the development of transparent and flexible electrochemical sensors specifically designed for H_2O_2 detection.

5.1.1 Transparent and flexible electrochemical sensors for the detection of H_2O_2

A limited number of studies have reported the successful fabrication of transparent and flexible electrochemical sensors to detect H_2O_2 (214,220,273). However, none have been incorporated into a lens design., The first transparent and flexible electrochemical sensor for H_2O_2, developed in 2016[1]consisted of AgNW films formed by mixing cellulose ester (273). 67% transparency was achieved by heat treatment with an optimised resistivity of 13 ohm sq^{-1}. Mechanical stability was demonstrated through consistent resistance levels even after subjecting the sensor to 50 bending cycles. The robustness of the sensor was further evidenced by the absence of resistance changes during exposure to increased temperatures (>85°C) or a concentrated salt solution (NaCl, >2 M), showcasing its resilience to diverse environmental conditions. Finally, photolithography was employed to pattern the working electrodes for the electrocatalytic reduction of H_2O_2.

In 2021, a stretchable and transparent electrode was developed by electrodeposition of Au NPs onto vacuum-filtered CNTs previously transferred to a PDMS substrate (214). Similar to the

aforementioned work, the flexibility test confirmed good mechanical stability with slight changes in relative resistance after bending cycles. Moreover, they also tested the electrochemical performance after the flexibility test with no changes in peak current or peak separation of ferricyanide. A positive conclusion was also obtained from the stretching test with a relative resistance increase to 131% after 100 stretching cycles suggesting robust mechanical stability of the electrodes. The sensor was successfully used to monitor changes in H_2O_2 released by cells upon treatment of PMA or 20% stretching considering the mechanical strain on the cells. While the figure of merit reported was good (2.68, lambda = 550 nm), the final electrode transparency was not reported and therefore a direct comparison with the previous work was not determined. In the most recent report from 2023, platinum NPs were electrodeposited onto SWCNT spin-coated PET film previously patterned using photolithography (220). The Pt NPs improved the redox kinetics of ferricyanide and increased the hydrophilicity of the electrode surface with a decrease in contact angle from 97° to 82°. The electrode with about 75% transparency was used to oxidise H_2O_2 at 0.6 V vs Ag|AgCl and showed good reproducibility (5% RSD), and response under different bending angles (15° - 90°, 1.3%). Furthermore, the PtNPs/SWCNTs/PET sensor was used to monitor H_2O_2 release from HeLa cells upon treatment with PMA.

While the three transparent sensors demonstrated a desirable LOD, a broad linear range, and robust mechanical stability, their translation into contact lenses devices could be challenging. For instance, incorporating an AgNWs-MCE membrane may present biocompatibility issues, as the exposure of the contact lens hydrogel to acetone vapor at 75 °C could potentially result in the retention of harmful toxin (273) Similar concerns arise during the electrode patterning process, where the use of toxic chemicals in the etching process of photolithography poses a risk(220,273) . Moreover, when contemplating the mass production of these technologies, electrodeposition emerges as a limiting step(214,273).

Despite potential solutions to overcome these limitations, the search for cost-effective materials for the fabrication of affordable contact lens diagnostics on a global scale remains a challenge.

Currently, all electrodes employed in the construction of transparent and flexible electrochemical sensors for H_2O_2 detection include rare and less abundant elements such as Ag, Pt, and Au(214,220,273). Hence, it is imperative to explore more readily available raw materials for the advancement of these technologies that meet the discussed properties such as optical transparency, high conductivity, and ophthalmic biocompatibility.

5.1.2 MXenes in the ophthalmic environment

While various *in vitro* and *in vivo* studies have consistently demonstrated the overall biocompatibility of MXenes with diverse cell lines and animal models (as discussed in Section 1.4.1.4), their evaluation within the ophthalmic environment is still in its infancy[4,5]. The first study assessing $Ti_3C_2T_x$ with ophthalmic cell lines, published in 2020, was tailored for an intraocular lens with an accommodative function(4). Their work demonstrated cytocompatibility, no inflammatory response, and positive resolution of wound-healing of human lens epithelial cells towards $Ti_3C_2T_x$ coated lenses(3,4). While this work suggests the potential to use MXenes in ocular lens- based devices, the cytocompatibility using human cornea epithelial cells has yet to be investigated.

5.1.3 Gap in knowledge

Although transparent and flexible electrochemical sensors for H_2O_2 have been reported, significant challenges remain in the development of this technology within a contact lens- based sensor as an ophthalmic diagnostics tool. It is crucial to select appropriate materials that meet the stringent requirements of contact lenses, including flexibility, optical transparency and ophthalmic biocompatibility, whilst also having the capability to perform as an electrochemical sensor for ophthalmic diagnostics. Yet, current publications incorporating electrochemical sensors to contact lenses for glucose, fail to assess the device biocompatibility.

In Chapter 3, the electrochemical performance of flexible and transparent $Ti_3C_2T_x$ electrodes was demonstrated using ruthenium hexamine. In Chapter 4, $Ti_3C_2T_x$ electrodes for the detection of H_2O_2 in simulated tear fluid were optimised which shows potential for ophthalmic diagnosis.

The simple processing of $Ti_3C_2T_x$ due to their ready dispersibility in water upon synthesis, suggests straightforward incorporation onto polymer substrates without the need for harmful chemicals. Additionally, their elemental chemistry where both Ti and C are within the most abundant elements on Earth, suggest a cost-effective approach to overcome pricy materials such as noble metals including Pt and Au. Therefore, it is hypothesised that $Ti_3C_2T_x$ can be used as a pristine electrode incorporated into a contact lens for the electrochemical detection of H_2O_2 while matching the strict requirements of ophthalmic diagnostics. This chapter centres on the integration of a $Ti_3C_2T_x$ electrode into commercially available contact lenses and evaluates their performance in electrochemical detection of H_2O_2, along with assessing biological compatibility.

5.1.4 Research objectives

1. To incorporate and characterise pristine $Ti_3C_2T_x$ electrode onto a commercially available contact lens.
2. To study the interaction between the $Ti_3C_2T_x$-coated contact lens and human corneal epithelial cells.
3. To demonstrate the $Ti_3C_2T_x$-coated lens utility as a transparent and flexible electrode for the detection of H_2O_2.

5.2 Materials and Methods

5.2.1 Materials

- MyDay daily disposable lenses (Stenfilcon A / 54%, Cooper vision)(274)
- Complex salt solution (CSS, Section 4.2)
- Simulated tear fluid (STF, Section 4.2)
- Human Corneal Epithelial (HCE) cell lines (B-3, LGC Standards ATCC)
- Dulbecco's Modified Eagle Medium (DMEM) (Gibco, UK)
- Fetal bovine serum (FBS, Sigma Aldrich, UK)

- Non-essential amino acids (NEAA, Gibco, UK)
- Phosphate buffered saline (PBS, Oxoid, UK)
- Trypsin-EDTA (0.25%, Gibco, UK)
- Trypan Blue Stain (0.4%, Gibco, UK)
- CellTier 96 Aqueous One Solution Cell Proliferation Assay kit (Promega Corporation, UK)
- Dibutyltin maleate (Hydro Polymers Ltd, UK)
- CytoTox 96 Non-Reactive Cells Proliferation Assay kit (Promega Corporation, UK)
- Hydrogen Peroxide (30%, Fisher Scientific, UK)
- IL-6 and IL-8 Enzyme-linked immunosorbent assay (ELISA, BD Biosciences, UK)
- High affinity binding 96-well plate for ELISA (Fisher Scientific, UK)
- Polyethylene (PET) sheets (200 μm in thickness, Express Polyethylene, UK)
- Bradford protein assay kit (Bio-Rad)

5.2.2 Immobilization techniques

Circular or rectangular samples of the contact lens were obtained by cutting the lens using a hole punch (diameter = 0.6 mm) or a surgical blade. The samples were then placed between two thin PET layers. Subsequently, these samples were sandwiched between two glass slides and secured with clips to ensure even pressure was applied to maintain a flat surface. The assembled samples were left to dry for 24 hours. After drying, the glass slides were removed by unclipping them, and one of the two thin plastic layers was carefully peeled off.

5.2.2.1 Drop-casting

A drop of 2.5 μL of a concentrated $Ti_3C_2T_x$ colloidal solution (20 mg mL^{-1}) was placed in the middle of the circular sample using a mechanical pipette. The MXene colloidal solution was gently spread along the sample using the side of a plastic pipette tip and avoiding contact with the hydrogel substrate. The samples were then left to dry for 24 hours before further use.

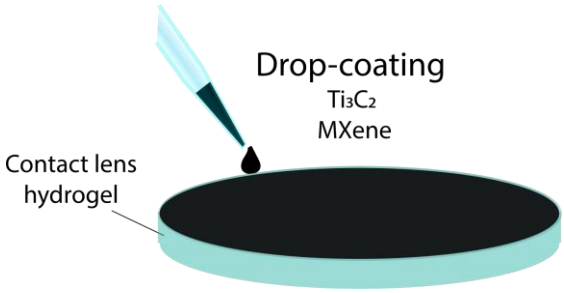

Figure 5.1. Schematic of incorporation of the pristine $Ti_3C_2T_x$ electrode onto a sample of a commercially available contact lens by drop casting.

5.2.2.2 Spray-coating

A colloidal solution of $Ti_3C_2T_x$ MXene at a concentration of 5 mg mL^{-1} was prepared. The rectangular contact lens samples were coated with the MXene solution using a spray gun. A total of 10 mL of the colloidal solution was sprayed over eight samples simultaneously for a duration of 15 minutes. The spray gun was positioned approximately 25 cm away from the samples, and spraying was interspersed with air drying using a hairdryer positioned at a distance of 50 cm.

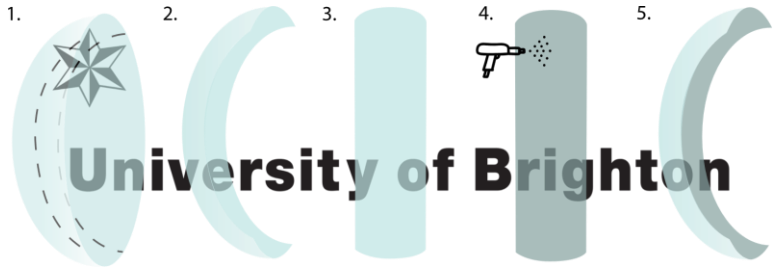

Figure 5.2 Steps followed to obtain a $Ti_3C_2T_x$-coated lens sample. (1-2) Cutting of the lens sample using a surgical blade, (3) followed by drying in the sample in a planar surface, (4) finally spray-coating $Ti_3C_2T_x$ colloidal solution and (5) allowing it to return to its normal spherical shape.

5.2.3 Contact Angle

Contact angle measurements were conducted using the SCA 20 software (OCA 15EC, DataPhysics Instruments GmbH, Germany). A dosage of 5 μL of DI water was dropped using the sessile drop method. To determine contact angle measurements, the baseline and ecliptic outline tools were utilised in the SCA 20 software.

5.2.4 Electrode stability

The CL solution in which the CL was packed, was stored before disposing the packaging. Circular hydrogel LF- and SF-coated and uncoated samples (n=5) were placed in a 48-well plate and incubated in CL storage solution (250 uL) at 21 ^{o}C for 1 week. Supernatants were combined and centrifuged at 10,000 rpm for 10 mins to collect potential leached MXene. Precipitations were redispersed in 1 mL of DI water and analysed by UV-vis spectroscopy at a wavelength of 780 nm.

5.2.5 Protein absorption

Supernatants from circularly coated and uncoated samples, incubated in either CSS or STF containing 10 mg mL-1 of bovine serum albumin, were analysed using the Bradford assay. After the 24 h incubation period, the samples underwent three washes in DI water and were subsequently immersed in a 3% SDS solution for 1 hour at 21 ^{o}C in a shaking incubator. Following the established manufacturing protocol, 5 μL of each sample was combined with 250 μL of the Bradford reagent. Unknown protein concentration was calculated using, a calibration curve with BSA in a concentration range of 0 to 1 mg mL^{-1} in CSS adding 5 uL of each concentration added to 250 uL of the Bradford reagent. Sample absorbance was recorded using UV-Vis spectrophotometry at a wavelength of 490 nm.

5.2.6 Cell culture conditions

The HLE cells were cultured in a complete medium of Dulbecco's Modified Eagle's Medium (DMEM) supplemented with 20% (v/v) fetal bovine serum (FBS) and 1% non-

essential amino acids (NEAA) in flasks of 80 cm^2 surface area and incubated at 37 C and 5% CO_2. Upon 75% confluence, cells were passaged by standard trypsinization using 2 mL of trypsin and 2 minutes incubation. Trypsin was diluted in 2 mL media and cell suspension was centrifuged for 5 min at 125 g. The supernatant was aspirated, and the pellet was redispersed in MEM from which 10 uL of the solution was used for cell counting and the remainder for reseeding

5.2.7 Cell viability assays

In a 48-well plate HLE cells were seeded at a density of 2 x 10^4 cells/well. For the standard curve, a top concentration of 4x10^4 cells/well in RPMI media was prepared with subsequent serial in well trituration and dilution down to 0 cells/well in 8 steps in triplicate. After a 24 hr incubation, the media was removed and 100 uL of fresh media was added followed by the MXene-coated or uncoated lenses and finally another 150 uL of fresh media was added. The treatment lasted 12 hrs during which the 48-well plate was left incubating at 37 ^oC with 5% CO_2. MTS assay

For the MTS assay (CellTiter 96® Aqueous, One Solution, Cell Proliferation Assay, Promgega, UK) dibutyltin maleate leachate was selected as the positive control due to its known cytotoxicity and its common use (275). Dibutyltin Maleate leachate was prepared by incubating with dibutyltin maleate in RPMI (0.1 mg mL^{-1}). The polymer was then removed and dibutyltin maleate leachate was filtered and added to cell-containing predetermined wells at the time when treatments (contact lenses) were added (t=24 hrs). The negative control was cells without contact lens incubation. Moreover, to consider possible interference between the contact lens and $Ti_3C_2T_x$ MXene with the MTS reagent, conditions without cells were prepared with contact lens with and without $Ti_3C_2T_x$ coatings. These enable obtaining backgrounds to individual conditions that could be subtracted to avoid interference. After the 12 hr incubation period, the media of all wells including negative and positive controls was transferred to a different plate and the contact lens samples were removed by aspiration. Following the supplier's protocol, 100 µL of MTS reagent were added to each well and the plate was incubated for 2 hr at 37 ^oC.

Following incubation, the solutions were carefully transferred to a new 96-well plate and absorbance readings were taken using an ELx800 Universal Microplate reader (Biotek, UK) at a wavelength of 492 nm(276). Each experiment consisted of triplicate wells per condition, and the experiment was repeated 3 times with different cell populations. To determine cell viability (%), raw values of no cell-containing samples were subtracted to their corresponding cell-containing condition. This was with the aim of remove potential background absorbance. Then, cell viability was determined utilising the negative control as 100%.

5.2.7.1 LDH release

For the negative control of the LDH assay (CytoTox 96® Non-Radioactive Cytotoxicity Assay, Promega, UK), 45 mins before the completion of the 12 hr incubation, 25 uL of 10X lysis solution provided by the supplied was added per well and the plates were returned to incubation (37 ºC with 5% CO_2)(277). Once the 12 hr incubation was completed, the media was transferred to Eppendorf tubes from which 50 uL per sample were transferred to a 96-well plate. The samples were left to cool to room temperature before adding 50 µL of the reagent solution to each well. The plates were cover in foil and incubated for 30 mins at room temperature. Then, 50 uL of the stop solution and the absorbance readings were taken within an hour using the microplate reader at a wavelength of 492 nm. Each experimental condition included triplicate wells, and the entire experiment was replicated three times using distinct cell populations. Lysed cells were use as 100% to determine cell cytotoxicity (%) of samples after removing the background absorbance.

5.2.8 Electrochemical measurements

Amperometry was the technique used to electrochemical detect H_2O_2 using the $Ti_3C_2T_x$-coated contact lens samples. An applied potential of -1050 mV vs Ag|AgCl was utilised in a three electrode system with a platinum wire as the CE. Simulated fluid with a BSA protein content of 10 mg mL^{-1} was chosen as the electrolyte.

To test the performance of the transparent electrode in bending state, three conditions were considered: A. straight form, which was achieved by having a glass substrate in the back of the lens samples, B. the natural curved shaped of the contact lens, and C. the electrode was bent 100 times (50 inward and 50 outward bends) and the electrochemical measurement was recorded in its natural curved shaped as condition B. To avoid tearing of the contact lens or the disruption of the MXene coating, aluminum was used at the alligator clip to protect the sample.

5.2.9 Statistical analysis

Data analysis was performed using GraphPad Prism 5 (GraphPad Software Inc., USA). The data was expressed as mean ± SD, with $n > 3$, specified in each study. Statistical analysis involved either a one-way ANOVA with Turkey's comparison where applicable. Significance levels were determined with a p-value less than 0.05.

5.3 Results and Discussion

5.3.1 Characterization of $Ti_3C_2T_x$ electrode onto hydrogel

To confirm the successful incorporation of thin $Ti_3C_2T_x$ coatings onto the contact lens samples, transmittance was recorded using UV-vis spectroscopy. As shown in Figure 5.3, the characteristic UV-vis spectra of $Ti_3C_2T_x$ was observed from which an absorption peak at 780 nm corresponds to the plasmonic peak characteristic of $Ti_3C_2T_x$. The transmittance of the coating was determined to be 94.1 % (± 0.8) at the standard wavelength of 550nm, which is typical for optically transparent devices.

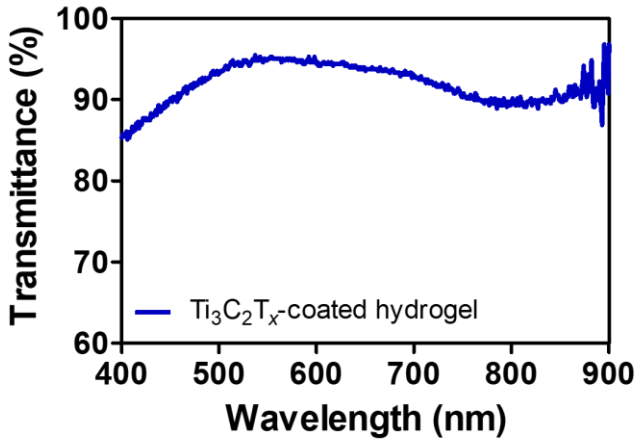

Figure 5.3 UV-visible spectroscopy of $Ti_3C_2T_x$ coated hydrogel

5.3.2 Impact of $Ti_3C_2T_x$ in hydrophilicity of lens

Contact angle measurements were taken to assess the effect of $Ti_3C_2T_x$ coatings on contact lens wettability. Representative optical images were captured, using 5 uL drops on an uncoated-lens (Figure 5.4a), a lens coated with large flake $Ti_3C_2T_x$ - (Figure 5.4b) and a lens coated with small flake $Ti_3C_2T_x$ (Figure 5.4c). It is evident that the droplet on the uncoated lens maintained a more rounded shape, indicative of a comparatively hydrophobic surface to that of the MXene-coated lenses. This observation was further supported by statistical analysis of the inner contact angle measurements of the test, MXene coated and uncoated, control samples

(Figure 5.4d). A significant reduction in contact angle measurement ($p<0.05$) was observed for both the large and small flake samples compared to the uncoated samples indicating that MXene creates a more hydrophilic surface than that of the uncoated lens. The inner contact angle significantly decreased from 88.8 (± 1.8) degrees for the uncoated samples to 61.4 (± 8.1) degrees and 58.5 (± 2.9) degrees for the large- and small-flake coated samples, respectively. This decrease aligns with the high hydrophilicity of $Ti_3C_2T_x$ flakes from the current understanding of MXene wettability(278). Theoretical and experimental studies have demonstrated hydrophilic interaction is enhanced predominantly by oxygen-containing terminations of $Ti_3C_2T_x$. For example, using molecular dynamics simulations, $Ti_3C_2T_x$ was alkalised replacing the -F termination by -OH termination, and as a result, the inner contact angle decreased by 19 degrees (278,279). Moreover, a comprehensive review of reported contact angle revealed a decrease in contact angle with an increase in surface roughness, explained by the Wenzel model, which assumes grooves between the solid material, in this case between MXene flakes, for liquid to penetrate. Consequently, the increase in an interfacial area between water and $Ti_3C_2T_x$ surface, due to an increase in surface roughness, results in energetically favourable.

Additionally, a negative correlation between the flake size of pristine $Ti_3C_2T_x$ and wettability has been reported(278,280). However, no significant difference (Figure 5.4d) was observed for the $Ti_3C_2T_x$ -coated samples despite the decrease in flake size from >1000 nm to 270 nm (Figure 3.1). This is likely due to a unique nano-macrostructure formed within the coating considering the non-uniform substrate (hydrogel). Unique nano-macrostructures have been theorised to explain the observation of both positive and negative correlations between surface roughness and contact angle with various flake size distributions. However, it is not feasible to consider these trends, as further imaging would be required to determine the organization of $Ti_3C_2T_x$ flakes deposited on top of the non-uniform hydrogel sample.

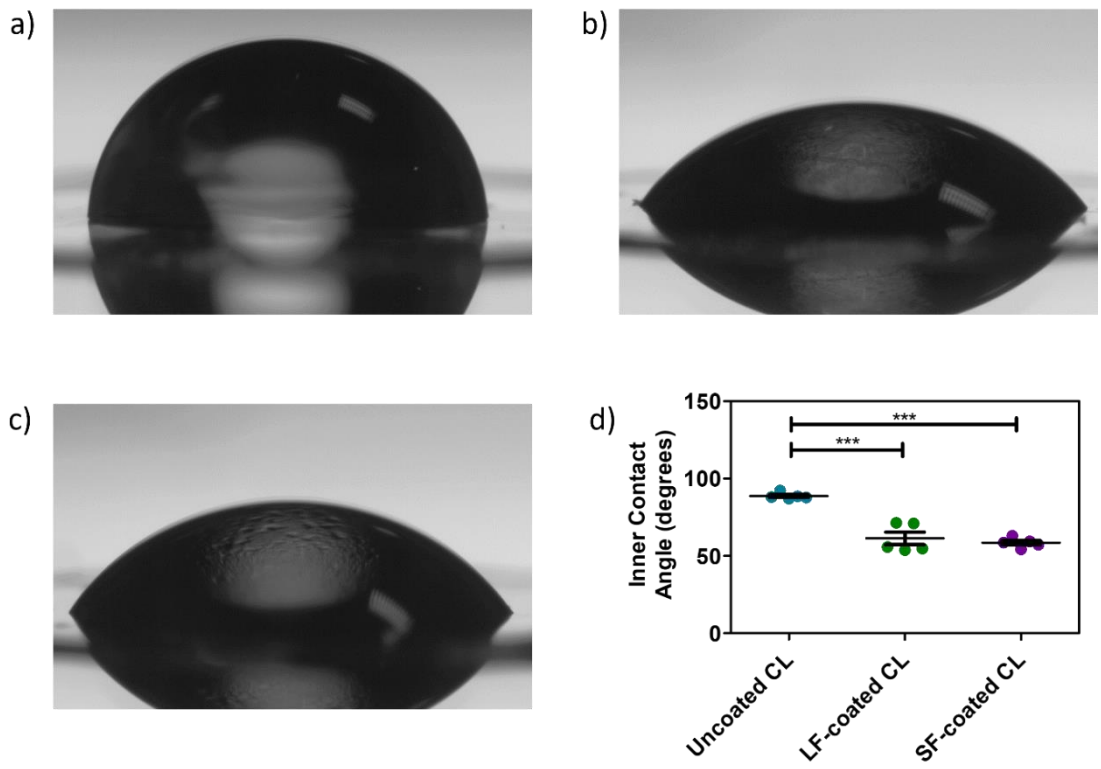

Figure 5.4. Optical images of 5 uL deionised water onto a) uncoated contact lenses (control), and contact lenses coated with b) large-flakes (LF) and c) small-flakes (SF) $Ti_3C_2T_x$. Inner contact angle measurements (n=6, $p<0.05$, data shown as mean ± SD, one-way ANOVA with Turkey's comparison).

It is important to note that the samples were tested in their dried state, as the high hydrophilicity of wet samples would immediately absorb the 5 µL droplet, making it difficult to capture images and measure the contact angle upon contact. To explore the impact of $Ti_3C_2T_x$ coatings on the swollen state of the lenses, a captive bubble method should be performed(281).

5.3.3 Stability of $Ti_3C_2T_x$ coating

The stability of the coatings was investigated in saline storage solution. To consider the lens in its packaging state, coated and uncoated samples were incubated in contact lens storage solution for 1 week. As shown in Figure 5.4, the characteristic peak of $Ti_3C_2T_x$ at around 780 nm was not identified for any of the samples. It is important to note that the sensitivity of

UV-vis spectroscopy is relatively low compared to other techniques. The lowest concentration of MXene that may be detected is about 10 ug mL^{-1}, estimated from the calibration curve of $Ti_3C_2T_x$ colloidal solution in DI water shown in Chapter 2, Figure 2.6. Therefore, these results only confirm that if there had been any leaching of $Ti_3C_2T_x$ from the coating to the solution it was below 2 µg, considering all the samples (n=5) for each condition were combined into one cuvette. Moreover, the current coating samples assume the electrode would have a large surface area (0.28 mm^2), which is typically beyond what seems to be suggested in the illustration designs by reports developing contact lens diagnosis(110,113). Therefore, it is likely that if there was any leaching of MXene during storage, it would be below 2 µg relative to the size of the electrode. Moreover, a cytocompatibility assessment of MXene-coated lenses in Section 5.3.5, considers the potential impact of MXene leachate in media which is commonly performed in literature(282). Future studies should consider the stability of the coating under mechanical stress and strain, such as scratching and stretching, which can easily occur during the handling of contact lenses.

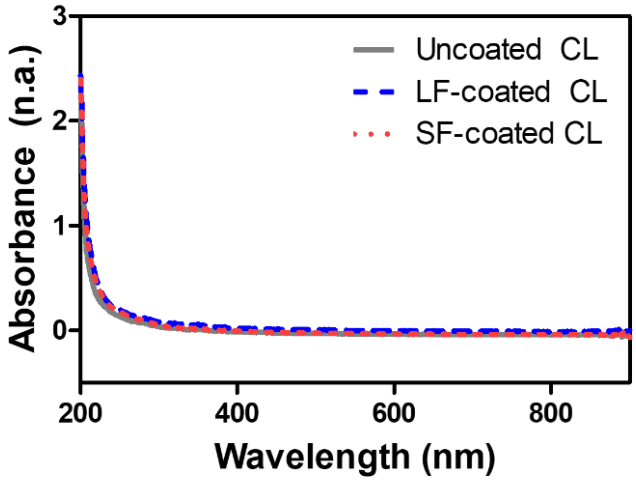

Figure 5.5. Stability assessment of $Ti_3C_2T_x$-coatings after one week of storage. UV-vis spectra of contact lens storage solution incubated for 7 days in large flake (LF) and small flake (SF) $Ti_3C_2T_x$ coated and uncoated contact lens samples.

5.3.4 Protein adsorption

To investigate the impact of $Ti_3C_2T_x$ coatings on protein adsorption, the Bradford assay was used. Figure 5.5a shows the standard curve to validate the assay using BSA at a concentration range of 0-1 mg mL^{-1} in 0.1M PBS solvent. In accordance with the assay's protocol, a linear relationship (R^2=0.936) was observed at an absorbance at 490 nm and protein concentration in a range between 0 and 1 mg mL^{-1} BSA in PBS (0.01 M) indicating assay suitability for measurement of unknown protein concentration in this concentration range (Figure 5.6a). Following a 24-hr incubation period in simulated tear fluid with (10 mg mL^{-1}) and without (CSS) BSA, samples were washed and SDS (3%) was used to detached absorbed BSA from the lenses. As shown in Figure 5.5b, no significance difference was observed for the contact lenses with and without coatings suggesting that $Ti_3C_2T_x$ does not promote protein absorption when used as a coating to contact lenses regardless of flake size. It is important to note that the sensitivity of this assay may not be appropriate for the potential absorption of protein by the samples and therefore only qualitative conclusions can be drawn.

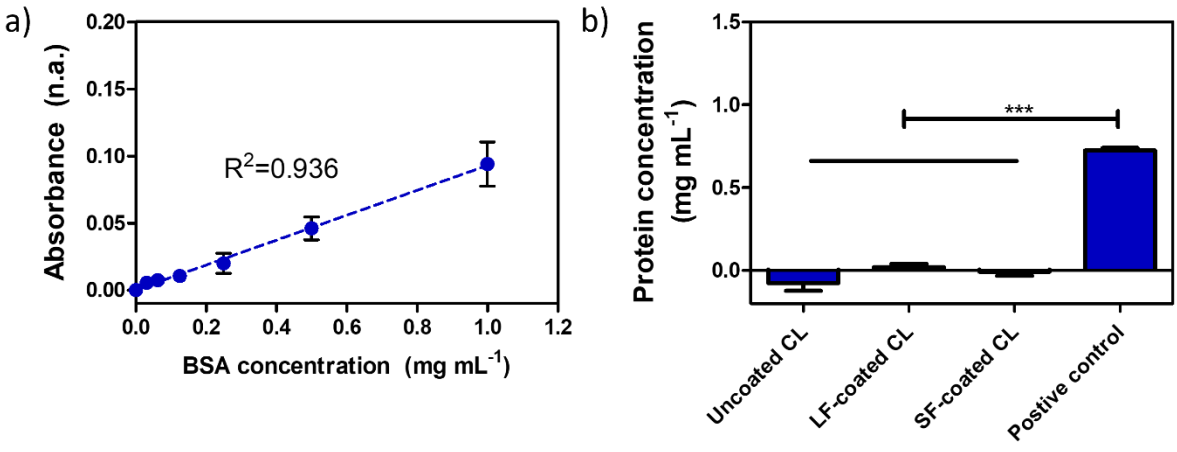

Figure 5.6 Comparison in protein absorption of $Ti_3C_2T_x$-coated and uncoated contact lens samples. a) Bovine serum albumin (BSA) in sodium dodecyl sulphate (SDS) standard curve using Bradford assay. b) Calculated total concentration of protein (mg mL^{-1}) upon SDS wash

after a 24 hr incubation simulated tear fluid (10 mg mL^{-1} BSA). (n=3, $p<0.05$, mean ± SD, one-way ANOVA with Turkey's comparison)

5.3.5 Biological assessment of $Ti_3C_2T_x$-coated contact lenses

The utilization of the MTS and LDH assays provided valuable insights into the viability of human epithelial cells (Figure 5.7) subsequent to a 12-hr incubation with uncoated and $Ti_3C_2T_x$ -coated contact lens samples. These assays, widely recognised for their role in assessing cell viability and cytotoxicity, respectively, serve as an indicator of potential toxicity in cell cultures. First, optimisation of cell seeding was performed through a standard curve (R^2=0.996) as shown in Figure 5.7a using the MTS reagent. The chosen cell seeding density was 2 x 10^4 cells mL^{-1} for the following experiments. As shown Figure 5.7b there was a significant decrease in cell viability when cells were treated with positive cytotoxic control tin maleate. No significant difference was observed between the coated and uncoated CL samples ($p<0.001$) suggesting cytocompatibility of the $Ti_3C_2T_x$ coatings for corneal lens epithelial cells. Moreover, results suggest that cell-viability was flake size-independent which is a parameter that has been known to vary interaction between different nanomaterials and cell lines. A slight decrease in cell viability was observed between the negative control (cell only) and cells treated with contact lenses irrespective of their coatings. It is assumed that this is due to a slight physical disruption when removing the sample before addition of the MTS reagent, as previous reports following different protocol report good cell viability of HCECs treated with CLs.

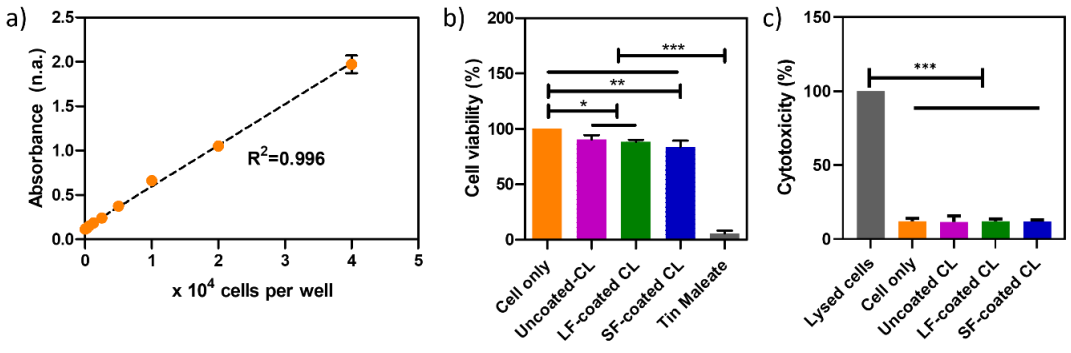

Figure 5.7. Impact of large flake (LF) and small flake (SF) $Ti_3C_2T_x$ coatings of contact lenses on human corneal epithelial cell cytocompatibility. a) Standard curve using MTS of different seeding cell concentration in a 48-well plate. b) Cell viability and c) cell cytotoxicity of different treatments upon a 12-hr incubation utilizing MTS and LDH assays, respectively, with a seeding density of 2 x 10^4 cells per well. (n=3, $p<0.001$, data shown as mean ± SD, one-way ANOVA with Turkey's comparison)

Cell cytotoxicity was determined using the LDH assay in which the positive control was a lysed cell solution (10X) using cell lysis buffer from the LDH assay kit (CytoTox 96® Non-Radioactive Cytotoxicity Assay, Promega). Results (Figure 5.87) are in agreement with the previous conclusion using the MTS assay in which no significant difference was observed between coated and uncoated samples nor between flake size-coatings. Moreover, there were no differences between cell only control and lens-treated cells. This suggests that potentially the physical disruption of cells was not damaging enough to break the cell membrane and therefore no LDH release, indicative of cell lysis, was detected.

5.3.6 Immune response of $Ti_3C_2T_x$-coated contact lenses

To assess the immune response of $Ti_3C_2T_x$ coatings, ELISA assay was performed to quantify the release of pro-inflammatory cytokine markers IL-6 and -8. The first step was the optimisation of the cell supernatant dilution for the positive control (Lipopolysaccharide (LPS) sample) using a series of dilutions consisting of 1 (supernatant) to 10, 20, 50 and 100 (0.1 M

PBS) (0.1, 0.05, 0.02 and 0.01). The LPS-treated sample was chosen, as these samples tended to have the highest secreted cytokine concentration and the use of the resultant optimal dilution factor from these samples would ensure that unknown sample values fitted within the range of the standard curve. As shown in Figure 5.8a, the linear range of curve occurred from 0 up to the 1:20 dilution point and began to plateau beyond this concentration. Therefore, the chosen supernatant dilution for the IL-6 assay was 1 in 25 ensuring the sample is within the linear range. For the IL-8, the concentration selected was 1:200 in order to fit within the linear range. The increase in IL-8 expression compared to IL-6 expression in HCECs matches the expression profile seen in other ocular cell lines such as lens epithelial cells (3,4,23).

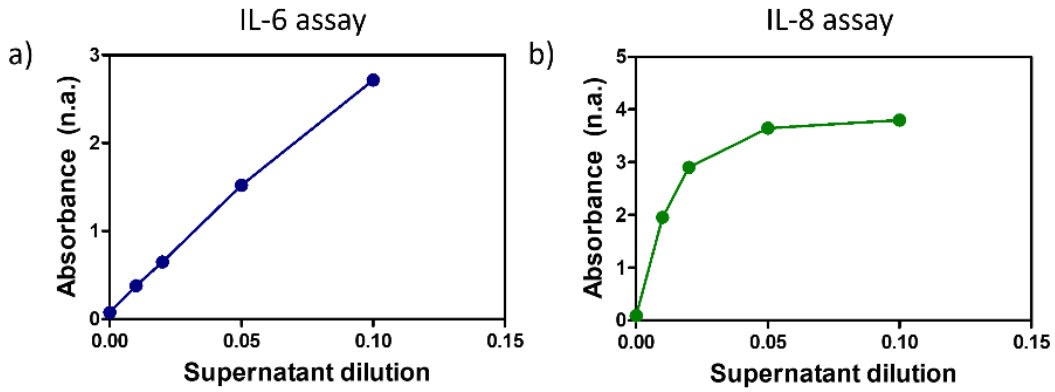

Figure 5.8. Determination of supernatant dilution required for ELISA assays. Absorbance values corresponding to a) IL-6 and b) IL-8 release found in cell supernatant diluted in 0.01 M PBS.

The standard curves for IL-6 and IL-8 are presented in Figure 5.9a and b, respectively. The analysis revealed no substantial upregulation of IL-6 (Figure 5.9c) or IL-8 (Figure 5.9d) in the lens-treated samples compared to the cell-only control. This suggests that the $Ti_3C_2T_x$ -coated lenses did not induce a significant pro-inflammatory response measured through upregulation of key inflammatory cytokines IL6 and IL8. These cytokines are involved in the regulation of multiple processes in corneal inflammation and wound healing, including neovascularization and stimulation of immune cells(283,284). As anticipated, the positive LPS treated control,

exhibited a considerable upregulation of both IL-6 and IL-8, validating the sensitivity of the assay and confirming the expected response to a potent immune stimulant.

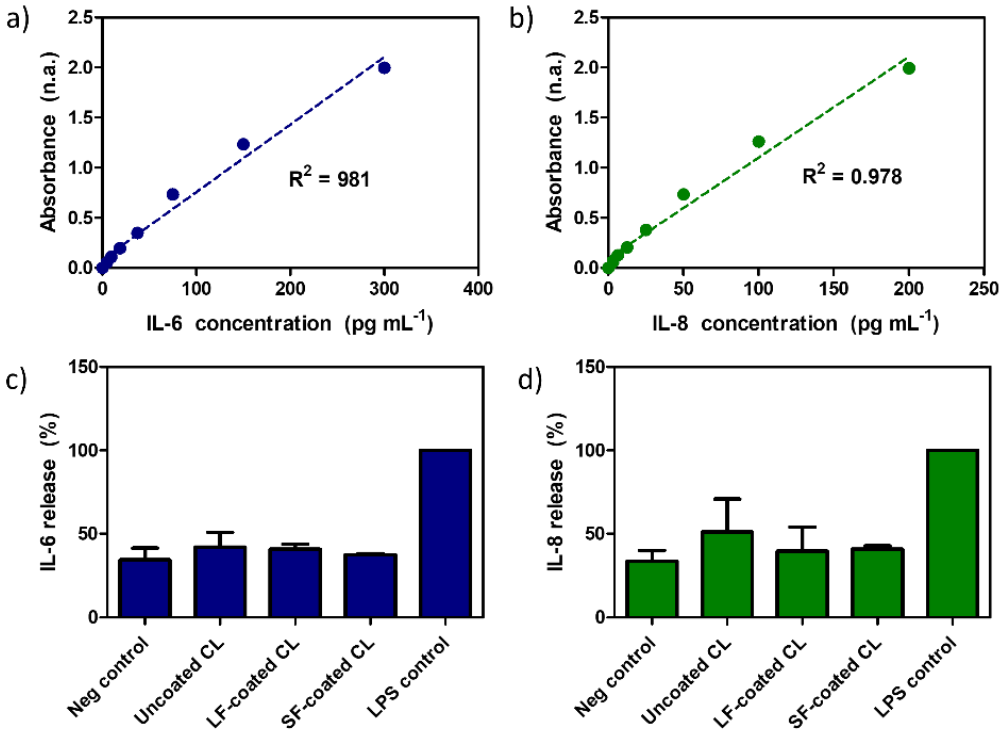

Figure 5.9 Impact of $Ti_3C_2T_x$-coatings on cytokine release by HCE cells. Standard curves of a) human interlukin-6 ELISA kit, and b) human interlukin-8 ELISA kit. Quantification of c) IL-6 and d) IL-8 release from HCE cells treated with uncoated and $Ti_3C_2T_x$-coated contact lenses (CL). Negative control refers to untreated cells and LPS is the positive control. (n=2, $p<0.05$, data shown as mean ± SD, one-way ANOVA with Turkey's comparison)

5.3.7 Demonstration of electrochemical performance of $Ti_3C_2T_x$-coated contact lenses

To demonstrate the electrochemical performance of $Ti_3C_2T_x$-coated hydrogels as working electrodes, amperometry was applied for the detection of H_2O_2. Three different configurations were considered as shown in Figure 5.9a; Configuration A – $Ti_3C_2T_x$ electrode as a coating of the lens in a glass substrate to maintain a straight structure, Configuration B –

$Ti_3C_2T_x$ electrode as a coating of the lens without a substrate resulting in a natural concave structure during measurement, Configuration C – 100 bends prior to electrochemical measurement following Configuration B. Figure 5.9b shows representative amperometric responses to the addition of 500 µM of H_2O_2 in simulated tear fluid at t=50 s with an applied potential of -1050 mV (vs Ag|AgCl) indicating successful electrochemical detection using a $Ti_3C_2T_x$ coated contact lens electrode. There was no significant difference between the faradaic response to H_2O_2 following flexing cycles (Figure 5C) suggesting that the $Ti_3C_2T_x$ coating can be used as a flexible and transparent electrode without compromising the performance of the sensor.

The visible transmittance value of these electrodes (94.5%, Figure 5.3) is above the required transmittance of commercially available contact lenses (>90%)(281). This confirms the suitability of $Ti_3C_2T_x$ thin film coatings for practical application in wearable ophthalmic devices. Moreover, tinted contact lenses for UV protection and several eye conditions management, have been reported with transmittance values >50%(285–287). Therefore, having confirmed that electrode thickness does not impact the electrochemical performance of pristine $Ti_3C_2T_x$ electrode (Figure 4.2a), future studies could consider different MXene coatings and thicknesses to tailor light transmittance (%) for ocular disease management.

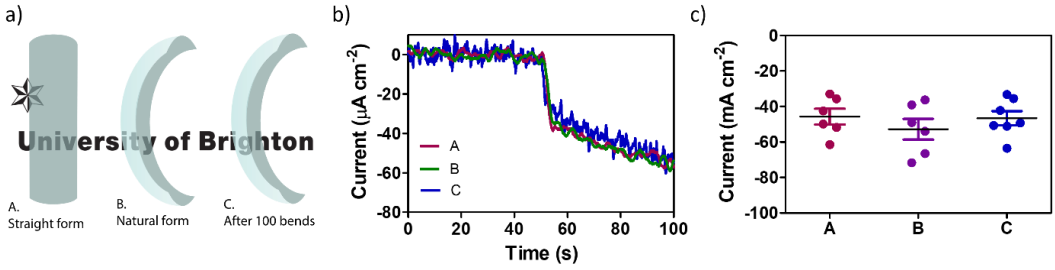

Figure 5.10. Impact of flexibility in electrochemical performance of transparent $Ti_3C_2T_x$-coated contact lenses. a) Schematics of electrode conditions (A, straight form, B natural form, and C electrode after 100 bends, 50 inward and 50 outwards). b) Amperometric responses to an addition of 500 µM H_2O_2 at t=50 s in tear simulated fluid at -1050 V vs Ag|AgCl. c)

Comparison of normalised current by surface area (mA cm^{-2}) between electrode configurations. (n=6, $p<0.05$, data shown as mean ± SD, one-way ANOVA with Turkey's comparison)

5.4 Conclusion

In summary, this chapter successfully incorporated a pristine $Ti_3C_2T_x$ electrode onto a commercially available contact lens, and UV-vis spectroscopy was employed to confirm the successful integration of MXene onto the hydrogel. The stability study demonstrated that MXene did not leach from the contact lens over a one-week period when incubated in contact lens storage solution. This conclusion was drawn by analysing the incubated solution using UV-vis spectroscopy, which did not exhibit any identifiable MXene spectra. Contact angle measurements revealed an increase in wettability of the lens upon incorporation of $Ti_3C_2T_x$ coatings, and this difference was independent of flake size. Moreover, results from the Bradford assay indicated no specific increase in protein adsorption on $Ti_3C_2T_x$-coated contact lenses compared to uncoated controls, suggesting no protein fouling. Cytocompatibility studies using a human corneal epithelial cell line demonstrated good cell viability for the coated-contact lenses compared to non-coated ones, indicating their biocompatibility in an ophthalmic environment. Electrochemical studies showcased the transparent pristine $Ti_3C_2T_x$ coating on a contact lens as a sensor for H_2O_2, demonstrating that repeated cycles of mechanical stress did not impact sensor detection capacity. These findings highlight the suitability of the coating for wearable devices that may experience mechanical stress during use. These findings have significant implications for the development of contact lens-based sensor technology, wearable devices and biosensors.

6 Conclusions and Future work

In this concluding chapter, a summary of findings derived from the investigation of a pristine $Ti_3C_2T_x$ MXene electrode for the electrochemical detection of the biomarker H_2O_2 in tear fluid is presented (Section 6.1), aiming to address the objectives outlined at the onset of this study while highlighting the broader impact of the work. Then, Section 6.2 focuses on assessing the hypotheses with the results presented, guided by the objectives of each chapter. Finally, Section 6.3 presents avenues for future work that can build upon the current study and advance the field of ophthalmic diagnostics with the use of $Ti_3C_2T_x$ MXene.

6.1 Comprehensive analysis and implications of research findings

6.1.1 Processing of pristine $Ti_3C_2T_x$ electrochemical sensors

The fabrication protocol of pristine $Ti_3C_2T_x$ electrodes, as illustrated in Figure 1.3, along with the successful development of thin coatings through spray coating (Figure 2.7 and Figure 5.1) and drop-casting (Figure 5.1), highlights the ease of processing $Ti_3C_2T_x$ colloidal solution onto electrochemical sensors. Moreover, the incorporation of pristine $Ti_3C_2T_x$ electrodes onto different substrates, such as Kapton tape (Chapter 2-4), glass (Chapter 2 and 3), and hydrogels (Chapter 5), demonstrates their integration onto diverse surfaces without the need of complex processing techniques or treatments. Notably, these electrodes consistently exhibit excellent electrochemical performance regardless of the fabrication method or substrate used, emphasizing their potential for developing sensors tailored to unique applications.

For instance, the incorporation of pristine $Ti_3C_2T_x$ electrodes onto Kapton tape enables the creation of flexible and wearable sensors for on-body monitoring(288), which may have applications in healthcare settings to track physiologically important molecules. Conversely, the integration of pristine $Ti_3C_2T_x$ electrodes onto glass substrates allows for the fabrication of transparent and robust sensors suitable for environmental monitoring applications, including the detection of pollutants in water samples or the monitoring of air quality. Additionally, the incorporation of pristine $Ti_3C_2T_x$ electrodes into hydrogel matrices opens up possibilities for

bioanalytical applications, such as biosensing and drug delivery systems, where the biocompatibility and biofunctionality of hydrogels are crucial(289).

The versatility of pristine $Ti_3C_2T_x$ electrodes, as evident from their successful integration onto various substrates and electrochemical performance, underscores their potential to address specific needs and challenges across diverse application areas. Ongoing research and exploration of this material, coupled with tailored fabrication techniques, hold significant promise for the development of innovative sensors with enhanced performance and functionality. Such advancements will have far-reaching implications in healthcare, environmental monitoring, biotechnology, and beyond, contributing to advancements in various fields and improving our understanding of the world around us.

6.1.2 Optimisation of pristine $Ti_3C_2T_x$ electrochemical sensors

By systematically investigating individual parameters (Chapter 3-4), this study demonstrated that pristine $Ti_3C_2T_x$ could be optimised for specific analytes. The study revealed that larger flakes facilitated outer-sphere electron transfer between ruthenium hexamine and $Ti_3C_2T_x$ (Figure 3.1). In contrast, smaller flakes exhibited higher sensitivity towards hydrogen peroxide (Figure 4.2). Exploring electrode thickness enhanced the faradaic responses compared to the capacitive current (Figure 3.2). An investigation into flake orientation demonstrated increased current density for vertically aligned flakes, while horizontally aligned flakes showed improved electron transfer kinetics (Figure 3.3). Further research on single-flake $Ti_3C_2T_x$ could provide insights into the role of $Ti_3C_2T_x$ edges in electrochemical sensing, including their surface chemistry for redox reactions or edge effects. this work emphasises the imperative nature of comprehensive parametric studies. Notably, the often-overlooked factors such as flake size emerges as a critical parameter with the potential to yield diverse outcomes(179,290). Recognizing the significance of material parameters in MXene applications is pivotal for advancing our understanding and optimizing the performance of materials in various technological domains. As research continues, such considerations will undoubtedly contribute

to the refinement and enhancement of MXene-based technologies, paving the way for innovative applications in diverse fields.

Future investigations should also consider the customization of surface terminations to enhance electrochemical sensing. Various approaches exist for controlling surface terminations during synthesis and functionalization(291,292). For instance, analytes that undergo adsorption-based electron transfer mechanisms may benefit from O-rich surface terminations instead of F-rich surface terminations. Additionally, expanding this research to other MXenes presents an exciting opportunity for the detection of multiple analytes with enhanced sensitivity by tailoring the outer transition metals in MXene structures. For example, vanadium carbide (V_2C) has shown enzyme-like properties, making it an excellent electrocatalyst for potential applications.

In conclusion, the systematic exploration of pristine $Ti_3C_2T_x$ parameters, as outlined in this study, offers valuable insights for optimizing sensor performance. Further research should focus on understanding the influence of single-flake $Ti_3C_2T_x$ and tailoring surface terminations to unlock the full potential of this material in electrochemical sensing. Expanding the investigation to other MXenes will enable the development of sensors with enhanced capabilities and broaden the scope of applications in various fields.

6.1.3 Pristine $Ti_3C_2T_x$ electrochemical sensor for H_2O_2

While the focus of this work was inspired by the role of H_2O_2 in the tear fluid, H_2O_2 also holds significant importance across various other domains. In environmental science, for example, the detection of high levels of hydrogen peroxide in water samples is crucial due to its potential detrimental effects on aquatic life and ecosystems, emphasizing the relevance of its detection for environmental monitoring(293). In chemical engineering, H_2O_2 is commonly utilised in large-scale industrial processes, such as the production of sodium perborate, sodium percarbonate, and percarboxylic acid (294). These compounds find wide-ranging applications in detergent formulations and bleaching agents. Therefore, the impact of the successful

optimisation of pristine $Ti_3C_2T_x$ electrodes for the detection of H_2O_2 definitely expands beyond the ophthalmic diagnostics to numerous fields.

Moreover, it's crucial to underscore that many electrochemical biosensors operate by monitoring H_2O_2 as a byproduct of various reactions. This fundamental concept was exemplified in the first invented glucose sensor, where the enzymatic oxidation of glucose by glucose oxidase involves oxygen consumption and production of H_2O_2(295). Expanding beyond enzymatic biosensors, the utility of H_2O_2 extends to immunosensors and DNA sensors(296,297). These sensors use H_2O_2 as an intermediate molecule for the detection of a wide range of analytes. In light of this, the work presented in this thesis promotes the exploration of anchoring biorecognition elements onto the surface of pristine $Ti_3C_2T_x$ electrodes. This approach aims to establish a correlation between H_2O_2 detection and the concentrations of numerous analytes, thereby broadening the applicability of $Ti_3C_2T_x$ electrochemical biosensing technologies.

6.1.4 Potential window of pristine $Ti_3C_2T_x$ electrode

As shown in Chapter 4, the potential window established in aqueous electrolytes, such as the biologically relevant 0.1 M PBS, was confined in the positive potential range, reaching only up to 0.2 V vs Ag|AgCl. This restriction poses challenges for the detection of numerous biomolecules that typically undergo oxidation beyond this potential threshold, including substances like ascorbic acid, uric acid, dopamine, serotonin, among others. While this limitation narrows the focus to molecules that can be electrochemically reduced or oxidised at negative potentials, it also suggests that potential interference from other elements may not be as prominent. Chapter 4 of this work substantiates this observation, demonstrating that the selected interferent molecules including dopamine, ascorbic acid, and urea, which typically pose challenges for electrochemical sensors oxidizing H_2O_2 at positive potentials, did not significantly impact the results.

To address these limitations, future investigations should delve into the exploration of composite electrodes incorporating other MXenes beyond $Ti_3C_2T_x$. This strategy aims to leverage the high conductivity of $Ti_3C_2T_x$ while potentially expanding the achievable potential window through the integration of another member from the family of MXenes. This approach could enhance the versatility and broaden the range of analytes detectable by electrochemical sensors, paving the way for more comprehensive and robust biosensing platforms.

6.1.5 Transparent and flexible pristine $Ti_3C_2T_x$ electrodes as a current collector

In this study, transparent and flexible sensors were successfully developed by depositing thin films of $Ti_3C_2T_x$. While these sensors were demonstrated for ruthenium hexamine and hydrogen peroxide detection, it is anticipated that pristine $Ti_3C_2T_x$ can also catalyse the reduction or oxidation of other molecules on its surface. In addition, $Ti_3C_2T_x$ electrode may also be used as transparent and flexible current collector for other sensors. Future investigations should explore the potential of depositing other nanomaterials such as graphene or metal NPs, onto pristine $Ti_3C_2T_x$ electrodes. This approach would enable the development of transparent and flexible electrodes with tailored functionalities. The fabrication of transparent electrodes holds promise for optically monitoring biological processes occurring at the electrode surface during measurements. Furthermore, the demonstrated biocompatibility of $Ti_3C_2T_x$ electrodes suggests their potential application in environments where traditional indium tin oxide electrodes, the standard TCE, may pose environmental toxicity concerns.

6.2 Closing remarks of fundamental study

The overarching hypothesis (Chapter 1) that pristine $Ti_3C_2T_x$ can be incorporated as a flexible, transparent conductive electrode onto a contact lens for electrochemical detection of

biomarkers in the tear fluid, exemplified using hydrogen peroxide, was supported by tackling the aims and research objectives in individual chapters.

Research objective 1, "To synthesise $Ti_3C_2T_x$ MXene and fabricate a pristine electrode with a defined area for use in electroanalytical measurements" was tackled in Chapter 2. Starting with the synthesis of pristine $Ti_3C_2T_x$ flakes utilizing high-Al MAX phase followed by the assessment of material quality and suitability for electrochemical studies using characterisation techniques including XRD, SEM, DLS and 4-point probe. Moreover, the electrode design enabled the fabrication of reproducible electrodes with ease tailorability of material (flake and orientation) and electrode (surface area and thickness) parameters. The reproducible cyclic voltammograms recorded in pristine $Ti_3C_2T_x$ electrodes supported the hypothesis of Chapter 2, that utilizing high-Al MAX phase for MXene synthesis, would result in electrical conductivities appropriate for the development of pristine $Ti_3C_2T_x$ electrodes for analytical electrochemistry.

Research objective 2 "To investigate the impact of material and electrode parameters in the electrochemical performance of pristine $Ti_3C_2T_x$ electrodes" was addressed in Chapter 3. A parametric study focused on the electrochemical activity of pristine $Ti_3C_2T_x$ was performed in Chapter 3. Using ruthenium hexamine, as a standard redox probe, insights into the impact of flake size, orientation and thickness on current densities and kinetics was obtained. The research expanded to examine the electrochemical performance of these electrodes under bending conditions (100 bends and bending during measurement (d=4 mm), crucial for applications requiring flexibility such as contact lenses. Finally, it was demonstrated that the electrochemical performance of transparent pristine $Ti_3C_2T_x$ electrodes was not impact by high optical transmittance. Therefore, the study not only advanced the understanding of parameters

of $Ti_3C_2T_x$ for analytical electrochemistry but also opened the avenues for the development of transparent and flexible electrodes relevant for contact lenses.

Research objective 3 “To optimise pristine $Ti_3C_2T_x$ electrode and the experimental parameters for the detection of a biomarker in simulated tear fluid” was achieved in Chapter 4. Pristine $Ti_3C_2T_x$ electrode was characterised for the electrochemical detection of H_2O_2. The experiment revealed the sensor's operating window in biologically relevant ion concentrations and demonstrated its capability to detect H_2O_2 independently of thickness. While sensitivity could be improved by reducing flake size, large-flake electrodes provided the most stable film. The highest sensitivity was achieved at -1050 mV vs Ag|AgCl, with excellent selectivity for H_2O_2 confirmed. Tests in simulated tear fluid, including protein, showed no interference with accurate detection, highlighting the sensor's robustness. Stability over a 30 minutes measurement and after a 24 hours storage incubation, further underscored its suitability for tear fluid analysis and potential applications beyond ophthalmic diagnostics. With the hypothesis that pristine $Ti_3C_2T_x$ electrodes is an attractive material for electrocatalytic activity towards H_2O_2 was supported.

Research objectives 4 “To incorporate pristine $Ti_3C_2T_x$ electrode onto a contact lens without impacting its electrochemical performance” and 5 “To evaluate the compatibility of the integrated $Ti_3C_2T_x$ electrode on a contact lens with an ophthalmic environment” were addressed in Chapter 5. The successful incorporation of pristine $Ti_3C_2T_x$ electrodes onto commercially available contact lenses was achieved through drop-casting and spray-coating techniques. Positive characterizations, including evaluations of wettability, protein adsorption, and cytocompatibility with a human corneal epithelial cell line, demonstrated the suitability of pristine $Ti_3C_2T_x$-based diagnostics using contact lenses as a platform. The consistent electrochemical performance observed across different sensor configurations underscores the robustness of these flexible and transparent sensors.

In summary, this study marks a significant milestone by presenting, for the first time, an electrochemical sensor utilizing pristine $Ti_3C_2T_x$ MXene. Beyond the novelty of this

achievement, the research underscores the practical advantages inherent in employing $Ti_3C_2T_x$ in such applications. Taking advantage of its optoelectronic and mechanical properties, along with their positive biocompatibility on contact with corneal epithelial cell monolayers and consistent electrochemical performance, the study showcases the efficacy of electrochemical sensors for a specific and critical application – ophthalmic diagnostics. The suitability of $Ti_3C_2T_x$ for corneal lens-based applications, supporting previous work on intraocular lens devices and suggesting potential advancements in ophthalmic technologies. By enabling non-invasive diagnostics, materials like $Ti_3C_2T_x$ can significantly contribute to the understanding of diseases from their early stages to their resolution, allowing for personalised therapies.

6.3 Future work

These encouraging results pave the way for further advancements in the field, with the ultimate goal of developing a complete prototype incorporating a comprehensive powering and communication system. $Ti_3C_2T_x$ has already demonstrated its potential for energy storage and wireless communication in wearable devices. Using these capabilities, $Ti_3C_2T_x$ stands poised to become the primary material for the development of miniaturised systems, thereby enabling the creation of electrochemical sensors with wireless power and communication capabilities. However, to progress towards this goal, it is imperative to embark on a deeper investigation into the performance of the electrochemical sensor *in vitro*. This would involve developing a biological model of the anterior eye, in which the release of H_2O_2 by cells is chemically induced or naturally occurring, facilitating a more comprehensive understanding of the sensor's behaviour in realistic physiological conditions. Such in-depth investigations are essential for refining sensor design, optimizing performance, and ultimately realizing the full potential of $Ti_3C_2T_x$-based sensors in advancing diagnostic and monitoring capabilities in ophthalmic and other relevant fields.

7 Contribution and sources

7.1 Contributions and acknowledgements

The author acknowledges the assistance received during the thesis writing process. Specifically, she recognises the utilisation of language and form refinement through ChatGPT, the collaboration with co-authors in the creation of sections derived from published paper (Section 8) and the use of Adobe Illustrator for generating images. This serves to transparently disclose the sources of support and tools employed in developing the thesis.

7.2 References

1. Bandodkar AJ, Wang J. Non-invasive wearable electrochemical sensors: A review. Trends Biotechnol. 2014;32(7):363–71.

2. Li X, Huang Z, Shuck CE, Liang G, Gogotsi Y, Zhi C. MXene chemistry, electrochemistry and energy storage applications. Nat Rev Chem. 2022;6:389–404.

3. Cooksley G, Dymond MK, Stewart NA, Bucca G, Hesketh A, Lacey J, et al. Positive resolution of the wound-healing response in lens epithelial cells by $Ti_3C_2T_x$ MXene coatings for use in accommodative intraocular lens devices. 2D Mater. 2023;10(1).

4. Ward EJ, Lacey J, Crua C, Dymond MK, Maleski K, Hantanasirisakul K, et al. 2D Titanium Carbide ($Ti_3C_2T_x$) in Accommodating Intraocular Lens Design. Adv Funct Mater. 2020;2000841:1–9.

5. Cotlier E, Van Haeringen NJ. Clinical Biochemistry of Tears. Surv Ophthalmol. 1961;26(2).

6. Swamynathan SK, Wells A. Conjunctival goblet cells: Ocular surface functions, disorders that affect them, and the potential for their regeneration. Ocular Surface. 2020;18(1):19–26.

7. Gipson IK, Hori Y, Argüeso P. Character of Ocular Surface Mucins and Their Alteration in Dry Eye Disease. Ocul Surf. 2004;2(2).

8. Dartt DA, Willcox MDP. Complexity of the tear film: Importance in homeostasis and dysfunction during disease. Exp Eye Res. 2013;117:1–3.

9. Mishima S. Some Physiological Aspects of the Precorneal Tear Film [Internet]. Available from: http://archopht.jamanetwork.com/

10. Sorensen T, Taagehoj Jensen F. Tear flow in normal human eyes. Acta Ophthalmol. 1979;57(4):564–81.

11. Bylsma LM, Gračanin A, Vingerhoets AJJM. The neurobiology of human crying. Clin Auton Res. 2019;29(1):63–73.

12. Atkinson AJ, Colburn WA, DeGruttola VG, DeMets DL, Downing GJ, Hoth DF, et al. Biomarkers and surrogate endpoints: Preferred definitions and conceptual framework. Clin Pharmacol Ther. 2001;69(3):89–95.

13. Tseng RC, Chen CC, Hsu SM, Chuang HS. Contact-lens biosensors. Sensors (Switzerland). 2018;18(8).

14. Aass C, Norheim I, Eriksen EF, Thorsby PM, Pepaj M. Single unit filter-aided method for fast proteomic analysis of tear fluid. Anal Biochem. 2015;480:1–5.

15. Hagan S, Martin E, Enríquez-de-Salamanca A. Tear fluid biomarkers in ocular and systemic disease: Potential use for predictive, preventive and personalised medicine. EPMA Journal. 2016;7(1):1–20.

16. Pannebaker C, Chandler HL, Nichols JJ. Tear proteomics in keratoconus. Mol Vis. 2010;16:1949–57.

17. Kramann C, Boehm N, Lorenz K, Wehrwein N, Stoffelns BM, Pfeiffer N, et al. Effect of contact lenses on the protein composition in tear film: A ProteinChip study. Graefe's Archive for Clinical and Experimental Ophthalmology. 2011;249(2):233–43.

18. Xue ML, Willcox MDP, Lloyd A, Wakefield D, Thakur A. Regulatory role of IL-1β in the expression of IL-6 and IL-8 in human corneal epithelial cells during Pseudomonas aeruginosa colonization. Clin Exp Ophthalmol. 2001;29(3):171–4.

19. Xue mei L, Zhu H, Thakur A, Willcox M. 1α,25-dihydroxyvitamin D3 inhibits pro-inflammatory cytokine and chemokine expression in human corneal epithelial cells colonized with Pseudomonas aeruginosa. Immunol Cell Biol. 2002;80:340–5.

20. Cavet ME, Harrington KL, Vollmer TR, Ward KW, Zhang JZ. Anti-inflammatory and anti-oxidative effects of the green tea polyphenol epigallocatechin gallate in human corneal epithelial cells. Mol Vis. 2011;533–42.

21. Thakur A, Willcox MDP. Contact Lens Wear Alters the Production of Certain Inflammatory Mediators in Tears. Exp Eye Res. 2000;70:255–9.

22. Santacruz C, Linares M, Garfias Y, Loustaunau LM, Pavon L, Perez-Tapia SM, et al. Expression of IL-8, IL-6 and IL-1β in tears as a main characteristic of the immune response in human microbial keratitis. Int J Mol Sci. 2015;16(3):4850–64.

23. Thakur A, Willcox MDP. Cytokine and Lipid Inflammatory Mediator Profile of Human Tears During Contact Lens Associated Inflammatory Diseases. Eye Res. 1998;67:980480.

24. Rantamäki AH, Seppänen-Laakso T, Oresic M, Jauhiainen M, Holopainen JM. Human tear fluid lipidome: From composition to function. PLoS One. 2011;6(5):e19553.

25. Ma J, Shen Z, Peng R, Li C, Hu B, Hong J. Tear Lipid Metabolites As Potential Diagnostic Biomarkers for Ocular Chronic Graft-Versus-Host Disease. Transplant Cell Ther. 2021 Mar 1;27(3):232.e1-232.e6.

26. Robciuc A, Rantaḿaki AH, Jauhiainen M, Holopainen JM. Lipid-modifying enzymes in human tear fluid and corneal epithelial stress response. Invest Ophthalmol Vis Sci. 2014;55(1):16–24.

27. Ambaw YA, Timbadia DP, Raida M, Torta F, Wenk MR, Tong L. Profile of tear lipid mediator as a biomarker of inflammation for meibomian gland dysfunction and ocular surface diseases: Standard operating procedures. Ocular Surface. 2022;26:318–27.

28. Choi W, Lian C, Ying L, Kim GE, You IC, Park SH, et al. Expression of Lipid Peroxidation Markers in the Tear Film and Ocular Surface of Patients with Non-Sjogren

Syndrome: Potential Biomarkers for Dry Eye Disease. Curr Eye Res. 2016;41(9):1143–9.

29. Stahl U, Willcox M, Stapleton F. Osmolality and tear film dynamics. Clin Exp Optom. 2012;95(1):3–11.

30. Tan SZ, Begley P, Mullard G, Hollywood KA, Bishop PN. Introduction to metabolomics and its applications in ophthalmology. Eye. 2016;30(6):773–83.

31. Rossi C, Cicalini I, Cufaro MC, Agnifili L, Mastropasqua L, Lanuti P, et al. Multi-omics approach for studying tears in treatment-naïve glaucoma patients. Int J Mol Sci. 2019;20(16):4029.

32. Roedl JB, Bleich S, Reulbach U, Rejdak R, Kornhuber J, Kruse FE, et al. Homocysteine in Tear Fluid of Patients With Pseudoexfoliation Glaucoma. J Glaucoma. 2007;16(2):234–9.

33. Kim AR, Nodel MR, Pavlenko TA, Chesnokova NB, Yakhno NN, Ugrumov M V. Tear fluid catecholamines as biomarkers of the parkinson's disease: A clinical and experimental study. Acta Naturae. 2019;11(4):99–103.

34. Urbanski G, Assad S, Chabrun F, Chao de la Barca JM, Blanchet O, Simard G, et al. Tear metabolomics highlights new potential biomarkers for differentiating between Sjögren's syndrome and other causes of dry eye. Ocular Surface. 2021;22:110–6.

35. Karamichos D, Zieske JD, Sejersen H, Sarker-Nag A, Asara JM, Hjortdal J. Tear metabolite changes in keratoconus. Exp Eye Res. 2015;132:1–8.

36. Lane JD, Krumholz DM, Sack RA, Morris C. Tear glucose dynamics in diabetes mellitus. Curr Eye Res. 2006;31(11):895–901.

37. Rentka A, Koroskenyi K, Harsfalvi J, Szekanecz Z, Szucs G, Szodoray P, et al. Evaluation of commonly used tear sampling methods and their relevance in subsequent biochemical analysis. Ann Clin Biochem. 2017 Sep 1;54(5):521–9.

38. Bron AJ. Diagnosis of Dry Eye. Surv Ophthalmol. 2001;45(2):221-226.

39. Guyette N, Williams L, Tran MT, Than T, Bradley J, Kehinde L, et al. Comparison of low-abundance biomarker levels in capillary-collected nonstimulated tears and washout tears of aqueous-deficient and normal patients. Invest Ophthalmol Vis Sci. 2013;54(5):3729–37.

40. Xu J, Tao X, Liu X, Yang L. Wearable Eye Patch Biosensor for Noninvasive and Simultaneous Detection of Multiple Biomarkers in Human Tears. Anal Chem. 2022;94(24):8659–67.

41. Spurr-Michaud S, Argüeso P, Gipson I. Assay of mucins in human tear fluid. Exp Eye Res. 2007;84(5):939–50.

42. Rohit A, Stapleton F, Brown SHJ, Mitchell TW, Willcox MDP. Comparison of Tear Lipid Profile among Basal, Reflex, and Flush Tear Samples. Optom Vis Sci. 2014;91(12):1391-5.

43. Fullard RJ, Snyderj C. Protein Levels in Nonstimulated and Stimulated Tears of Normal Human Subjects. Invest Ophthalmol Vis Sci. 1990;31(6):1119-26.

44. Pieczyński J, Szulc U, Harazna J, Szulc A, Kiewisz J. Tear fluid collection methods: Review of current techniques. Eur J Ophthalmol. 2021;31(5):2245–51.

45. Hui J, Quah M, Tong L, Barbier S. Patient Acceptability of Tear Collection in the Primary Healthcare Setting. Optom Vis Sci. 2014;19(4):452–8.

46. Badugu, Ramachandram; Jeng, Bennie H.; Reece, E. Albert; Lakowicz JR. Contact lens to measure individual ion concentration in tears and application to dry eye disease. Anal Biochem. 2018;542:84–94.

47. Moreddu R, Wolffsohn JS, Vigolo D, Yetisen AK. Laser-inscribed contact lens sensors for the detection of analytes in the tear fluid. Sens Actuators B Chem. 2020;317:128183.

48. Kett WG. A Brief History Of Contact Lenses. Aust J Optom. 1960;360–2.

49. Musgrave CSA, Fang F. Contact lens materials: A materials science perspective. Materials. 2019;12(2):261.

50. Moreddu R, Vigolo D, Yetisen AK. Contact Lens Technology: From Fundamentals to Applications. Adv Healthc Mater. 2019;8(15):1–24.

51. Fink JK. Contact Lenses: Materials, Chemicals and Applications. 1st ed. Beverly: Scrivener Publishing; 2022.

52. Yang X, Yao H, Zhao G, Ameer GA, Sun W, Yang J, et al. Flexible, wearable microfluidic contact lens with capillary networks for tear diagnostics. J Mater Sci. 2020 Aug 1;55(22):9551–61.

53. Moreddu R, Elsherif M, Adams H, Moschou D, Cordeiro MF, Wolffsohn JS, et al. Integration of paper microfluidic sensors into contact lenses for tear fluid analysis. Lab Chip. 2020;20(21):3970–9.

54. Ku M, Kim J, Won JE, Kang W, Park YG, Park J, et al. Smart, soft contact lens for wireless immunosensing of cortisol. Sci Adv. 2020;6(eabb2891).

55. Jiang N, Montelongo Y, Butt H, Yetisen AK. Microfluidic Contact Lenses. Small. 2018;14(15):1704363.

56. Badugu R, Reece EA, Lakowicz JR. Glucose-sensitive silicone hydrogel contact lens toward tear glucose monitoring toward tear glucose monitoring. J Biomed Opt. 2018;23(5):1-9.

57. March W, Lazzaro D, Rastogi S. Fluorescent Measurement in the Non-Invasive Contact Lens Glucose Sensor. Diabetes Technology and Therapeutics (Symposium Paper). 2006;8(3):312–7.

58. March WF, Mueller A, Herbrechtsmeier P. Clinical Trial of a Noninvasive Contact Lens Glucose Sensor. Diabetes Technol Ther. 2004;6(6):782-9.

59. Deng M, Song G, Zhong K, Wang Z, Xia X, Tian Y. Wearable fluorescent contact lenses for monitoring glucose via a smartphone. Sens Actuators B Chem. 2022;352:131067.

60. Elsherif M, Moreddu R, Alam F, Salih AE, Ahmed I, Butt H. Wearable Smart Contact Lenses for Continual Glucose Monitoring: A Review. Front Med (Lausanne). 2022;9:858784.

61. Hernández-Rodríguez JF, Rojas D, Escarpa A. Electrochemical Sensing Directions for Next-Generation Healthcare: Trends, Challenges, and Frontiers. Anal Chem. 2021;93(1):167–83.

62. Yu Y, Nyein HYY, Gao W, Javey A. Flexible Electrochemical Bioelectronics: The Rise of In Situ Bioanalysis. Advanced Materials. 2020;32(15):1902083.

63. Noviana E, Mccord CP, Clark KM, Jang I, Henry CS. Electrochemical Paper-Based Devices: Sensing Approaches and Progress Toward Practical Applications. Lab Chip. 2020;(1):9–34.

64. Karimi-Maleh H, Karimi F, Alizadeh M, Sanati AL. Electrochemical Sensors, a Bright Future in the Fabrication of Portable Kits in Analytical Systems. Chem Rec 2020;20(7):682-692.

65. Wang J. Analytical Electrochemistry, Third Edition. 3rd Edition. Analytical Electrochemistry, Third Edition. Wiley-VCH; 2006. pp. 1–250.

66. Bard AJ, Faulkner LR. Electrochemical methods - Fundamentals and applications. 2nd ed. John Wiley & Sons, Inc. 2001. pp. 457–465.

67. Patel BA. Electrochemical Biosensors, Chapter 12: Electrochemical Biosensors. Electrochemistry for Bioanalysis. 1st Edition. Elsevier; 2021.

68. Forster RJ. Microelectrodes: New Dimensions in Electrochemistry. Chem Society Rev. 1994:4:289

69. McCreery RL. Advanced carbon electrode materials for molecular electrochemistry. Chem Rev. 2008;108(7):2646–87.

70. Chen P, McCreery RL. Control of Electron Transfer Kinetics at Glassy Carbon Electrodes by Specific Surface Modification. Anal Chem. 1996;68(22):3958–65.

71. Kneten KR, McCreery RL. Effects of Redox System Structure on Electron-Transfer Kinetics at Ordered Graphite and Glassy Carbon Electrodes. Anal Chem. 1992;64(21):2518–24.

72. Cirocka A, Zarzeczańska D, Wcisło A. Good choice of electrode material as the key to creating electrochemical sensors-characteristics of carbon materials and transparent conductive oxides (TCO). Materials. 2021;14(16).

73. Bi H, Li Y, Liu S, Guo P, Wei Z, Lv C, et al. Carbon-nanotube-modified glassy carbon electrode for simultaneous determination of dopamine, ascorbic acid and uric acid: The effect of functional groups. Sens Actuators B Chem. 2012;171–172:1132–40.

74. Roberts JG, Moody BP, McCarty GS, Sombers LA. Specific oxygen-containing functional groups on the carbon surface underlie an enhanced sensitivity to dopamine at electrochemically pretreated carbon fiber microelectrodes. Langmuir. 2010;26(11):9116–22.

75. Mahbubur Rahman M, Liu D, Siraj Lopa N, Baek JB, Nam CH, Lee JJ. Effect of the carboxyl functional group at the edges of graphene on the signal sensitivity of dopamine detection. Journal of Electroanalytical Chemistry. 2021;898:115628.

76. Swinya DL, Martín-Yerga D, Walker M, Unwin PR. Surface Nanostructure Effects on Dopamine Adsorption and Electrochemistry on Glassy Carbon Electrodes. Journal of Physical Chemistry C. 2022;126(31):13399–408.

77. Wang S, Zhang T, Zhu X, Zu S, Xie Z, Lu X, et al. Metal–Organic Frameworks for Electrocatalytic Sensing of Hydrogen Peroxide. Molecules. 2022;27(14):4571.

78. Terzi F, Pigani L, Zanardi C. Unusual metals as electrode materials for electrochemical sensors. Curr Opin Electrochem. 2019;16:157–63.

79. Chimene D, Alge DL, Gaharwar AK. Two-Dimensional Nanomaterials for Biomedical Applications: Emerging Trends and Future Prospects. Adv Mater. 2015;27(45):7261–84.

80. Si P, Huang Y, Wang T, Ma J. Nanomaterials for electrochemical non-enzymatic glucose biosensors. RSC Adv. 2013;3(11):3487–502.

81. Randviir EP, Brownson DAC, Metters JP, Kadara RO, Banks CE. The fabrication, characterisation and electrochemical investigation of screen-printed graphene electrodes. Physical Chemistry Chemical Physics. 2014;16(10):4598–611.

82. Randviir EP, Brownson DAC, Gómez-Mingot M, Kampouris DK, Iniesta J, Banks CE. Electrochemistry of Q-Graphene. Nanoscale. 2012;4(20):6470–80.

83. Nagel B, Dellweg H, Gierasch LM. Glossary for chemists of terms used in biotechnology. Pure and Applied Chemistry. 1992;64(1):143–68.

84. Karunakaran C, Rajkumar R, Bhargava K. Introduction to Biosensors. In: Biosensors and Bioelectronics. Elsevier Inc.; 2015. p. 1–68.

85. Mohr Said, N. A. 2014. Electrochemical biosensor based on microfabricated electrode arrays for life sciences applications. PhD Thesis, University College Cork. Available at https://hdl.handle.net/10468/1759

86. Malhotra BD, Ali A. Nanomaterials in Biosensors: Fundamentals and Applications. Elsevier; 2018.

87. Marrazza G. Piezoelectric biosensors for organophosphate and carbamate pesticides: A review. Biosensors (Basel). 2014;4(3):301–17.

88. Dai J, Ogbeide O, Macadam N, Sun Q, Yu W, Li Y, et al. Printed gas sensors. Chem Soc Rev. 2020;49(6):1756–89.

89. Kaushik A, Mujawar MA. Point of care sensing devices: Better care for everyone. Sensors (Switzerland). 2018;18(12):10–3.

90. Darwish A, Ismail Sayed G, Ella Hassanien A. Intelligent Pervasive Computing Systems for Smarter Healthcare. Chapter 3: The Impact of Implantable Sensors in Biomedical Technology on the Future of Healthcare Systems. Wiley Online library 2019.

91. Corrie SR, Coffey JW, Islam J, Markey KA, Kendall MAF. Blood, sweat, and tears: Developing clinically relevant protein biosensors for integrated body fluid analysis. Anal. 2015;140(13):4350–64.

92. Park GS, Ku K, Baek SH, Kim SJ, Kim S Il, Kim BT, et al. Development of Reverse Transcription Loop-Mediated Isothermal Amplification Assays Targeting SARS-CoV-2. The Journal of Molecular Diagnostics. 2020;22(6):729–35.

93. Chu DKW, Pan Y, Cheng SMS, Hui KPY, Krishnan P, Liu Y, et al. Molecular Diagnosis of a Novel Coronavirus (2019-nCoV) Causing an Outbreak of Pneumonia. Clin Chem. 2020;7:1–7.

94. Seo G, Lee G, Kim MJ, Baek SH, Choi M, Ku KB, et al. Rapid Detection of COVID-19 Causative Virus (SARS-CoV-2) in Human Nasopharyngeal Swab Specimens Using Field-Effect Transistor-Based Biosensor. ACS Nano. 2020;14(9):12257–8.

95. Napi MLM, Sultan SM, Ismail R, How KW, Ahmad MK. Electrochemical-based biosensors on different zinc oxide nanostructures: A review. Materials. 2019;12(18):1–34.

96. Feigel IM, Vedala H, Star A. Biosensors based on one-dimensional nanostructures. J Mater Chem. 2011;21(25):8940–54.

97. Zhan H, Guo D, Xie GX. Two-dimensional layered materials: From mechanical and coupling properties towards applications in electronics. Nanoscale. 2019;11(28):13181–212.

98. Ganesan S, Ramajayam K, Kokulnathan T, Palaniappan A. Recent Advances in Two-Dimensional MXene-Based Electrochemical Biosensors for Sweat Analysis. Molecules. 202;28(12):4617.

99. Justino CIL, Gomes AR, Freitas AC, Duarte AC, Rocha-Santos TAP. Graphene based sensors and biosensors. TrAC - Trends in Analytical Chemistry. 2017;91:53–66.

100. Sabu C, Henna TK, Raphey VR, Nivitha KP, Pramod K. Advanced biosensors for glucose and insulin. Biosens Bioelectron. 2019;141:111201.

101. Yoo EH, Lee SY. Glucose biosensors: An overview of use in clinical practice. Sensors. 2010;10(5):4558–76.

102. Kim J, Kim M, Lee MS, Kim K, Ji S, Kim YT, et al. Wearable smart sensor systems integrated on soft contact lenses for wireless ocular diagnostics. Nat Commun. 2017;8:14997.

103. Mitsubayashi K, Dicks JM, Yokoyama K, Takeuchi T, Tamiya E, Karube I. A flexible biosensor for glucose. Electroanalysis. 1995;7(1):83–7.

104. Mitsubayashi K, Wakabayashi Y, Tanimoto S, Murotomi D, Endo T. Optical-transparent and flexible glucose sensor with ITO electrode. Biosens Bioelectron. 2003;19(1):67–71.

105. Ali AH, Shuhaimi A, Hassan Z. Structural, optical and electrical characterization of ITO, ITO/Ag and ITO/Ni transparent conductive electrodes. Appl Surf Sci. 2014;288:599–603.

106. Chu MX, Miyajima K, Takahashi D, Arakawa T, Sano K, Sawada SI, et al. Soft contact lens biosensor for in situ monitoring of tear glucose as non-invasive blood sugar assessment. Talanta. 2011;83(3):960–5.

107. Yao H, Shum AJ, Cowan M, Lähdesmäki I, Parviz BA. A contact lens with embedded sensor for monitoring tear glucose level. Biosens Bioelectron. 2011;26(7):3290–6.

108. Keum DH, Kim SK, Koo J, Lee GH, Jeon C, Mok JW, et al. Wireless smart contact lens for diabetic diagnosis and therapy. Sci Adv. 2020;6(17):1–13.

109. Kaisti M. Detection principles of biological and chemical FET sensors. Biosens Bioelectron. 2017;98:437–48.

110. Senior M. Novartis signs up for Google smart lens. Nat Biotechnol. 2014;32(9):856.

111. Otis B. Update on our Smart Lens program with Alcon. 2018. Available: https://verily.com/perspectives/update-on-our-smart-lens-program-with-alcon. Accessed Jan 2024.

112. Thomas N, Lähdesmäki I, Parviz BA. A contact lens with an integrated lactate sensor. Sens Actuators B Chem. 2012;162(1):128–34.

113. Jang J, Kim J, Shin H, Park YG, Jun Joo B, Seo H, et al. Smart contact lens and transparent heat patch for remote monitoring and therapy of chronic ocular surface inflammation using mobiles. Sci Adv. 2021;7:7194–225.

114. Liu Z, Wang G, Ye C, Sun H, Pei W, Wei C, et al. An Ultrasensitive Contact Lens Sensor Based On Self-Assembly Graphene For Continuous Intraocular Pressure Monitoring. Adv Funct Mater. 2021;31(29):2010991.

115. Yin R, Xu Z, Mei M, Chen Z, Wang K, Liu Y, et al. Soft transparent graphene contact lens electrodes for conformal full-cornea recording of electroretinogram. Nat Commun. 2018;9(1):2334.

116. Michael Naguib, Murat Kurtoglu, Volker Presser, Jun Lu, Junjie Niu, Min Heon, et al. Two-Dimensional Nanocrystals Produced by Exfoliation of Ti_3AlC_2. Adv Mater. 2011;23:4248–4253.

117. Deysher G, Shuck CE, Hantanasirisakul K, Frey NC, Foucher AC, Maleski K, Sarycheva A, Shenoy VB, Stach EA, Anasori B, Gogotsi Y. Synthesis of Mo_4VAlC_4 MAX Phase and Two-Dimensional Mo_4VC_4 MXene with Five Atomic Layers of Transition Metals, ACS Nano 2020;14(1): 204–217.

118. Hantanasirisakul K, Gogotsi Y. Electronic and Optical Properties of 2D Transition Metal Carbides and Nitrides (MXenes). Advanced Materials. 2018;30(52):1804779.

119. Anasori B, Lukatskaya MR, Gogotsi Y. 2D metal carbides and nitrides (MXenes) for energy storage. Nat Rev Mater. 2017;2:16098.

120. Hantanasirisakul K, Zhao MQ, Urbankowski P, Halim J, Anasori B, Kota S, et al. Fabrication of $Ti_3C_2T_x$ MXene Transparent Thin Films with Tunable Optoelectronic Properties. Adv Electron Mater. 2016;2(6):1–7.

121. Hart JL, Hantanasirisakul K, Lang AC, Anasori B, Pinto D, Pivak Y, et al. Control of MXenes' electronic properties through termination and intercalation. Nat Commun. 2019;10(1):522.

122. Kumar H, Frey NC, Dong L, Anasori B, Gogotsi Y, Shenoy VB. Tunable Magnetism and Transport Properties in Nitride MXenes. ACS Nano. 2017;11(8):7648–55.

123. Anasori B, Gogotsi Y. MXenes: trends, growth, and future directions. Graphene and 2D Materials. 2022;7(3–4):75–9.

124. Mathis T, Maleski K, Goad A, Sarycheva A, Anayee M, Foucher AC, et al. Modified MAX Phase Synthesis for Environmentally Stable and Highly Conductive Ti_3C_2 MXene. ACS Nano. 2020;15(4):6420–6429.

126. Sarycheva A, Polemi A, Liu Y, Dandekar K, Anasori B, Gogotsi Y. 2D titanium carbide (MXene) for wireless communication. Sci Adv. 2018;4(9):1–9.

127. Khorsand Kazemi K, Hosseini E, Hu S, Narang R, Li S, Arjmand M, et al. MXene membrane in planar microwave resonant structures for 5G applications. Appl Mater Today. 2022;26:101294.

128. Shahzad F, Alhabeb M, Hatter CB, Anasori B, Hong SM, Koo CM, Gogotsi Y. Electromagnetic interference shielding with 2D transition metal carbides (MXenes), Science 2016;353(6304):1137-1140.

129. Han M, Shuck CE, Rakhmanov R, Parchment D, Anasori B, Koo CM, et al. Beyond $Ti_3C_2T_x$ - MXenes for electromagnetic interference shielding. ACS Nano. 2020;14:5008–16.

130. Liu Z, Alshareef HN. MXenes for Optoelectronic Devices. Adv Electron Mater. 2021;7(9):2100295.

131. Maleski K, Shuck CE, Fafarman AT, Gogotsi Y. The Broad Chromatic Range of Two-Dimensional Transition Metal Carbides. Adv Opt Mater. 2020;9:2001563.

132. Mauchamp V, Bugnet M, Bellido EP, Botton GA, Moreau P, Magne D, et al. Enhanced and tunable surface plasmons in two-dimensional Ti_3C_2 stacks: Electronic structure versus boundary effects. Phys Rev B Condens Matter Mater Phys. 2014;89(23):1–6.

133. El-Demellawi JK, Lopatin S, Yin J, Mohammed OF, Alshareef HN. Tunable Multipolar Surface Plasmons in 2D $Ti_3C_2T_x$ MXene Flakes. ACS Nano. 2018;12(8):8485–93.

134. Salles P, Quain E, Kurra N, Sarycheva A, Gogotsi Y. Automated Scalpel Patterning of Solution Processed Thin Films for Fabrication of Transparent MXene Microsupercapacitors. Small. 2018;14(44):1–7.

135. Salles P, Pinto D, Hantanasirisakul K, Maleski K, Shuck CE, Gogotsi Y. Electrochromic Effect in Titanium Carbide MXene Thin Films Produced by Dip-Coating. Adv Funct Mater. 2019;29(17):1–9.

136. Ahn S, Han TH, Maleski K, Song J, Kim YH, Park MH, et al. A 2D Titanium Carbide MXene Flexible Electrode for High-Efficiency Light-Emitting Diodes. Advanced Materials. 2020;32:202000919.

137. Anasori B, Gogotsi Y. 2D Metal Carbides and Nitrides (MXenes) - Structure, Properties and Applications. Springer. 2019.

138. Lukatskaya MR, Bak SM, Yu X, Yang XQ, Barsoum MW, Gogotsi Y. Probing the mechanism of high capacitance in 2D titanium carbide in Situ X-ray absorption spectroscopy. Adv Energy Mater. 2015;5:1500589.

139. Inman A, Šedajová V, Matthews K, Gravlin J, Busa J, Shuck CE, et al. Shear delamination of multilayer MXenes. JMR. 2022;37(22):1–11.

140. Levitt A, Zhang J, Dion G, Gogotsi Y, Razal JM. MXene-Based Fibers, Yarns, and Fabrics for Wearable Energy Storage Devices. Adv Funct Mater. 2020;30(47):202000739.

141. Morales-garc A, Calle-vallejo F, Illas F. MXenes: New Horizons in Catalysis. ACS Catal. 2020;10(22):13487-13503.

142. Seh ZW, Fredrickson KD, Anasori B, Kibsgaard J, Strickler AL, Lukatskaya MR, et al. Two-Dimensional Molybdenum Carbide (MXene) as an Efficient Electrocatalyst for Hydrogen Evolution. ACS Energy Letters. 2016;1(3):589–94.

143. Liu H, Duan C, Yang C, Shen W, Wang F, Zhu Z. A novel nitrite biosensor based on the direct electrochemistry of hemoglobin immobilized on MXene-Ti_3C_2. Sens Actuators B Chem. 2015;218:60–6.

144. Amara U, Sarfraz B, Mahmood K, Mehran MT, Muhammad N, Hayat A, et al. Fabrication of ionic liquid stabilized MXene interface for electrochemical dopamine detection. Microchimica Acta. 2022;189(2):64.

145. Rakhi RB, Nayuk P, Xia C, Alshareef HN. Novel amperometric glucose biosensor based on MXene nanocomposite. Sci Rep. 2016;6:36422.

146. Lorencova L, Bertok T, Filip J, Jerigova M, Velic D, Kasak P, et al. Highly stable $Ti_3C_2T_x$ (MXene)/Pt nanoparticles-modified glassy carbon electrode for H_2O_2 and small molecules sensing applications. Sens Actuators B Chem. 2018;263:360–8.

147. Kalambate PK, Gadhari NS, Li X, Rao Z, Navale ST, Shen Y, et al. Recent advances in MXene–based electrochemical sensors and biosensors. Trends in Analytical Chemistry. 2019;120:115643.

148. Jastrzębska AM, Szuplewska A, Wojciechowski T, Chudy M, Ziemkowska W, Chlubny L, et al. In vitro studies on cytotoxicity of delaminated $Ti_3C_2T_x$ MXene. J Hazard Mater. 2017;339:1–8.

149. Rozmysłowska-Wojciechowska A, Szuplewska A, Wojciechowski T, Poźniak S, Mitrzak J, Chudy M, et al. A simple, low-cost and green method for controlling the cytotoxicity of MXenes. Mater Sci Eng C. 2020;111:110790.

150. Feng W, Wang R, Zhou Y, Ding L, Gao X, Zhou B, et al. Ultrathin Molybdenum Carbide MXene with Fast Biodegradability for Highly Efficient Theory-Oriented Photonic Tumor Hyperthermia. Adv Funct Mater. 2019;29(22):1–15.

151. Lin H, Gao S, Dai C, Chen Y, Shi J. A Two-Dimensional Biodegradable Niobium Carbide (MXene) for Photothermal Tumor Eradication in NIR-I and NIR-II Biowindows. J Am Chem Soc. 2017;139(45):16235–47.

152. Lin H, Wang Y, Gao S, Chen Y, Shi J. Theranostic 2D Tantalum Carbide (MXene). Adv Mater. 2017;30(4):1703284.

153. Driscoll N, Richardson AG, Maleski K, Anasori B, Adewole O, Lelyukh P, et al. Two-Dimensional Ti_3C_2 MXene for High-Resolution Neural Interfaces. ACS Nano. 2018;12:10419–29.

154. Lin H, Chen Y, Shi J. Insights into 2D MXenes for Versatile Biomedical Applications: Current Advances and Challenges Ahead. Advanced Science. 2018;5(10).

155. Liu G, Zou J, Tang Q, Yang X, Zhang Y, Zhang Q, et al. Surface Modified Ti_3C_2 MXene Nanosheets for Tumor Targeting Photothermal/Photodynamic/Chemo Synergistic Therapy. ACS Appl Mater Interfaces. 2017;9(46):40077–86.

156. Xu C, Wang L, Liu Z, Chen L, Guo J, Kang N, et al. Large-area high-quality 2D ultrathin Mo2C superconducting crystals. Nat Mater. 2015;14(11):1135–41.

157. Cai X, Xu Y, Liu M, Yang J. Growth kinetics and mechanical properties of the V_2C and V_8C_7 carbide layers on iron substrate. Surf Coat Technol. 2020;382:125148.

158. Fan Y, Li L, Zhang Y, Zhang X, Geng D, Hu W. Recent Advances in Growth of Transition Metal Carbides and Nitrides (MXenes) Crystals. Adv Funct Mater. 2022;32(16):2111357.

159. Garrick Lim KR, Shekhirev M, C. WyattB, Anasori B, Gogotsi Y, Wei Seh Z. Fundamentals of MXene synthesis. Nature Synthesis. 2022;1:601–14.

160. Khaledialidusti R, Khazaei M, Khazaei S, Ohno K. High-throughput computational discovery of ternary-layered MAX phases and prediction of their exfoliation for formation of 2D MXenes. Nanoscale. 2021;13(15):7294–307.

161. Zhang J, Kong N, Uzun S, Levitt A, Seyedin S, Lynch PA, et al. Scalable Manufacturing of Free-Standing, Strong $Ti_3C_2T_x$ MXene Films with Outstanding Conductivity. Advanced Materials. 2020;32(23):e2001093.

162. Sang X, Xie Y, Lin MW, Alhabeb M, Van Aken KL, Gogotsi Y, et al. Atomic defects in monolayer titanium carbide ($Ti_3C_2T_x$) MXene. ACS Nano. 2016;10(10):9193–200.

163. Zhang CJ, Anasori B, Seral-Ascaso A, Park SH, McEvoy N, Shmeliov A, et al. Transparent, Flexible, and Conductive 2D Titanium Carbide (MXene) Films with High Volumetric Capacitance. Adv Mater. 2017;29(36):1–9.

164. Hantansirisakul K, Zhao M, Urbankowski P, Halim J, Anasori B, Kota S, et al. Fabrication of $Ti_3C_2T_x$ MXene Transparent Thin Films with Tunable Optoelectronic Properties. Adv Electron Mater. 2016;2(6):1600050.

165. Xu S, Dall'Agnese Y, Wei G, Zhang C, Gogotsi Y, Han W. Screen-printable microscale hybrid device based on MXene and layered double hydroxide electrodes for powering force sensors. Nano Energy. 2018;50:479–88.

166. Driscoll N, Maleski K, Richardson AG, Murphy B, Anasori B, Lucas TH, et al. Fabrication of $Ti_3C_2T_x$ MXene microelectrode arrays for in vivo neural recording. JoVE. 2020; (156):1–9.

167. Orangi J, Hamade F, Davis VA, Beidaghi M. 3D Printing of Additive-Free 2D $Ti_3C_2T_x$ (MXene) Ink for Fabrication of Micro-Supercapacitors with Ultra-High Energy Densities. ACS Nano. 2020;14(1):640–50.

168. Yang W, Yang J, Byun JJ, Moissinac FP, Xu J, Haigh SJ, et al. 3D Printing of Freestanding MXene Architectures for Current-Collector-Free Supercapacitors. Adv Mater. 2019;31(37).

169. Song D, Li X, Li XP, Jia X, Min P, Yu ZZ. Hollow-structured MXene-PDMS composites as flexible, wearable and highly bendable sensors with wide working range. J Colloid Interface Sci. 2019;555:751–8.

170. Akuzum B, Maleski K, Anasori B, Lelyukh P, Alvarez NJ, Kumbur EC, et al. Rheological Characteristics of 2D Titanium Carbide (MXene) Dispersions: A Guide for Processing MXenes. ACS Nano. 2018;12(3):2685–94.

171. Maleski K, Mochalin VN, Gogotsi Y. Dispersions of Two-Dimensional Titanium Carbide MXene in Organic Solvents. Chemistry of Materials. 2017;29(4):1632–40.

172. Zhang J, Uzun S, Seyedin S, Lynch PA, Akuzum B, Wang Z, et al. Additive-Free MXene Liquid Crystals and Fibers. ACS Cent Sci. 2020;6(2):254-265.

173. Shuck CE, Gogotsi Y. Taking MXenes from the lab to commercial products. Chem Eng Journ. 2020;401:125786.

174. Shuck CE, Sarycheva A, Anayee M, Levitt A, Zhu Y, Uzun S, et al. Scalable Synthesis of $Ti_3C_2T_x$ MXene. Adv Eng Mater. 2020;22(3):1–8.

175. Uzun S, Seyedin S, Stoltzfus AL, Levitt AS, Alhabeb M, Anayee M, et al. Knittable and Washable Multifunctional MXene-Coated Cellulose Yarns. Adv Funct Mater. 2019;29(45):1905015.

176. Mashtalir O, Naguib M, Mochalin VN, Dall'Agnese Y, Heon M, Barsoum MW, et al. Intercalation and delamination of layered carbides and carbonitrides. Nat Commun. 2013;4:1–7.

177. Shekhirev M, Shuck CE, Sarycheva A, Gogotsi Y. Characterization of MXenes at every step, from their precursors to single flakes and assembled films. Prog Mater Sci. 2021;120:100757.

178. El-Demellawi JK, Lopatin S, Yin J, Mohammed OF, Alshareef HN. Tunable Multipolar Surface Plasmons in 2D $Ti_3C_2T_x$ MXene Flakes. ACS Nano. 2018;12(8):8485–93.

179. Maleski K, Ren CE, Zhao MQ, Anasori B, Gogotsi Y. Size-Dependent Physical and Electrochemical Properties of Two-Dimensional MXene Flakes. ACS Appl Mater Interfaces. 2018;10(29):24491–8.

180. Alhabeb M, Maleski K, Anasori B, Lelyukh P, Clark L, Sin S, et al. Guidelines for synthesis and processing of two-dimensional titanium carbide ($Ti_3C_2T_x$ MXene). Chemistry of Materials. 2017;29:7633–44.

181. Sakho EHM, Allahyari E, Oluwafemi OS, Thomas S, Kalarikkal N. Dynamic Light Scattering (DLS). Thermal and Rheological Measurement Techniques for Nanomaterials Characterization. 2017;3:37–49.

182. Santos MH, Lodeiro C, Capelo-Martinez JL. Ultrasound in Chemistry: Analytical Applications. Ultrasound in Chemistry: Analytical Applications. 2009;1–157.

183. Mohammadi AV, Rosen J, Gogotsi Y. The world of two-dimensional carbides and nitrides (MXenes). Science. 2021;372:1165.

184. Levitt A, Zhang J, Dion G, Gogotsi Y, Razal JM. MXene-Based Fibers, Yarns, and Fabrics for Wearable Energy Storage Devices. Adv Funct Mater. 2020;30(47):202000739.

185. Qin L, Jiang J, Hou L, Zhang F, Rosen J. MXene-based multifunctional smart fibers for wearable and portable electronics. J Mater Chem A Mater. 2022;10(23):12544–50.

186. Gogotsi Y. The Future of MXenes. Chem Mater. 2023;35(21):8767–70.

187. Zhang D, Yu L, Wang D, Yang Y, Mi Q, Zhang J. Multifunctional latex/ polytetrafluoroethylene-based triboelectric nanogenerator for self-powered organ-like mxene/metal-organic framework-derived CuO nanohybrid ammonia sensor. ACS Nano. 2021;15(2):2911–9.

188. Yin A, Zhang C, Luo J, Liu J, Ren Z, Wang Y, et al. A highly sensitive and miniaturized wearable antenna based on MXene films for strain sensing. Mater Adv. 2022;4(3):917–22.

189. Wang Y, Zhao P, Gao B, Yuan M, Yu J, Wang Z, et al. Self-reduction of bimetallic nanoparticles on flexible MXene-graphene electrodes for simultaneous detection of ascorbic acid, dopamine, and uric acid. Microchem J. 2023;185:108177.

190. Ankitha M, Shabana N, Vaishag P V., Rasheed PA. A novel flexible electrode with highly stable trifluoroacetic acid modified Nb_2CT_x MXene for the sensitive detection of rifampicin. JEAC. 2023;928:117088.

191. Li XP, Li Y, Li X, Song D, Min P, Hu C, et al. Highly sensitive, reliable and flexible piezoresistive pressure sensors featuring polyurethane sponge coated with MXene sheets. J Colloid Interface Sci. 2019;542:54–62.

192. Kumar S, Kang D, Nguyen VH, Nasir N, Hong H, Kim M, et al. Application of Titanium-Carbide MXene-Based Transparent Conducting Electrodes in Flexible Smart Windows. ACS Appl Mater Interfaces. 2021;13(34):40976–85.

193. Wang D, Zhang D, Tang M, Zhang H, Chen F, Wang T, et al. Rotating triboelectric-electromagnetic nanogenerator driven by tires for self-powered MXene-based flexible wearable electronics. J Chem Eng. 2022;446:136914.

194. Zhang H, Zhang D, Wang Z, Xi G, Mao R, Ma Y, et al. Ultrastretchable, Self-Healing Conductive Hydrogel-Based Triboelectric Nanogenerators for Human-Computer Interaction. ACS Appl Mater Interfaces. 2023;15(4):5128–38.

195. Zhang H, Zhang D, Zhang B, Wang D, Tang M. Wearable Pressure Sensor Array with Layer-by-Layer Assembled MXene Nanosheets/Ag Nanoflowers for Motion Monitoring and Human-Machine Interfaces. ACS Appl Mater Interfaces. 2022;14(43):48907–16.

196. Li X, Huang Z, Shuck CE, Liang G, Gogotsi Y, Zhi C. MXene chemistry, electrochemistry and energy storage applications. Nat Rev Chem. 2022;6:389–404.

197. Inman A, Hryhorchuk T, Bi L, Wang R, Greenspan B, Tabb T, et al. Wearable energy storage with MXene textile supercapacitors for real world use. J Mater Chem. 2023;11(7):3514–23.

198. Zhang C (John), Nicolosi V. Graphene and MXene-based transparent conductive electrodes and supercapacitors. Energy Storage Mater. 2019;16:102–25.

199. Park J, Hwang JC, Kim GG, Park JU. Flexible electronics based on one-dimensional and two-dimensional hybrid nanomaterials. InfoMat. 2020;2(1):33–56.

200. Sinha A, Dhanjai, Stavrakis AK, Stojanovic CM. Textile-based electrochemical sensors and their applications. Talanta. 2022;244:123425.

201. Yuan F, Xia Y, Lu Q, Xu Q, Shu Y, Hu X. Recent advances in inorganic functional nanomaterials based flexible electrochemical sensors. Talanta. 2022;244:123419.

202. Gao F, Liu C, Zhang L, Liu T, Wang Z, Song Z, et al. Wearable and flexible electrochemical sensors for sweat analysis: a review. Microsyst Nanoeng. 2023;9(1):1–21.

203. Zhu X, Liu W, Shuang S, Nair M, Li CZ. Intelligent tattoos, patches, and other wearable biosensors. POC. 2017;133–50.

204. Yuan F, Xia Y, Lu Q, Xu Q, Shu Y, Hu X. Recent advances in inorganic functional nanomaterials based flexible electrochemical sensors. Talanta. 2022;244:123419.

205. He W, Ye X, Cui T. Flexible Electrochemical Sensor with Graphene and Gold Nanoparticles to Detect Dopamine and Uric Acid. IEEE Sens J. 2021;21(23):26556–65.

206. Zhao J, He C, Wu W, Yang H, Peng L, Wen L, et al. MXene-MoS_2 carbon-fiber-based flexible electrochemical interface for multiple bioanalysis in biofluids. Chem Eng J. 2022;446:136841.

207. Wang Y, Zhao P, Gao B, Yuan M, Yu J, Wang Z, et al. Self-reduction of bimetallic nanoparticles on flexible MXene-graphene electrodes for simultaneous detection of ascorbic acid, dopamine, and uric acid. Microchem J. 2023;185:108177.

208. Wen L, Dong J, Yang H, Zhao J, Hu Z, Han H, et al. A novel electrochemical sensor for simultaneous detection of Cd^{2+} and Pb^{2+} by MXene aerogel-CuO/carbon cloth flexible electrode based on oxygen vacancy and bismuth film. Sci Total Envir. 2022;851:158325.

209. Zhu X, Lin L, Wu R, Zhu Y, Sheng Y, Nie P, et al. Portable wireless intelligent sensing of ultra-trace phytoregulator α-naphthalene acetic acid using self-assembled phosphorene/Ti_3C_2-MXene nanohybrid with high ambient stability on laser induced porous graphene as nanozyme flexible electrode. Biosens Bioelectron. 2021;179:113062.

210. Li QF, Chen X, Wang H, Liu M, Peng HL. Pt/MXene-Based Flexible Wearable Non-Enzymatic Electrochemical Sensor for Continuous Glucose Detection in Sweat. ACS Appl Mater Interfaces. 2023;15(10):13290–8.

211. Ankitha M, Shabana N, Vaishag P V., Rasheed PA. A novel flexible electrode with highly stable trifluoroacetic acid modified Nb_2CT_x MXene for the sensitive detection of rifampicin. JAEC. 2023;928:117088.

212. Aparicio-Martínez E, Ibarra A, Estrada-Moreno IA, Osuna V, Dominguez RB. Flexible electrochemical sensor based on laser scribed Graphene/Ag nanoparticles for non-enzymatic hydrogen peroxide detection. Sens Actuators B Chem. 2019;301:127101.

213. Morales-Masis M, De Wolf S, Woods-Robinson R, Ager JW, Ballif C. Transparent Electrodes for Efficient Optoelectronics. Adv Electron Mater. 2017;3(5):1600529.

214. Li J, Jiang M, Su M, Tian L, Shi W, Yu C. Stretchable and Transparent Electrochemical Sensor Based on Nanostructured Au on Carbon Nanotube Networks for Real-Time Analysis of H_2O_2 Release from Cells. Anal Chem. 2021;93(17):6723–30.

215. Kim GJ, Kim KO. Novel glucose-responsive of the transparent nanofiber hydrogel patches as a wearable biosensor via electrospinning. Sci Rep. 2020;10(1):1–12.

216. Won P, Kim KK, Kim H, Park JJ, Ha I, Shin J, et al. Transparent Soft Actuators/Sensors and Camouflage Skins for Imperceptible Soft Robotics. Adv Mater. 2021;33:2002397.

217. Cho YU, Lim SL, Hong JH, Yu KJ. Transparent neural implantable devices: a comprehensive review of challenges and progress. Flexible Electronics. 2022;6:53.

218. Bai Y, Li S. Oxidative Stress Sensing System for 8-OHdG Detection Based on Plasma Coupled Electrochemistry by Transparent ITO/AuNTAs/PtNPs Electrode. Biosensors (Basel). 2023;13(6):643.

219. Jin ZH, Liu YL, Chen JJ, Cai SL, Xu JQ, Huang WH. Conductive Polymer-Coated Carbon Nanotubes To Construct Stretchable and Transparent Electrochemical Sensors. Anal Chem. 2017;89:2032–8.

220. Oh DE, Lee CS, Kim TW, Jeon S, Kim TH. A Flexible and Transparent PtNP / SWCNT / PET Electrochemical Sensor for Nonenzymatic Detection of Hydrogen Peroxide Released from Living Cells with Real-Time Monitoring Capability. Biosensors (Basel). 2023;13(7):704.

221. Oh JW, Heo J, Kim TH. An electrochemically modulated single-walled carbon nanotube network for the development of a transparent flexible sensor for dopamine. Sens Actuators B Chem. 2018;267:438–47.

222. Urgunde AB, Kumar AR, Shejale KP, Sharma RK, Gupta R. Metal wire networks functionalized with nickel alkanethiolate for transparent and enzymeless glucose sensors. ACS Appl Nano Mater. 2018;1(10):5571–80.

223. Zhang XY, Xu JL, Ren S, Yang Q, Liu MJ, Chang XH, et al. Flexible and Transparent Composite Electrode with 3D Freestanding Architecture for Dopamine Monitoring. Adv Electron Mater. 2022;8(12):220610.

224. Rakhi RB, Nayuk P, Xia C, Alshareef HN. Novel amperometric glucose biosensor based on MXene nanocomposite. Sci Rep. 2016;6:36422.

225. Niamsi W, Larpant N, Kalambate PK, Primpray V, Karuwan C, Rodthongkum N, et al. Paper-Based Screen-Printed Ionic-Liquid/Graphene Electrode Integrated with Prussian Blue/MXene Nanocomposites Enabled Electrochemical Detection for Glucose Sensing. Biosensors (Basel). 2022;12(10):852.

226. Chen Y, Sun Y, Niu Y, Wang B, Zhang Z, Zeng L, et al. Portable Electrochemical Sensing of Indole-3-acetic Acid Based on Self-assembled MXene and Multi-walled Carbon Nanotubes Composite Modified Screen-printed Electrode. Electroanalysis. 2023;35(3):2200279.

227. Rasheed PA, Pandey RP, Rasool K, Mahmoud KA. Ultra-sensitive electrocatalytic detection of bromate in drinking water based on Nafion/$Ti_3C_2T_x$ (MXene) modified glassy carbon electrode. Sens Actuators B Chem. 2018;265:652–9.

228. Rasheed PA, Pandey RP, Jabbar KA, Ponraj J, Mahmoud KA. Sensitive electrochemical detection of l-cysteine based on a highly stable Pd@$Ti_3C_2T_x$ (MXene) nanocomposite modified glassy carbon electrode. Analytical Methods. 2019;11(30):3851–6.

229. Zhao J, He C, Wu W, Yang H, Peng L, Wen L, et al. MXene-MoS_2 carbon-fiber-based flexible electrochemical interface for multiple bioanalysis in biofluids. Chem Eng J. 2022;446:136841.

230. Mathis TS, Maleski K, Goad A, Sarycheva A, Anayee M, Foucher AC, et al. Modified MAX Phase Synthesis for Environmentally Stable and Highly Conductive $Ti_3C_2T_x$ MXene. ACS Nano. 2021;15(4):6420–9.

231. Hantanasirisakul K, Gogotsi Y. Electronic and Optical Properties of 2D Transition Metal Carbides and Nitrides (MXenes). Advanced Materials. 2018;30(52):1804779.

232. Shekhirev M, Busa J, Shuck CE, Torres A, Bagheri S, Sinitskii A, et al. Ultralarge Flakes of $Ti_3C_2T_x$ MXene via Soft Delamination. ACS Nano. 2022;16(9):13695–703.

233. Boonpakdee D, Guajardo Yévenes CF, Surareungchai W, La-O-Vorakiat C. Exploring non-linearities of carbon-based microsupercapacitors from an equivalent circuit perspective. J Mater Chem A Mater. 2018;6(16):7162–7.

234. Zhang CJ, Kremer MP, Seral-Ascaso A, Park SH, McEvoy N, Anasori B, et al. Stamping of Flexible, Coplanar Micro-Supercapacitors Using MXene Inks. Adv Funct Mater. 2018;28(9):1705506.

235. Lipatov A, Lu H, Alhabeb M, Anasori B, Gruverman A, Gogotsi Y, et al. Elastic properties of 2D $Ti_3C_2T_x$ MXene monolayers and bilayers. Sci Adv. 2018;4(6):1–8.

236. Zhang CJ, Anasori B, Seral-Ascaso A, Park SH, McEvoy N, Shmeliov A, et al. Transparent, Flexible, and Conductive 2D Titanium Carbide (MXene) Films with High Volumetric Capacitance. Advanced Materials. 2017;29(36):1–9.

237. Maleski K, Shuck CE, Fafarman AT, Gogotsi Y. The Broad Chromatic Range of Two-Dimensional Transition Metal Carbides. Adv Opt Mater. 2020;9:2001563.

238. Lioi DB, Joshua Kennedy W, Stevenson PR, Seymour BT, Neher G, Schaller RD, et al. Simultaneous ultrafast transmission and reflection of nanometer-thick $Ti_3C_2T_x$ MXene films in the visible and near-infrared: Implications for energy storage, electromagnetic shielding, and laser systems. ACS Appl Nano Mater. 2020;3(10):9604–9.

239. Hantanasirisakul K, Zhao MQ, Urbankowski P, Halim J, Anasori B, Kota S, et al. Fabrication of $Ti_3C_2T_x$ MXene Transparent Thin Films with Tunable Optoelectronic Properties. Adv Electron Mater. 2016;2:1600050.

240. Bayir H. Reactive oxygen species. Crit Care Med. 2005;33(12):498-501.

241. Pizzino G, Irrera N, Cucinotta M, Pallio G, Mannino F, Arcoraci V, et al. Oxidative Stress: Harms and Benefits for Human Health. Oxid Med Cell Longev. 2017;2017:8416763.

242. Delic NC, Lyons JG, Di Girolamo N, Halliday GM. Damaging Effects of Ultraviolet Radiation on the Cornea. Photochem Photobiol. 2017;93(4):920–9.

243. Masuda T, Shimazawa M, Hara H. Retinal Diseases Associated with Oxidative Stress and the Effects of a Free Radical Scavenger (Edaravone). Oxid Med Cell Longev. 2017;2017:9208489.

244. Dammak A, Pastrana C, Martin-Gil A, Carpena-Torres C, Peral Cerda A, Simovart M, et al. Oxidative Stress in the Anterior Ocular Diseases: Diagnostic and Treatment. Biomedicines. 2023;11(2):292.

245. Chwa M, Atilano SR, Reddy V, Jordan N, Kim DW, Kenney MC. Increased stress-induced generation of reactive oxygen species and apoptosis in human keratoconus fibroblasts. Invest Ophthalmol Vis Sci. 2006;47(5):1902–10.

246. Buddi R, Lin B, Atilano SR, Zorapapel NC, Kenney MC, Brown DJ. Evidence of oxidative stress in human corneal diseases. Journal of Histochemistry and Cytochemistry. 2002;50(3):341–51.

247. Wojcik KA, Kaminska A, Blasiak J, Szaflik J, Szaflik JP. Oxidative stress in the pathogenesis of keratoconus and Fuchs endothelial corneal dystrophy. Int J Mol Sci. 2013;14(9):19294–308.

248. Nita M, Grzybowski A. The Role of the Reactive Oxygen Species and Oxidative Stress in the Pathomechanism of the Age-Related Ocular Diseases and Other Pathologies of the Anterior and Posterior Eye Segments in Adults. Oxid Med Cell Longev. 2016;3164734.

249. Vaneev AN, Kost OA, Eremeev NL, Beznos O V., Alova A V., Gorelkin P V., et al. Superoxide dismutase 1 nanoparticles (Nano-SOD1) as a potential drug for the treatment of inflammatory eye diseases. Biomedicines. 2021;9(4):396.

250. Li S, Tang L, Zhou J, Anchouche S, Li D, Yang Y, et al. Sleep deprivation induces corneal epithelial progenitor cell over-expansion through disruption of redox homeostasis in the tear film. Stem Cell Reports. 2022;17(5):1105–19.

251. Yan Q, Peng B, Su G, Cohan BE, Major TC, Meyerhoff ME. Measurement of tear glucose levels with amperometric glucose biosensor/capillary tube configuration. Anal Chem. 2011;83(21):8341–6.

252. Lockington D, Agarwal P, Young D, Caslake M, Ramaesh K. Antioxidant properties of amniotic membrane: Novel observations from a pilot study. CJO. 2014;49(5):426–30.

253. Shimmura S, Suematsu M, Shimoyama M, Tsubota K, Oguchi Y, Yuzuru Ishimura. Subthreshold UV Radiation-induced Peroxide Formation in Cultured Corneal Epithelial Cells: The Protective Effects of Lactoferrin. Exp Eye Res. 1996;63:519–26.

254. Pan Q, Qiu WY, Huo YN, Yao YF, Lou MF. Low levels of hydrogen peroxide stimulate corneal epithelial cell adhesion, migration, and wound healing. Invest Ophthalmol Vis Sci. 2011;52(3):1723–34.

255. Hall SB, Khudaish EA, Hart AL. Electrochemical oxidation of hydrogen peroxide at platinum electrodes. Part 1. An adsorption-controlled mechanism. Electrochim Acta. 1998;43:579–88.

256. Cai X, Tanner EEL, Lin C, Ngamchuea K, Foord JS, Compton RG. The mechanism of electrochemical reduction of hydrogen peroxide on silver nanoparticles. PCCP. 2018;20(3):1608–14.

257. Chen W, Cai S, Ren QQ, Wen W, Zhao Y Di. Recent advances in electrochemical sensing for hydrogen peroxide: A review. Analyst. 2012;137(1):49–58.

258. Yagati AK, Choi JW. Protein Based Electrochemical Biosensors for H_2O_2 Detection Towards Clinical Diagnostics. Electroanalysis. 2014;26(6):1259–76.

259. Sitnikova NA, Komkova MA, Khomyakova I V., Karyakina EE, Karyakin AA. Transition metal hexacyanoferrates in electrocatalysis of H_2O_2 reduction: An exclusive property of prussian blue. Anal Chem. 2014;86(9):4131–4.

260. Lorencova L, Bertok T, Dosekova E, Holazova A, Paprckova D, Vikartovska A, et al. Electrochemical performance of $Ti_3C_2T_x$ MXene in aqueous media: towards ultrasensitive H_2O_2 sensing. Electrochim Acta. 2017;235:471–9.

261. Neampet S, Ruecha N, Qin J, Wonsawat W, Chailapakul O, Rodthongkum N. A nanocomposite prepared from platinum particles, polyaniline and a $Ti_3C_2T_x$ MXene for amperometric sensing of hydrogen peroxide and lactate. Microchimica Acta. 2019;186(12):752.

262. Nagarajan RD, Murugan P, Palaniyandi K, Atchudan R, Sundramoorthy AK. Biocompatible MXene ($Ti_3C_2T_x$) immobilized with flavin adenine dinucleotide as an electrochemical transducer for hydrogen peroxide detection in ovarian cancer cell lines. Micromachines (Basel). 2021;12(8):862.

263. Zhu F, Wang X, Yang X, Zhao C, Zhang Y, Qu S, et al. Reasonable design of an MXene-based enzyme-free amperometric sensing interface for highly sensitive hydrogen peroxide detection. Analytical Methods. 2021;13(22):2512–8.

264. Nagarajan RD, Sundaramurthy A, Sundramoorthy AK. Synthesis and characterization of MXene ($Ti_3C_2T_x$)/Iron oxide composite for ultrasensitive electrochemical detection of hydrogen peroxide. Chemosphere. 2022;286:131478.

265. Li Q, Wang X, Chen L, Liu X, Ma J, Wang L, et al. Cu/Cu_2O nanoparticles modified $Ti_3C_2T_x$ MXene with in-situ formed TiO_2-X for detection of hydrogen peroxide. Ceram Int. 2023;49(6):9632–41.

266. Singh S, Numan A, Khalid M, Bello I, Panza E, Cinti S. Facile and Affordable Design of MXene-Co_3O_4-Based Nanocomposites for Detection of Hydrogen Peroxide in

Cancer Cells: Toward Portable Tool for Cancer Management. Small. 2023;19(51):2208209.

267. Rajaji U, Ganesh PS, Kim SY, Govindasamy M, Alshgari RA, Liu TY. MoS_2 Sphere/2D S- $Ti_3C_2T_x$ MXene Nanocatalysts on Laser-Induced Graphene Electrodes for Hazardous Aristolochic Acid and Roxarsone Electrochemical Detection. ACS Appl Nano Mater. 2022;5(3):3252–64.

268. Zhu B, An D, Bi Z, Liu W, Shan W, Li Y, et al. Two-Dimensional Nitrogen-Doped Ti3C2 Promoted Catalysis Performance of Silver Nanozyme for Ultrasensitive Detection of Hydrogen Peroxide. ChemElectroChem. 2022;9(10):1–11.

269. Chen L, Wakeel M, Haq TU, Chen C, Ren X. Insight into UV-induced simultaneous photocatalytic degradation of $Ti_3C_2T_x$ MXene and reduction of U(VI). J Hazard Mater. 2022;430:128377.

270. Zhang CJ, Pinilla S, McEvoy N, Cullen CP, Anasori B, Long E, et al. Oxidation Stability of Colloidal Two-Dimensional Titanium Carbides (MXenes). Chem Mater. 2017;29(11):4848–56.

271. Class II Daily Wear Contact Lenses - Premarket Notification [510(k)] Guidance Document. Office of Medical Products and Tobacco, Center for Devices and Radiological Health. 1994; Accessed Jan 2024.

272. Averbeck SR, Xu D, Murphy BB, Shevchuk K, Shankar S, Anayee M, et al. Stability of $Ti_3C_2T_x$ MXene Films and Devices under Clinical Sterilization Processes. ACS Nano. 2023;17:9442–54.

273. Lee JH, Huynh-Nguyen BC, Ko E, Kim JH, Seong GH. Fabrication of flexible, transparent silver nanowire electrodes for amperometric detection of hydrogen peroxide. Sens Actuators B Chem. 2016;224:789–97.

274. Stenfilcon A Soft (Hydrophilic) Daily Disposable Contact Lenses [Internet]. Available from: www.coopervision.com

275. Barnes LM, Phillips GJ, Davies JG, Lloyd AW, Cheek E, Tennison SR, et al. The cytotoxicity of highly porous medical carbon adsorbents. Carbon. 2009;47(8):1887–95.

276. Corporation P. CellTiter 96 ® AQ ueous One Solution Cell Proliferation Assay Instructions for Use of Products G3580, G3581 and G3582 [Internet]. Accessed Jan 2024. Available from: www.promega.com

277. Corporation P. CytoTox 96 ® Non-Radioactive Cytotoxicity Assay Instructions for Use of Product G1780 [Internet]. Accessed Jan 2024. Available from: www.promega.com

278. Yu LP, Lu L, Zhou XH, Xu L. Current Understanding of the Wettability of MXenes. Adv Mater Interfaces. 2023;10(2):2201818.

279. Chen Z, Li W, Yang X, Ke C, Chen H, Li Q, et al. Gel polymer electrolyte with MXene to extend cycle lifespan of flexible and rechargeable Zinc–Air batteries. J Power Sources. 2022;523:231020.

280. Silvestrini M, Brito C. Wettability of Reentrant Surfaces: A Global Energy Approach. Langmuir. 2017;33(43):12535–45.

281. Efron N. Contact Lens Practice. Third Edition. Elsevier; 2018.

282. Tanti NC, Jones L, Gorbet MB. Impact of Multipurpose Solutions Released from Contact Lenses on Corneal Cells. Optom Vis Sci. 2011;88(4):482-92.

283. Ghasemi H, Ghazanfari T, Yaraee R, Faghihzadeh S, Hassan ZM. Roles of IL-8 in ocular inflammations: A review. Ocul Immunol Inflamm. 201;19(6):401–12.

284. Fortingo N, Melnyk S, Sutton SH, Watsky MA, Bollag WB. Innate Immune System Activation, Inflammation and Corneal Wound Healing. Int J Mol Sci. 2022;23(23):14933.

285. Osuagwu UL, Ogbuehi KC. UV-vis light transmittance through tinted contact lenses and the effect of color on values. Contact Lens Anterior Eye. 2014;37(3):136–43.

286. Sekar P, Dixon PJ, Chauhan A. Pigmented contact lenses for managing ocular disorders. Int J Pharm. 2019;555:184–97.

287. Lai CF, Li JS, Fang YT, Chien CJ, Lee CH. UV and blue-light anti-reflective structurally colored contact lenses based on a copolymer hydrogel with amorphous array nanostructures. RSC Adv. 2018;8(8):4006–13.

288. Garland NT, Schmieder J, Johnson ZT, Hjort RG, Chen B, Andersen C, et al. Wearable Flexible Perspiration Biosensors Using Laser-Induced Graphene and Polymeric Tape Microfluidics. ACS Appl Mater Interfaces. 2023;15(32):38201–13.

289. Zhang YZ, El-Demellawi JK, Jiang Q, Ge G, Liang H, Lee K, et al. MXene hydrogels: fundamentals and applications. Chem Soc Rev. 2020;49:7229-7251

290. Wongrakpanich A, Mudunkotuwa IA, Geary SM, Morris AS, Mapuskar KA, Spitz DR, et al. Size-dependent cytotoxicity of copper oxide nanoparticles in lung epithelial cells. Environ Sci Nano. 2016;3(2):365–74.

291. Gogotsi Y, Huang Q. MXenes: Two-Dimensional Building Blocks for Future Materials and Devices. ACS Nano. 2021;15(4):5775–80.

292. Feng W, Han X, Hu H, Chang M, Ding L, Xiang H, et al. 2D vanadium carbide MXenzyme to alleviate ROS-mediated inflammatory and neurodegenerative diseases. Nat Commun. 2021;12(1):1–16.

293. Sleigh JW, Linter SPK. Hazards of hydrogen peroxide. Br Med J (Clin Res Ed). 1985;291(6510):1706.

294. Caron S, Dugger RW, Ruggeri SG, Ragan JA, Brown Ripin DH. Large-scale oxidations in the pharmaceutical industry. Chem Rev. 2006;106(7):2943–89.

295. Pohanka M. Glucose electrochemical biosensors: The past and current trends. Int J Electrochem Sci. 2021;16(7):1–12.

296. Rashid JIA, Yusof NA. The strategies of DNA immobilization and hybridization detection mechanism in the construction of electrochemical DNA sensor: A review. Sens Biosensing Res. 2017;16:19–31.

297. Gao Z, Li Y, Zhang C, Zhang S, Li F, Wang P, et al. Label-free electrochemical immunosensor for insulin detection by high-efficiency synergy strategy of Pd NPs@3D MoSx towards H_2O_2. Biosens Bioelectron. 2019;126:108–14.

299. Noriega N., Shekhirev M., Shuck CE., Salvage J., VahidMohammadi A., Dymond MK., Lacey J., Sandeman S., Gogotsi Y., Patel BA. ACS Appl Mater Interfaces. 2024;16(5):6569-6578.

8 Appendix

8.1 Publications

- N. Noriega et al. "$Ti_3C_2T_x$ electrochemical sensor for the detection of H_2O_2 in tear fluid" (*In preparation)*
- N. Noriega et al. Book Chapter: "MXene Handbook, Chapter 17: MXenes in Healthcare Technologies", accepted December 2023
- N. Noriega et al. "Pristine $Ti_3C_2T_x$ MXene Enables Flexible and Transparent Electrochemical Sensors", ACS Applied Materials and interfaces, accepted January 2024

8.2 Honors and Awards

- Best Oral Presentation Award, Analytical Professionals, May 2023
- People's Choice Best Presentation Award, 3 Minute Thesis Competition, June 2023
- International Research Scholarship, University of Brighton, October 2019 – June 2023

8.3 Leadership and volunteering

- Head, MXene Bio-Applications Group coordinated between UPenn, Drexel and UoB
- Post Graduate Student Representative, School of Applied Sciences, UoB

8.4 Presentation of work through presentations:

- Transparent and Flexible $Ti_3C_2T_x$ MXene Electrochemical Sensors for H_2O_2, Poster and Oral Presentation
  Graphene Conference, Manchester, UK, June 2023
- MXenes Electrochemical Sensors for the Detection of Hydrogen Peroxide, Oral Presentation
- Early Analytical Professionals, Bristol, UK, May 2023

- Two-dimensional Transition Metal Carbides (MXenes) for Electrochemical Sensing, Oral Presentation
- Pittcon Conference, Philadelphia, USA, March 2023
- 2D Transition Metal Carbides (MXenes) for Electrochemical Sensing, Teaching Presentation
- MXene Course, Online, February 2023
- Exploring the Scope of Pristine $Ti_3C_2T_x$ MXene for electrochemical sensing, Oral Presentation
- RSC Electrochem. Conference, Edinburgh, UK, September 2022
- The Electroactivity of Pristine MXene Electrodes, Poster Presentation
- MXene Conference, Philadelphia, USA, August 2022
- Keep Your Tears Where They Belong and Used Them to Monitor Your Health, Oral Presentation
- Festival of Postgraduate Research, 3-min Thesis, Brighton, UK, June 2022
- Optical Properties of 2D Transition Metal Carbides (MXenes), Teaching Presentation
- MXene Course, Online, February 2022 and June 2021
- MXenes for Ophthalmic Biosensing, Poster Presentation
- MXene Conference, Online, August 2020